MAGNETO HYDRODYNAMIC FLOW IN A TWO-DIMENSIONAL BEND

by

John H. W. Lau B.A.Sc., M.A.Sc.

Submitted in partial fulfillment of the requirements for the degree of Doctor of Philosophy

Department of Electrical Engineering
Faculty of Pure and Applied Science
University of Ottawa
Ottawa, Ontario

November 1969

Summary

The purpose of this thesis is to investigate theoretically and experimentally the effect of crossed electric and magnetic fields on the motion of conducting compressible and incompressible fluids flowing along a two-dimensional right-angle bend. The work reported herein breaks down into the following individual stages.

(1) Using the method of characteristics, the flow of conducting, compressible fluid flowing at supersonic speed along the bend under the action of an aligned magnetic field was studied. The calculation shows clearly the effectiveness of the field in delaying and ultimately suppressing the standing shock normally encountered in this type of flow.

(2) The flow of ideal, incompressible, inviscid fluid without MHD effects was investigated theoretically using two methods not hitherto employed in connection with this problem. (a) The Rayleigh-Ritz variational approach was used to calculate the coefficients of an orthogonal function series governing the flow. This method is semi-analytic, in that it provides complete analytic information in series form once the coefficients are determined by numerically solving a matrix equation. (b) The method of integral relations was employed to this problem yielding numerical results which were found to be in close agreement with method (a) as well as with results of calculations of other authors. The two methods allow more accurate assessment of the effect of straight inlet and exit regions to the bend than was hitherto reported in the literature.

(3) The method of integral relations was also applied to the case of subsonic flow of conducting gas along the bend under the action of an aligned magnetic field, without applied electric field. Calculations show that the effect of the field on the wall pressure distribution was too small to be measurable with the equipment normally available in the laboratory, as the effect is of the nature of a second order correction to the undisturbed (non-MHD) condition.

(4) The effect of aligned magnetic and crossed, applied electric field on the flow in the bend was studied mathematically. This is a zero-order effect in which compressibility enters as a first order correction. The latter was therefore neglected. The wall pressure distribution was calculated using both methods (a) and (b) above, yielding close agreement with each other. Results indicate that with this arrangement of electromagnetic fields, the adverse effect on the pressure distribution of the centrifugal forces can largely be counteracted.

(5) By way of confirmation of the above calculations, experiments were carried out using a solution of electrolyte in a bend with applied electric and magnetic fields. The wall pressure distribution was measured using liquid manometers and both the basic pressure distribution predicted in (2) as well as the modifications introduced by the MHD effects, calculated in (4) were confirmed with fair accuracy after allowance was made for the viscous pressure losses.

(6) The wall pressure distribution in a bend due to flow of potassium seeded, ionized argon from a plasma arc jet both with

and without applied, crossed fields was measured with a scanning electric pressure transducer. The predicted pressure distribution without applied fields was confirmed with fair accuracy, but the modification due to MHD effects of the pressures was not borne out by the experiments except in a qualitative sense of a partial suppression of centrifugal forces. The reasons for this discrepancy are discussed in terms of non-uniform current distribution along the electrodes.

ACKNOWLEDGEMENTS

The author wishes to thank Prof. G. S. Glinski, his thesis supervisor and Mr A. J. Bachmeier for their interest and encouragement.

The author is also sincerely grateful for the continuing advice and inspiration of his immediate supervisor, Dr P. Savic, during the course of this work.

Most of the experimental work was performed using the arc-jet designed by Mr E. H. Dudgeon; his advice and assistance, together with those of Dr I. R. G. Lowe and Mr E. V. Evans, in operating, maintaining of the arc-jet, and its adaptation to the present experiment have been an essential contribution to this work. For this the author is deeply indebted.

TABLE OF CONTENTS

TABLE OF CONTENTS (CONT'D)

NOTATION

A_i	Constants defined in various sections
a_p	Constants defined in sections 3.2 and 3.4
a_{ij}	Constants defined in section 3.3
B	Magnetic field intensity
B_i	Constant defined in section 3.2.3
B_{ij}	Constant defined in section 3.3
C_i	Constant defined in section 3.2.3
C_{ij}	Constant defined in section 3.3
C_v	Specific heat at constant volume
c	Sound speed
D	Height of 2-D channel
d_p	Constants defined in section 3.3
F_{ij}	Constants defined in section 3.2.3
G	Green's function
G_i	Constant defined in section 3.2.3
H_i	Constant defined in section 3.2.3
h	Function as defined in section 3.2.2
J	Current
j	Current density
K	Constant as defined in section 3.3
M	Mach number
M_i	Constant as defined in section 3.2.3
P	Pressure at downstream infinity (section 3.3)
P_i	Constant as defined in section 3.3
p	Pressure

NOTATION (CONT'D)

Q_i	Constant as defined in section 3.3
R_o	Radius of inner wall of bend
R	Density at downstream infinity (section 3.3)
r	Radius in cylindrical coordinates
S	Interaction parameter
s	Entropy
T	Temperature
u	Velocity
V	Velocity
x	Cartesian coordinates
y	Cartesian coordinates
Z	Function as defined in section 3.2.2

Greek Symbols

α	Angle as defined in section 3.1, or constants as defined in various sections, or function of ρ, u, v as defined in section 3.3
β	Integral as defined in section 3.2.2, or function of ρ, u, v as defined in section 3.3
γ	Ratio of specific heat or constants as defined in section 3.4
ϵ	$(A_1 - a_1)$, a small parameter
ξ	Function of ρ, u, v as defined in section 3.3
θ	Angle in cylindrical coordinates
ϕ	Angle as defined in section 3.1
ρ	Density
ω	$\nabla \times V$, vorticity

NOTATION (CONT'D)

Subscripts

x	Component along x direction
y	Component along y direction
r	Component along r direction
θ	Component along θ direction
i	Values at i^{th} strip, or i^{th} term in series

ILLUSTRATIONS

ILLUSTRATIONS (CONT D)

ILLUSTRATIONS (CONT'D)

1. Introduction

The theories of fluid mechanics and electromagnetic field have been well developed for some time, but a combination of these two disciplines, i.e. the interation between a flow field and an electromagnetic field, commonly known as magnetohydrodynamics, has not, until the last fifteen or twenty years, been investigated extensively. Most of the interest was spurred initially by astrophysical considerations and problems associated with controlled thermonuclear fusion. Today, the study of MHD has brought forth many interesting results and useful applications, e.g. in flow control, communications, aerodynamics, plasma containment, propulsion and power generation.

The study of MHD interaction effect dates back to the times of Faraday, but it was not until the early twentieth century that this principle was used in a practical device, the electromagnetic pump. At that time, the only fluids available which were capable of conducting electricity were liquid metals and electrolytes with which a high degree of interaction is not easily attained. Today, however, with various plasma generating devices, highly conducting gases with temperatures up to millions of degrees can be readily produced in the laboratory, and with the application of superconducting magnets, strong interactions can be achieved.

The present thesis attempts to study the effect of a curved magnetic field on the ionized gas flow around a 90° bend, with the purpose of investigating how the flow of hot ionized gases can be influenced and controlled by electromagnetic fields. Earlier investigators of plasma flow in curved fields [1 - 5] dealt with tenuous plasmas ($n = 10^{12}/cm^3$) and found that for a field of 4.5

KGauss, the particles follow the curved field lines quite well. A current flow parallel to $\bar{B}$ in these cases shorts out the polarization field due to the $\nabla_{\perp}B$ drifts, so that the $\bar{E} \times \bar{B}$ drift towards the outer wall of the bend was not pronounced, In atmospheric pressure plasmas, however, the mechanism by which a curved field influences the flow is quite different. The particles on turning around the bend, experience a centrifugal force and this is balanced by a pressure gradient between the inner and outer wall. If a current flows across the plasma either due to the interaction of fluid flow and the magnetic field, or due to external sources, this current will interact with the magnetic field, producing interacting forces between the plasma and the magnetic field.

To gain some insight into the problem, we started with calculating the supersonic flow around a bend under the influence of a magnetic field aligned with the bend. The characteristic net shows the formation of a shock without magnetic field; the latter serves to delay the shock formation, and eventually inhibits it altogether with strong enough fields. This phenomenon could have been easily detected by optical means. Unfortunately, an estimate of the mass flow and power required to heat the gas to the desired temperature shows that the plasma jet in this laboratory did not have sufficient power. A complete theoretical analysis was therefore carried out for the subsonic compressible flow. Because the streamlines and the magnetic field lines are almost parallel to one another, the results at Mach number of 0.6 show that the pressure difference produced by adding the magnetic field is very small since it constitutes only a first order effect. It was decided then that to be able to measure any significant interaction effects, an external source had to be applied to drive a current through the plasma. To reduce both theoretical and experimental complications a slower flow was used, so that an incompressible flow model could be assumed. The analysis shows that with the present equipment, an interaction parameter can be achieved to produce measurable pressure differences. The primary concern of the present research is to investigate how these differences can be produced and measured.

2. Review of Work on Flow Around Bends and Purpose of the Present Experiment

Neglecting the effects of viscosity and heat conduction, the potential flow around a two-dimensional bend can be readily analysed, since it satisfies the Laplace equation. However, since all fluids are viscous and conduct heat, the flow field is vortical, and the resulting three-dimensional flow becomes quite complex. Much of the earlier work on such flows was stimulated by the interest in flows in cascades of compressors and turbine blades, and losses in ducting. An excellent survey and summary was published by Hawthorne[8]. A brief description is given below.

Consider the flow around an elbow with rectangular cross-section. Depending on the length and aspect ratio of the inlet section before the bend, the velocity approaching the bend will have a fully developed or a developing velocity profile, with zero velocity at the walls due to viscosity. As the fluid flows around the bend, a pressure gradient develops in the radial direction to balance the centrifugal force. A typical pressure plot around a bend with long upstream and downstream straight section is shown in Fig. 1 (Ward-Smith, 1963)[52]. Because of the higher velocity along the centre plane (A-A, Fig. 2), the pressure gradient is largest there, driving the fluid in a transverse plane, forming the secondary vortices (Fig. 2). The character of the whole flow field is then changed because the Bernoulli surfaces (surfaces of constant stagnation pressure) are distorted, and theoretical analysis is very difficult. Squire and Winter[44], Hawthorne[45], Karman and Tsien[46] analysed the three-dimensional disturbances to a basic two-dimensional shear flow using a linearized approach, and their theories proved to be most fruitful. However, up to the present, there does not seem to exist a quantitative study of the relation of these secondary flows to the losses around bends. From some of the results, Eichenberger[9] and Hawthorne[8] concluded that large losses around bends are not due to energy associated with the secondary flow, but rather to the increased viscous dissipation caused by the spreading of high velocity fluid onto the walls under the convective action of the secondary flows. Using a rather crude analysis, Hawthorne[47] showed that the high velocity fluid is rotated back and forth about the axis of the pipe, making a complete oscillation approximately $1.2\ (2\pi)\sqrt{d/R}$ radians of bend deflection, where R is the radius of the bend and d the height of the channel.

In ducts with large deflections and helical flows this oscillation is quickly damped by viscosity after the first cycle and only a steady secondary flow pattern (fully developed curved flow) exists as described by Dean[48], White[49], Adler[50] and Cuming[51].

With most bends and blade rows of interest, only a fraction of a complete oscillation (depending on bend geometry and inlet condition) has occurred at the outlet of the bend. The secondary velocity and position of the Bernoulli surfaces therefore vary at the outlet, and Hawthorne[8] concluded that it was probably due to these large residual secondary flows at the outlet that some of the results with the appropriate $\sqrt{R/d}$ value suffer the larger losses.

One of the most important phenomena in bend flow as distinct from straight pipe flow is the appearance of a pressure difference between inner and outer curved walls to balance the centrifugal force. This in turn, as discussed above, sets up the secondary motion and causes much of the extra loss in bend flow. If it were possible to eliminate or reduce this pressure difference by applying externally a body force on the fluid, the secondary flow should be smaller in magnitude and the extra loss should accordingly be reduced. Moreover, for bends with small R/d values, the low velocity fluid near the walls cannot overcome the large axial pressure gradient generated (Fig. 1), and the flow separates. Such flow separation could be avoided if the external body force were large enough to reduce the pressure gradient below its critical value.

The effect of electromagnetic body force on the secondary vorticity is calculated by a rough approximation in the Appendix. The actual computation is not attempted here since it involves a step by step integration of a rather complicated set of equations. Moreover, the relation between the bend losses and these secondary vorticities is not easily formulated, and generating secondary vorticities and measuring their changes is quite difficult in a hot plasma flow, and is at any rate beyond the scope of this thesis. The experiments to be described were therefore performed only with a view to studying the effectiveness of MHD forces in reducing the transverse pressure gradient.

An arc-heated, potassium-seeded argon plasma jet was used as the source of flow, with a static temperature of about 3000°K. Pitot probing of the hot, high velocity flow to study the flow losses in the present arrangement is quite difficult and was not attempted here. Instead, a fairly uniform velocity distribution at the inlet to the bend was used in order to avoid complications due to secondary flows. The inlet to the bend section was therefore placed quite close to the contraction section of the settling chamber to ensure a uniform velocity and to avoid excessive heat loss to the walls. Also, a bend with R/d value which incurs the smallest loss and which is not likely to induce separation is chosen for the present experiment.

3. Theoretical Analysis

3.1 Supersonic Flow Around a Two-Dimensional Bend

To solve the problem of compressible magnetohydrodynamic flow around a bend requires quite, lengthy techniques, and in order to start with a comparatively tractable instance, a case was chosen in which a simple well developed mathematical technique can be applied[6,7]. This section describes the supersonic, inviscid and non-heat conducting flow around a two-dimensional right angle bend under the influence of an aligned magnetic field. The magnetic

Reynolds number is assumed to be small so that the applied field is not perturbed by the current generated in the plasma flow. It is also assumed that there are no electrode or boundary layer losses. The ratio of channel height to the radius of the bend is chosen to be small (0.1), so that the field lines can be assumed to be approximately concentric circles in the bend and straight lines in the inlet and exit sections. The governing set of equations are:

$$\rho \bar{V} \cdot \nabla \bar{V} = -\nabla p + \bar{J} \times \bar{B} \qquad \text{Momentum}$$

$$\nabla \cdot \rho \bar{V} = 0 \qquad \text{Continuity}$$

$$\rho T \bar{V} \cdot \nabla s = \frac{J^2}{\sigma} \qquad \text{Energy}$$

$$\bar{J} = \sigma(\bar{V} \times \bar{B}) \qquad \text{Ohm's Law}$$

$$\frac{p}{p_\infty} = \left(\frac{\rho}{\rho_\infty}\right)^{\gamma} e^{s/c_v} \qquad \text{State}$$

Here the conductivity is assumed to be constant and the current generated by the induced electric field ($\bar{V} \times \bar{B}$) when the flow moves across a field line is assumed to flow freely across the two side walls which are perfect conductors shorted together (i.e. there a are no electrode losses).

In matrix form, the set of equations reduces to:

$$
\begin{bmatrix}
\rho & 0 & 0 & \rho & u & v & 0 & 0 \\
u & v & 0 & 0 & \frac{c^2}{\rho} & 0 & \frac{c^2}{\gamma} & 0 \\
0 & 0 & u & v & 0 & \frac{c^2}{\rho} & 0 & \frac{c^2}{\gamma} \\
0 & 0 & 0 & 0 & 0 & 0 & u & v \\
dx & dy & 0 & 0 & 0 & 0 & 0 & 0 \\
0 & 0 & dx & dy & 0 & 0 & 0 & 0 \\
0 & 0 & 0 & 0 & dx & dy & 0 & 0 \\
0 & 0 & 0 & 0 & 0 & 0 & dx & dy
\end{bmatrix}
\times
\begin{bmatrix}
\frac{\partial u}{\partial x} \\
\frac{\partial u}{\partial y} \\
\frac{\partial v}{\partial x} \\
\frac{\partial v}{\partial y} \\
\frac{\partial \rho}{\partial x} \\
\frac{\partial \rho}{\partial y} \\
\frac{\partial S/c_v}{\partial x} \\
\frac{\partial S/c_v}{\partial y}
\end{bmatrix}
=
\begin{bmatrix}
0 \\
-\frac{\sigma B_y}{\rho}(uB_y - vB_x) \\
\frac{\sigma B_x}{\rho}(uB_y - vB_x) \\
\frac{\gamma(\gamma-1)\sigma(uB_y - vB_x)}{\rho c^2} \\
du \\
dv \\
d\rho \\
d\,S/c_v
\end{bmatrix}
$$

The derivatives $\partial u/\partial x$, $\partial u/\partial y$, etc. can be solved in the form of a quotient of two determinants. By the theory of hyperbolic p.d.e., these derivatives can be discontinuous (or indeterminate), and the determinants can be set to zero, yielding the three characteristic curves and the compatibility equations along them. The equations are:

Characteristic I $$u\,dy - v\,dx = 0$$

Compatibility I $$\frac{v c^2\, d\,{}^{S}\!/_{C_v}}{\gamma(\gamma-1)} - \frac{\sigma(uB_y - vB_x)^2}{\rho}\,dy = 0$$

Characteristic II (− sign)

III (+ sign) $$dy = \frac{uv \pm \sqrt{u^2 + v^2 - c^2}\;dx}{u^2 - c^2}$$

Compatibility II and III,

$$(v^2-u^2)(du\,dx - dv\,dy) - 2uv\,(du\,dy + dv\,dx)$$
$$- \frac{c^2\,d\,{}^{S}\!/_{C_v}}{\gamma(\gamma-1)}\cdot(u\,dx + v\,dy) + \frac{\sigma(uB_y - vB_x)}{\rho}\Big[B_y\big\{v\,dx\,dy - (\gamma-1)\,u\,dx^2$$
$$- \gamma u\,dy^2\big\} + B_x\big\{\gamma v\,dx^2 + (\gamma-1)\,v\,dy^2 -$$
$$u\,dx\,dy\big\}\Big] = 0$$

In polar coordinates, where

$$u = V\cos\theta \qquad x = r\sin\phi$$
$$v = V\sin\theta \qquad y = r\cos\phi$$
$$\frac{1}{M} = \frac{c}{V} = \sin\alpha$$

the equations become

$$\frac{dy}{dx} = \tan\theta$$

Characteristic I $$d\,{}^{S}\!/_{C_v} = \frac{\gamma(\gamma-1)\,\sigma B^2 V^2 \sin^2(\phi+\theta)\,dx}{\rho c^2\cos\theta}$$

Characteristic II (− sign), III (+ sign)

$$\frac{dy}{dx} = \tan(\theta \pm \alpha)$$

Compatibility II and III,

$$\pm d\theta - \cot\alpha \cdot \frac{dV}{V} - \frac{\sin\alpha\cos\alpha}{\gamma(\gamma-1)}\, d\,{}^{s}\!/_{c_v} + \frac{\sigma B^2 dx}{\rho V}\frac{\sin(\phi+\theta)}{\sin\alpha\cos(\theta\pm\alpha)}\cdot$$

$$\left[\sin(\phi+\theta\pm\alpha)\cos\alpha + \gamma\sin(\theta+\phi)\right] = 0$$

These characteristic equations, together with the energy equation

$$\frac{d\rho}{\rho} = \frac{dV^2}{2c^2} - \frac{d\,{}^{s}\!/_{c_v}}{\gamma-1}$$

which applies through the whole flow field, were used to construct the whole characteristic net. For example, point "3" can be located by drawing three characteristic lines from points 1 and 2 (Fig. 3a), where all variables are known, and flow variables at point 3 can be computed by the following finite difference equations derived from above characteristic equations.

$$x_3 = \frac{1}{\tan(\theta+\alpha)_2 - \tan(\theta-\alpha)_1}\left[y_1 - y_2 + x_2\tan(\theta+\alpha)_2 - x_1\tan(\theta-\alpha)_1\right]$$

$$y_3 = y_2 + \tan(\theta+\alpha)_2\cdot(x_3 - x_2)$$

$$\theta_3 = \frac{1}{\cos\alpha_1\sin\alpha_1 + \cos\alpha_2\sin\alpha_2}\Big[\cos\alpha_1\sin\alpha_1\cdot\theta_2 + \cos\alpha_2\sin\alpha_2\cdot\theta_1$$

$$+ \frac{\cos\alpha_2\sin\alpha_2\cos\alpha_1\sin\alpha_1}{\gamma-1}\ln\frac{c_2^2}{c_1^2} - \frac{\sin\alpha_2\cos\alpha_2\sin\alpha_1\cos\alpha_1}{\gamma(\gamma-1)}(s_2 - s_1)$$

$$- \frac{m\cos\alpha_1\sin\alpha_1}{\rho_2 V_2}\frac{\sin(\theta+\phi)_2\left[\sin(\phi+\theta+\alpha)_2\cos\alpha_2 + \gamma\sin(\theta+\phi)_2\right]}{\sin\alpha_2\cos(\theta+\alpha)_2}(x_3 - x_2)$$

$$+ \frac{m\cos\alpha_2\sin\alpha_2}{\rho_1 V_1}\frac{\sin(\theta+\phi)_1\left[\sin(\phi+\theta-\alpha)_1\cos\alpha_1 + \gamma\sin(\theta+\phi)_1\right]}{\sin\alpha_1\cos(\theta-\alpha)_1}(x_3 - x_1)$$

$$S_4 = S_1 + (S_2 - S_1)\,\frac{Y_1 - Y_4}{Y_1 - Y_2}$$

$$\rho_4 = \rho_1 + (\rho_2 - \rho_1)\,\frac{Y_1 - Y_4}{Y_1 - Y_2}$$

$$c_4 = c_1 + (c_2 - c_1)\,\frac{Y_1 - Y_4}{Y_1 - Y_2}$$

$$\theta_4 = \theta_1 + (\theta_2 - \theta_1)\,\frac{Y_1 - Y_4}{Y_1 - Y_2}$$

$$V_4 = V_1 + (V_2 - V_1)\,\frac{Y_1 - Y_4}{Y_1 - Y_2}$$

$$S_3 = S_4 + \frac{\gamma(\gamma-1)\,m\,\sin^2(\phi+\theta)_4\,(x_3 - x_4)\,V_4}{\rho_4\,\cos\theta_4\,c_4^2}$$

$$V_3 = V_2 + V_2\tan\alpha_2\,(\theta_3 - \theta_2) - V_2\,\frac{\sin^2\alpha_2}{\gamma(\gamma-1)}\,(S_3 - S_2)$$

$$+ \frac{m}{\rho_2}\cdot\frac{\sin(\phi+\theta)_2\,(x_3 - x_2)}{\cos\alpha_2\,\cos(\theta+\alpha)_2}\left[\sin(\phi+\theta+\alpha)_2\cos\alpha_2 + \gamma\sin(\theta+\phi)_2\right]$$

$$c_3 = \sqrt{\frac{\gamma-1}{2}(V_2^2 - V_3^2) + c_2^2}$$

$$\alpha_3 = \sin^{-1}\frac{1}{M_3} = \sin^{-1}\frac{c_3}{V_3}$$

$$\rho_3 = \rho_2\left[1 + \frac{V_2^2 - V_3^2}{2\,c_2^2} - \frac{S_3 - S_2}{\gamma - 1}\right]$$

On the outer wall, (Fig. 3b),

$$x_2 = \cos^2(\theta+\alpha)_1 \Big[x_1 \tan^2(\theta+\alpha)_1 - y_1 \tan(\theta+\alpha)_1$$

$$+ \sqrt{R^2 \sec^2(\theta+\alpha)_1 - \left\{ y_1 - x_1 \tan(\theta+\alpha)_1 \right\}^2}$$

$$y_2 = \sqrt{R^2 - x^2}$$

$$\theta_2 = -\phi_2 = -\tan^{-1} \frac{x_2}{y_2}$$

$$\beta_2 = \beta_0 + \frac{\gamma(\gamma-1)\,\sigma\beta^2 \sin^2(\phi+\theta)_0 V_0}{\rho_0 \sin\theta_0\, c_0^2}(y_2 - y_0)$$

$$V_2 = V_1 + V_1 \tan\alpha_1 \cdot (\theta_2 - \theta_1) - V_1 \frac{\sin^2\alpha_1}{\gamma(\gamma-1)}(\beta_2 - \beta_1)$$

$$+ \frac{m}{\rho_1} \frac{\sin(\phi+\theta)_1 (x_2 - x_1)}{\cos\alpha_1 \cos(\theta+\alpha)_1} \Big[\sin(\phi+\theta+\alpha)_1 \cos\alpha_1 + \gamma \sin(\theta+\phi)_1 \Big]$$

$$c_2 = \sqrt{\frac{\gamma-1}{2}(V_1^2 - V_2^2) + c_1^2}$$

$$\rho_2 = \rho_1 \left[1 + \frac{V_1^2 - V_2^2}{2c_1^2} - \frac{\beta_2 - \beta_1}{\gamma - 1} \right]$$

$$\alpha_2 = \sin^{-1} \frac{c_2}{V_2}$$

On the inner wall, (Fig. 3c),

$$x_2 = \cos^2(\theta-\alpha)_1 \Big[x_1 \tan^2(\theta-\alpha)_1 - y_1 \tan(\theta-\alpha)_1$$

$$- \sqrt{R^2 \sec^2(\theta-\alpha)_1 - \{y_1 - x_1 \tan(\theta-\alpha)_1\}^2}$$

$$y_2 = \sqrt{r_0^2 - x_2^2}$$

$$\theta_2 = -\phi_2 = -\tan^{-1}\frac{x_2}{y_2}$$

$$\beta_2 = \beta_0 + \frac{\gamma(\gamma-1)\sigma B^2 \sin^2(\phi+\theta)_0 V_0}{\rho_0 \sin\theta_0 \; C_0^2}(y_2 - y_0)$$

$$V_2 = V_1 - V_1 \tan\alpha_1 \cdot (\theta_2 - \theta_1) - \frac{V_1 \sin^2\alpha_1}{\gamma(\gamma-1)}(\beta_2 - \beta_1)$$

$$+ \frac{m}{\rho_1}\frac{\sin(\phi+\theta)_1 \cdot (x_2 - x_1)}{\cos\alpha_1 \; \cos(\theta-\alpha)_1}\Big[\sin(\phi+\theta-\alpha)_1 \cos\alpha_1 + \gamma \sin(\theta+\phi)_1\Big]$$

$$C_2 = \sqrt{\frac{\gamma-1}{2}(V_1^2 - V_2^2) + C_1^2}$$

$$\rho_2 = \rho_1 \Big[1 + \frac{V_1^2 - V_2^2}{2C_1^2} - \frac{\beta_2 - \beta_1}{\gamma - 1}\Big]$$

$$\alpha_2 = \sin^{-1}\frac{C_2}{V_2}$$

The SDS 920 computer and the on line Mosley 2DR-2A X-Y plotter were used to construct the characteristic net starting at the entrance to the bend up to the point where the characteristics coalesce to form a shock. In Figure 4, the characteristic nets for different strengths of magnetic field applied are shown. It is seen that the effect of the magnetic field is to delay and eventually inhibit the formation of the shock if a strong enough field is applied. This would have been quite an interesting phenomenon to set up experimentally, since shock waves are quite easy to detect. However, to provide an ideal steady, uniform supersonic plasma flow is a formidable task, especially when separation and secondary flows complicated matters at the bend section. Moreover, the plasma arc jet and vacuum pumps available at present do not quite have the necessary capacity to provide an adequate flow. It was therefore decided to do the experiment for subsonic flows where the power requirements are less and imperfections in the fabrication of the nozzles and test sections are less critical.

3.2 Incompressible Flow in a 90° Bend

3.2.1 General

Much of the earlier work on curved flow was stimulated by the interest in flows in cascades of compressor and turbine blades. The principal features of such flows were summarised in the above-mentioned review by Hawthorne[8] and need not be repeated here. These studies dealt mainly with the development of secondary flow and vorticity and the losses associated with them. However, since it was shown that the energy in the secondary flow after a 90° bend is only a small fraction of the main (axial) flow energy (1 percent as measured by Eichenberger[9]), losses due to wall effects will be neglected. Moreover, the results of Richter and the summary by Hawthorne suggest that the minimum loss in a right-angle bend occurs when the ratio of bend radius/duct diameter is of the order of 3 - 4. Accordingly, in the present study, this ratio was chosen to be 3 and 3.5.

Previous theoretical and experimental work on flow in right-angle bends includes that of Higginbotham et al.[10]. In it, a relaxation method was used to solve the Laplace equation. The experiments showed that when the above length ratio was chosen as 2.5, flow losses were minimised. In earlier theoretical work on potential flow in bends (Szezeniowski[11], Carrier[12]), conformal transformations were used to solve the inverse problem, whereby the bend profile was obtained from assumed velocity distributions. The direct problem of solving for the flow in a given bend profile turns out to be somewhat more difficult. Kamiyama[13] developed a technique, using conformal mapping to obtain a series solution relating the physical coordinates of the bend profile to a unit circle in an auxiliary plane. The pressure distribution then results from the coefficients of the series. This theory was found to agree quite closely with experiments, but pressure and velocity are not given explicitly in terms of physical coordinates. In the following, two methods will be used to solve the potential flow problem in a right-angle bend, the first serving as a check for the second, which will subsequently be extended to the case of compressible magnetohydrodynamic flow.

3.2.2 Rayleigh-Ritz Method

In an incompressible potential fluid flow the stream function ψ satisfies the Laplace equation

$$\nabla^2\psi = 0$$

For the present geometry (Fig. 5), the boundary conditions are $\psi = 0$ on the inner wall and $\psi = 1$ on the outer wall. In order to satisfy the boundary conditions, it is more convenient to use different coordinate systems for the straight and curved parts of the bend. Since the flow is symmetric about the 45° plane, we only have to consider the upstream straight portion. There, the solution that satisfies

$$\psi = 0 \quad \text{on} \quad y = 0$$

$$\psi = 1 \quad \text{on} \quad y = D$$

$$\text{and} \quad \psi = \frac{y}{D} \quad \text{(uniform flow) at} \quad x = -\infty$$

is

$$\psi = \frac{y}{D} + \sum_1^N a_n e^{\frac{n\pi x}{D}} \sin\frac{n\pi y}{D}$$

where a_n are N arbitrary constants. At the entrance to the bend where $x = 0$, $\psi = \frac{y}{D} + \sum a_n \sin\frac{n\pi y}{D}$

In the curved portion, the boundary conditions are therefore

$$\psi = 0 \text{ at } r = 1$$

$$\psi = 1 \text{ at } r = 1 + D$$

$$\text{and} \quad \psi = \frac{r-1}{D} + \sum a_n \sin\frac{n\pi(r-1)}{D} \quad \text{at} \quad \theta = \pm\frac{\pi}{4}$$

To solve the Laplace equation under these boundary conditions it is most convenient to use Green's functions. Put

$$z = \psi - h$$

where $$h(r) = \frac{r-1}{D} + \sum a_n \sin\frac{n\pi(r-1)}{D}$$

Therefore Z satisfies $\nabla^2 Z = \nabla^2\psi - \nabla^2 h = -\nabla^2 h$

and Z = 0 on all boundaries.

Green's function for this region is

$$G_T = \frac{-8}{\pi \ln(1+D)} \frac{\sum\sum \sin\frac{n\pi \ln r}{\ln(1+D)} \cos 2(2m-1)\theta \sin\frac{n\pi \ln r_0}{\ln(1+D)} \cos 2(2m-1)\theta_0}{\left[\frac{n\pi}{\ln(1+D)}\right]^2 + 4(2m-1)^2}$$

Then

$$Z = \iint G_T \cdot \left[-\nabla^2 h(r_0)\right] r_0\, dr_0\, d\theta_0$$

$$= \sum\sum \alpha_{mn} \sin\frac{n\pi \ln r}{\ln(1+D)} \cos 2(2m-1)\theta$$

and

$$\psi = \sum\sum \alpha_{mn} \sin\frac{n\pi \ln r}{\ln(1+D)} \cos 2(2m-1)\theta + \frac{r-1}{D} + \sum a_n \sin\frac{n\pi(r-1)}{D}$$

where

$$\alpha_{mn} = \frac{\frac{8n}{[\ln(1+D)]^2} \cdot \frac{(-1)^{m+1}}{2m-1}\left[\frac{\frac{1}{D} - (-1)^n(1+\frac{1}{D})}{1 + \left\{\frac{n\pi}{\ln(1+D)}\right\}^2}\right] - \sum_k a_k \beta_{kn}}{\left\{\frac{n\pi}{\ln(1+D)}\right\}^2 + 4(2m-1)^2}$$

and

$$\beta_{kn} = \frac{n\pi}{\ln(1+D)} \int_1^{1+D} \sin\frac{k\pi(r-1)}{D} \sin\frac{n\pi \ln r}{\ln(1+D)} \frac{dr}{r}$$

A solution ψ is therefore obtained separately in the straight and curved portions of the bend as a function of the parameters a_k. To find these parameters we note that the integral

$$I = \iint_{\text{WHOLE AREA}} (\nabla\psi)^2\, dA$$

is a minimum if ψ satisfies the Laplace equation. (Kantorovich[14]). We therefore set

$$\frac{\partial I}{\partial a_i} = 2\int_{-\infty}^{0}\int_{0}^{D} \frac{\partial}{\partial a_i}\left[\left(\frac{\partial\psi}{\partial x}\right)^2 + \left(\frac{\partial\psi}{\partial y}\right)^2\right] dx\, dy$$

$$+ \int_{1}^{1+D}\int_{-\frac{\pi}{4}}^{\frac{\pi}{4}} \frac{\partial}{\partial a_i}\left[\left(\frac{\partial\psi}{\partial r}\right)^2 + \left(\frac{1}{r}\frac{\partial\psi}{\partial\theta}\right)^2\right] r\, dr\, d\theta = 0$$

and obtain N linear algebraic equations for a_i, $i = 1 \ldots N$,

$$\left[2i\pi + \frac{i^2\pi^3(D+2)}{4D}\right]a_i + \sum_{k'\neq i} \frac{ik'\pi}{2}\left[\frac{(-1)^{i+k'}-1}{(i+k')^2} + \frac{(-1)^{i-k'}-1}{(i-k')^2}\right]a_{k'}$$

$$-\frac{16\pi}{\{\ln(1+D)\}^3}\sum_k\left[\sum_m\sum_n \frac{\frac{n^2}{(2m-1)^2}\beta_{kn}\beta_{in}}{\left\{\frac{n\pi}{\ln(1+D)}\right\}^2 + 4(2m-1)^2}\right]a_k =$$

$$\frac{1-(-1)^i}{i} + \frac{16\pi}{D[\ln(1+D)]^3}\sum_m\sum_n \frac{\frac{n^2}{(2m-1)^2}\,\frac{(-1)^n(1+D)-1}{1+\left[\frac{n\pi}{\ln(1+D)}\right]^2}}{\left[\frac{n\pi}{\ln(1+D)}\right]^2 + 4(2m-1)^2}\cdot\beta_{in}$$

The above set of algebraic equations was solved on the computer for $N = 10$ and different values of D. The values of a_k were tabulated in Table 1 and show that the series converges fairly rapidly. A comparison with other theoretical work shows that it agrees very well with Kamiyama (Fig. 6a) and the measurements of

Higginbotham[10] (Fig.6b-e), but deviates from the theoretical work of the latter. This is probably due to the fact that when constructing the solution with the relaxation method the grid points were not extended far enough upstream into the straight portion, and this has a very marked effect on the development of the flow in the bend.

3.2.3 Method of Integral Relations

Whereas the solution of the incompressible case is comparatively simple, the more general case where the fluid is compressible is much more difficult. Moreover, magnetohydrodynamic forces create vorticity in the fluid which further complicates the problem. To solve the set of non-linear partial differential equations analytically in the present geometry seems impossible using present day techniques without making drastic assumptions, and one has to seek an approximate solution with the help of a computer. There are at present three well developed methods of solving such equations: the finite difference method, the characteristic method, and the method of integral relations. In the first method, the derivatives are replaced by finite differences, resulting in a system of algebraic equations. For a more complicated set of equations, this method is quite tedious and complex and requires large machine storage. The second method is quite accurate and simple to apply, but it is only suitable for solving hyperbolic equations. For subsonic flow as in the present case, the partial equations are elliptic and this method is therefore not applicable. The third method consists in substituting the dependent variables with an interpolation formula in one direction and then integrating them in that direction. The partial differential equations are thereby reduced to a set of ordinary differential equations, and can be solved using any of a whole host of well developed numerical methods for solution of ordinary differential equations. This method has been used quite successfully in fluid flow problems (references 15-19) and described in detail in a few papers (references 20-23), so the general method will not be described here.

Before applying this method to the final MHD problem, the simple case of potential flow will be solved using this method, to find the best way of approximating the system, since there is no unique or standard procedure for the method, and to check its accuracy. A brief outline of the final form of approximation is given below. As before, different coordinate systems are used on the straight and curved parts of the bend. In the straight part, the equations are:

$$\frac{\partial v}{\partial x} - \frac{\partial u}{\partial y} = 0 \qquad \text{irrotationality}$$

$$\frac{\partial v}{\partial y} + \frac{\partial u}{\partial x} = 0 \qquad \text{continuity}$$

The region is divided into three strips (Fig. 7), and the velocity components are approximated by trigonometric series (interpolation formulae) in the y-direction, i.e.

$$u(x,y) = \left(\frac{u_0}{6} + \frac{u_1}{3} + \frac{u_2}{3} + \frac{u_3}{6}\right) + \left(\frac{u_0}{3} + \frac{u_1}{3} - \frac{u_2}{3} - \frac{u_3}{3}\right)\cos \pi y$$
$$+ \left(\frac{u_0}{3} - \frac{u_1}{3} - \frac{u_2}{3} + \frac{u_3}{3}\right)\cos 2\pi y + \left(\frac{u_0}{6} - \frac{u_1}{3} + \frac{u_2}{3} - \frac{u_3}{6}\right)\cos 3\pi y$$

$$v(x,y) = \left(\frac{v_1}{\sqrt{3}} + \frac{v_2}{\sqrt{3}}\right)\sin \pi y + \left(\frac{v_1}{\sqrt{3}} - \frac{v_2}{\sqrt{3}}\right)\sin 2\pi y$$
$$+ \left(-\frac{v_1}{\sqrt{3}} + \frac{v_2}{3\sqrt{3}} + \frac{v_3}{3\pi}\right)\sin 3\pi y$$

where
$$u_i = u\left(x, \frac{i}{3}\right)$$
$$v_i = v\left(x, \frac{i}{3}\right)$$
and
$$v_3 = \left[\frac{\partial v(x,y)}{\partial y}\right]_{y=0}$$

The last quantity is added because it was found to improve the result sufficiently without having to increase the number of strips. The whole velocity field is then reduced to $u_i(x)$ and $v_i(x)$ which are velocity components along the strip lines and functions of one variable only. Substituting these series into the original equations and integrating from $y = 0$ to $y = \frac{i}{3}$, $(i = 1, 2, 3)$ we obtain a set of ordinary differential equations

$$\begin{bmatrix} 1 & 0 & 0 & 0 & 0 & 0 & 0 \\ \frac{1}{18}+\frac{\sqrt{3}}{4\pi} & \frac{1}{9}+\frac{\sqrt{3}}{12\pi} & \frac{1}{9}-\frac{\sqrt{3}}{4\pi} & \frac{1}{18}-\frac{\sqrt{3}}{12\pi} & 0 & 0 & 0 \\ \frac{1}{9}+\frac{\sqrt{3}}{12\pi} & \frac{2}{9}+\frac{\sqrt{3}}{4\pi} & \frac{2}{9}-\frac{\sqrt{3}}{12\pi} & \frac{1}{9}-\frac{\sqrt{3}}{4\pi} & 0 & 0 & 0 \\ \frac{1}{6} & \frac{1}{3} & \frac{1}{3} & \frac{1}{6} & 0 & 0 & 0 \\ 0 & 0 & 0 & 0 & \frac{7}{12\sqrt{3}\pi} & \frac{-1}{36\sqrt{3}\pi} & \frac{2}{9\pi^2} \\ 0 & 0 & 0 & 0 & \frac{9}{4\sqrt{3}\pi} & \frac{3}{4\sqrt{3}\pi} & 0 \\ 0 & 0 & 0 & 0 & \frac{4}{3\sqrt{3}\pi} & \frac{20}{9\sqrt{3}\pi} & \frac{2}{9\pi^2} \end{bmatrix} \times \begin{bmatrix} \frac{\partial u_0}{\partial x} \\ \frac{\partial u_1}{\partial x} \\ \frac{\partial u_2}{\partial x} \\ \frac{\partial u_3}{\partial x} \\ \frac{\partial v_1}{\partial x} \\ \frac{\partial v_2}{\partial x} \\ \frac{\partial v_3}{\partial x} \end{bmatrix} = \begin{bmatrix} -v_3 \\ -v_1 \\ -v_2 \\ 0 \\ u_1 - u_0 \\ u_2 - u_0 \\ u_3 - u_0 \end{bmatrix}$$

which reduces to

$$u_0' = -v_3$$

$$u_1' = v_3 - \frac{5\pi}{2\sqrt{3}} v_1 - \frac{\pi}{2\sqrt{3}} v_2$$

$$u_2' = -v_3 + \frac{9\pi}{2\sqrt{3}} v_1 - \frac{3\pi}{2\sqrt{3}} v_2$$

$$u_3' = v_3 - \frac{4\pi}{\sqrt{3}} v_1 + \frac{4\pi}{\sqrt{3}} v_2$$

$$v_1' = \frac{\sqrt{3}\pi}{6}\left[-3u_0 + u_1 + 3u_2 - u_3\right]$$

$$v_2' = \frac{\sqrt{3}\pi}{6}\left[u_0 - 3u_1 - u_2 + 3u_3\right]$$

$$v_3' = \pi^2\left[-\frac{19}{6}u_0 + 4u_1 - \frac{4}{3}u_2 + \frac{u_3}{2}\right]$$

where primes denote differentiation.

In the curved part, the equations are:

$$\frac{\partial u}{\partial \theta} + \frac{\partial vr}{\partial r} = 0 \qquad \text{continuity}$$

$$\frac{\partial v}{\partial \theta} - \frac{\partial ur}{\partial r} = 0 \qquad \text{irrotationality}$$

The velocities are approximated here by polynomials in r instead of trigonometric series since $\frac{\partial u}{\partial y} \neq 0$ whereas in the straight portion $\frac{\partial u}{\partial y} = 0$. This region is again divided into strips (Fig. 7). Here,

$$u(r,\theta) = u_0 + \left(-\frac{11}{2}u_0 + 9u_1 - \frac{9}{2}u_2 + u_3\right)(r-r_0)$$

$$+ \left(9u_0 - \frac{45}{2}u_1 + 18u_2 - \frac{9}{2}u_3\right)(r-r_0)^2 + \left(-\frac{9}{2}u_0 + \frac{27}{2}u_1 - \frac{27}{2}u_2 + \frac{9}{2}u_3\right)(r-r_0)^3$$

$$v(r,\theta) = v_3(r-r_0) + \left(-\tfrac{11}{2}v_3 + 27v_1 - \tfrac{27}{4}v_2\right)(r-r_0)^2$$
$$+ \left(9v_3 - \tfrac{135}{2}v_1 + 27v_2\right)(r-r_0)^3 + \left(-\tfrac{9}{2}v_3 + \tfrac{81}{2}v_1 - \tfrac{81}{4}v_2\right)(r-r_0)^4$$

where,

$$u_i(\theta) = u(r_i,\theta)\ ,\ v_i(\theta) = v(r_i,\theta)\ ,\ v_3(\theta) = \left[\frac{\partial v}{\partial r}\right]_{r=r_0}\ ,\ r_i = r_0 + \frac{i}{3}$$

Since these interpolation formulae are different from those in the straight section, we can match the velocities only at the points y=0, 1/3, 2/3 and 1 at the junction. The velocity distribution across the junction is therefore not completely matched, but the discrepancy was found to be small. For example, assuming that $u_0 = u_1 = u_2 = u_3 = 1$ at $x = -\infty$, the mass flow in the straight section $\int_0^1 u(-\infty, y)\,dy = 1$, whereas the mass flow in the curve section was found to be $\frac{7.9953}{8} = 0.9994$. This small error can be tolerated since the method itself is not expected to be very accurate in view of the small number of strips used.

After integrating along the r direction and solving for the derivatives as in the straight section, we obtain a similar set of ordinary differential equations.

$$u_0' = -r_0 v_3$$
$$u_1' = \frac{r_0}{3}v_3 - \frac{3}{2}v_1 r_1 - \frac{3}{2}v_2 r_2$$
$$u_2' = -\frac{r_0}{3}v_3 + 6v_1 r_1 - 3v_2 r_2$$
$$u_3' = r_0 v_3 - \frac{27}{2}v_1 r_1 + \frac{27}{2}v_2 r_2$$
$$v_1' = -\frac{19}{9}u_0 r_0 + 3u_2 r_2 - \frac{8}{9}u_3 r_3$$
$$v_2' = \frac{8}{9}u_0 r_0 - 3u_1 r_1 + \frac{19}{9}u_3 r_3$$
$$v_3' = -\frac{111}{2}u_0 r_0 + 81u_1 r_1 - \frac{81}{2}u_2 r_2 + 15u_3 r_3$$

Since the two sets of differentials have constants coefficients, they can be solved quite readily. The solution, with uniform flow ($u_i = 1$) $v_i = 0$) at $x = -\infty$ in the straight section and symmetry in the curved section, is

$$v_1 = Ae^{\pi x} + Be^{2\pi x}$$

$$v_2 = Ae^{\pi x} - Be^{2\pi x}$$

$$v_3 = \frac{2\pi}{\sqrt{3}}Ae^{\pi x} + \frac{4\pi}{\sqrt{3}}Be^{2\pi x} + Ce^{3\pi x}$$

$$u_0 = 1 - \frac{2}{\sqrt{3}}Ae^{\pi x} - \frac{2}{\sqrt{3}}Be^{2\pi x} - \frac{C}{3\pi}e^{3\pi x}$$

$$u_1 = 1 - \frac{1}{\sqrt{3}}Ae^{\pi x} + \frac{1}{\sqrt{3}}Be^{2\pi x} + \frac{C}{3\pi}e^{3\pi x}$$

$$u_2 = 1 + \frac{1}{\sqrt{3}}Ae^{\pi x} + \frac{1}{\sqrt{3}}Be^{2\pi x} - \frac{C}{3\pi}e^{3\pi x}$$

$$u_3 = 1 + \frac{2}{\sqrt{3}}Ae^{\pi x} - \frac{2}{\sqrt{3}}Be^{2\pi x} + \frac{C}{3\pi}e^{3\pi x}$$

In the curved section,

$$v_1 = \alpha_1 \sinh M_1\theta + \alpha_2 \sinh M_2\theta + \alpha_3 \sinh M_3\theta$$

$$v_2 = G_1\alpha_1 \sinh M_1\theta + G_2\alpha_2 \sinh M_2\theta + G_3\alpha_3 \sinh M_3\theta$$

$$v_3 = H_1\alpha_1 \sinh M_1\theta + H_2\alpha_2 \sinh M_2\theta + H_3\alpha_3 \sinh M_3\theta$$

$$u_0 = F_{01}\alpha_1 \cosh M_1\theta + F_{02}\alpha_2 \cosh M_2\theta + F_{03}\alpha_3 \cosh M_3\theta$$

$$u_1 = F_{11}\alpha_1 \cosh M_1\theta + F_{12}\alpha_2 \cosh M_2\theta + F_{13}\alpha_3 \cosh M_3\theta$$

$$u_2 = F_{21}\alpha_1 \cosh M_1\theta + F_{22}\alpha_2 \cosh M_2\theta + F_{23}\alpha_3 \cosh M_3\theta$$

$$u_3 = F_{31}\alpha_1 \cosh M_1\theta + F_{32}\alpha_2 \cosh M_2\theta + F_{33}\alpha_3 \cosh M_3\theta$$

where A, B, C, α_1, α_2, α_3, α_4 are arbitrary constants and M, G, H, F are some algebraic combinations of r_i which are obtained during formulation of the solution. By equating the seven variables at the junction ($x = 0$ or $\theta = \frac{\pi}{4}$), the seven arbitrary constants are obtained, giving the solution for the entire flow field. The pressure coefficients obtained from this solution is compared with those obtained from the Rayleigh-Ritz method in Fig. 8. The agreement is seen to be quite good and it was concluded that the method is probably accurate enough to apply to the compressible MHD flow.

3.3 Compressible MHD Flow Around Bend

Neglecting Hall and ion slip effects and assuming a small magnetic Reynolds number, the set of equations governing compressible MHD flow is

(1)

$$\rho \bar{V} \cdot \nabla \bar{V} + \nabla p = \sigma(\bar{V} \times \bar{B}) \times \bar{B} \qquad \text{momentum}$$

$$\nabla \cdot (\rho \bar{V}) = 0 \qquad \text{mass}$$

$$p = \rho R T \qquad \text{state (assuming perfect gas)}$$

$$C_v \rho T \, V \cdot \nabla S = \sigma(\bar{V} \times \bar{B})^2 \qquad \text{energy}$$

$$\frac{p}{p_\infty}\left(\frac{\rho_\infty}{\rho}\right)^{\gamma} = e^{\frac{s - s_\infty}{c_v}} \qquad \text{entropy}$$

$$\bar{J} = \sigma(\bar{V} \times \bar{B}) \qquad \text{ohm's law}$$

Combining the momentum and energy equations we obtain,

$$\bar{V} \cdot \nabla \frac{V^2}{2} + \bar{V} \cdot \nabla \frac{\gamma}{\gamma - 1} \frac{p}{\rho} = 0$$

$$\therefore \quad \frac{2\gamma}{\gamma - 1} \frac{p}{\rho} + V^2 = K \quad , \text{ a constant}$$

This is what is expected since a magnetic field alone cannot add energy to the flow.

The energy equation can then be eliminated, and the set of equations simplified to a form suitable for applying the method of integral relations. In the straight section,

$$\frac{\partial \rho(K+\frac{\gamma+1}{\gamma-1}u^2-v^2)}{\partial x} + \frac{2\gamma}{\gamma-1}\frac{\partial \rho u v}{\partial y} = -\frac{2\gamma}{\gamma-1}S(uB_y - vB_x)B_y$$

$$\frac{\partial \rho u v}{\partial x} + \frac{\gamma-1}{2\gamma}\frac{\partial \rho(K-u^2+\frac{\gamma+1}{\gamma-1}v^2)}{\partial y} = S(uB_y - vB_x)B_x \; .$$

$$\frac{\partial \rho u}{\partial x} + \frac{\partial \rho v}{\partial y} = 0$$

In the above equations all the variables are non-dimensionalized with corresponding quantities at upstream infinity, and $S = \frac{\sigma B_\infty^2 D}{\rho_\infty u_\infty^2}$ is the interaction parameter. The dependent variables are approximated along the y-direction as before, bearing in mind the boundary conditions at the walls.

$$\rho(K+\tfrac{\gamma+1}{\gamma-1}u^2-v^2) = \tfrac{1}{6}\Big[\rho_0(K+\tfrac{\gamma+1}{\gamma-1}u_0^2) + 2\rho_1(K+\tfrac{\gamma+1}{\gamma-1}u_1^2-v_1^2)$$

$$+ 2\rho_2(K+\tfrac{\gamma+1}{\gamma-1}u_2^2-v_2^2) + \rho_3(K+\tfrac{\gamma+1}{\gamma-1}u_3^2)\Big]$$

$$+\tfrac{1}{3}\Big[\rho_0(K+\tfrac{\gamma+1}{\gamma-1}u_0^2)+\rho_1(K+\tfrac{\gamma+1}{\gamma-1}u_1^2-v_1^2)-\rho_2(K+\tfrac{\gamma+1}{\gamma-1}u_2^2-v_2^2)-\rho_3(K+\tfrac{\gamma+1}{\gamma-1}u_3^2)\Big]\cos\pi y$$

$$+\tfrac{1}{3}\Big[\rho_0(K+\tfrac{\gamma+1}{\gamma-1}u_0^2)-\rho_1(K+\tfrac{\gamma+1}{\gamma-1}u_1^2-v_1^2)-\rho_2(K+\tfrac{\gamma+1}{\gamma-1}u_2^2-v_2^2)+\rho_3(K+\tfrac{\gamma+1}{\gamma-1}u_3^2)\Big]\cos 2\pi y$$

$$+\tfrac{1}{6}\Big[\rho_0(K+\tfrac{\gamma+1}{\gamma-1}u_0^2)-2\rho_1(K+\tfrac{\gamma+1}{\gamma-1}u_1^2-v_1^2)+2\rho_2(K+\tfrac{\gamma+1}{\gamma-1}u_2^2-v_2^2)-\rho_3(K+\tfrac{\gamma+1}{\gamma-1}u_3^2)\Big]\cos 3\pi y$$

ρu is expanded likewise.

$$\rho u v = \frac{1}{\sqrt{3}}(\rho_1 u_1 v_1 + \rho_2 u_2 v_2)\sin \pi y + \frac{1}{\sqrt{3}}(\rho_1 u_1 v_1 - \rho_2 u_2 v_2)\sin 2\pi y$$

$$+ \frac{1}{\sqrt{3}}\left(-\rho_1 u_1 v_1 + \frac{1}{3}\rho_2 u_2 v_2 + \frac{\rho_0 u_0 v_3}{\sqrt{3}\pi}\right)\sin 3\pi y$$

$$(uB_y - vB_x)B_y = \frac{1}{3}\left[(u_1 B_{y_1} - v_1 B_{x_1})B_{y_1} + (u_2 B_{y_2} - v_2 B_{x_2})B_{y_2}\right]$$

$$+ \frac{1}{3}\left[(u_1 B_{y_1} - v_1 B_{x_1})B_{y_1} - (u_2 B_{y_2} - v_2 B_{x_2})B_{y_2}\right]\cos \pi y$$

$$+ \frac{1}{3}\left[-(u_1 B_{y_1} - v_1 B_{x_1})B_{y_1} - (u_2 B_{y_2} - v_2 B_{x_2})B_{y_2}\right]\cos 2\pi y \qquad (2)$$

$$+ \frac{1}{3}\left[-(u_1 B_{y_1} - v_1 B_{x_1})B_{y_1} + (u_2 B_{y_2} - v_2 B_{x_2})B_{y_2}\right]\cos 3\pi y$$

$$(uB_y - vB_x)B_x = \left[(u_1 B_{y_1} - v_1 B_{x_1})B_{x_1} + (u_2 B_{y_2} - v_2 B_{x_2})B_{x_2}\right]\frac{\sin \pi y}{\sqrt{3}}$$

$$+ \left[(u_1 B_{y_1} - v_1 B_{x_1})B_{x_1} - (u_2 B_{y_2} - v_2 B_{x_2})B_{x_2}\right]\frac{\sin 2\pi y}{\sqrt{3}}$$

$$+ \left[-(u_1 B_{y_1} - v_1 B_{x_1})B_{x_1} + (u_2 B_{y_2} - v_2 B_{x_2})B_{x_2} + \frac{B_{x_0}\left(u_0 \left\{\frac{\partial B_y}{\partial y}\right\}_{y=0} - B_{x_0} v_3\right)}{\sqrt{3}\pi}\right]\frac{\sin 3\pi y}{\sqrt{3}}$$

These equations were substituted into the partial differential equations which were then integrated as before from $y = 0$ to $y = \frac{i}{3}$, $i = 1, 2, 3$. After some manipulation of the algebra, we find:

$$
\left.
\begin{aligned}
\frac{d}{dx}\left[\rho_0\left(K + \frac{\gamma+1}{\gamma-1}u_0^2\right)\right] &= -\frac{2\gamma}{\gamma-1}\rho_0 u_0 v_3 = \alpha_0 \\
\frac{d}{dx}\left[\rho_1\left(K + \frac{\gamma+1}{\gamma-1}u_1^2 - v_1^2\right)\right] &= \frac{2\gamma}{\gamma-1}\left[\rho_0 u_0 v_3 - \frac{5\pi}{2\sqrt{3}}\rho_1 u_1 v_1 - \frac{\pi}{2\sqrt{3}}\rho_2 u_2 v_2 - S(u_1 B_{y_1} - v_1 B_{x_1})B_{y_1}\right] = \alpha_1 \\
\frac{d}{dx}\left[\rho_2\left(K + \frac{\gamma+1}{\gamma-1}u_2^2 - v_2^2\right)\right] &= \frac{2\gamma}{\gamma-1}\left[-\rho_0 u_0 v_3 + \frac{9\pi}{2\sqrt{3}}\rho_1 u_1 v_1 - \frac{3\pi}{2\sqrt{3}}\rho_2 u_2 v_2 - S(u_2 B_{y_2} - v_2 B_{x_2})B_{y_2}\right] = \alpha_2 \\
\frac{d}{dx}\left[\rho_3\left(K + \frac{\gamma+1}{\gamma-1}u_3^2\right)\right] &= \frac{2\gamma}{\gamma-1}\left[\rho_0 u_0 v_3 - \frac{4\pi}{\sqrt{3}}\rho_1 u_1 v_1 + \frac{4\pi}{\sqrt{3}}\rho_2 u_2 v_2\right] = \alpha_3 \\
\frac{d}{dx}\left[\rho_0 u_0\right] &= -\rho_0 v_3 = \xi_0 \\
\frac{d}{dx}\left[\rho_1 u_1\right] &= \rho_0 v_3 - \frac{5\pi}{2\sqrt{3}}\rho_1 v_1 - \frac{\pi}{2\sqrt{3}}\rho_2 v_2 = \xi_1 \\
\frac{d}{dx}\left[\rho_2 u_2\right] &= -\rho_0 v_3 + \frac{9\pi}{2\sqrt{3}}\rho_1 v_1 - \frac{3\pi}{2\sqrt{3}}\rho_2 v_2 = \xi_2 \\
\frac{d}{dx}\left[\rho_3 u_3\right] &= \rho_0 v_3 - \frac{4\pi}{\sqrt{3}}\rho_1 v_1 + \frac{4\pi}{\sqrt{3}}\rho_2 v_2 = \xi_3 \\
\frac{d}{dx}\left[\rho_1 u_1 v_1\right] &= -\frac{\gamma-1}{2\gamma}\,\frac{\sqrt{3}\pi}{6}\Big[-3\rho_0(K-u_0^2) + \rho_1\left(K-u_1^2+\frac{\gamma+1}{\gamma-1}v_1^2\right) \\
&\qquad + 3\rho_2\left(K-u_2^2+\frac{\gamma+1}{\gamma-1}v_2^2\right) - \rho_3(K-u_3^2)\Big] + S(u_1 B_{y_1} - v_1 B_{x_1})B_{x_1} = \beta_1 \\
\frac{d}{dx}\left[\rho_2 u_2 v_2\right] &= -\frac{\gamma-1}{2\gamma}\,\frac{\sqrt{3}\pi}{6}\Big[\rho_0(K-u_0^2) - 3\rho_1\left(K-u_1^2+\frac{\gamma+1}{\gamma-1}v_1^2\right) \\
&\qquad - \rho_2\left(K-u_2^2+\frac{\gamma+1}{\gamma-1}v_2^2\right) + 3\rho_3(K-u_3^2)\Big] + S(u_2 B_{y_2} - v_2 B_{x_2})B_{x_2} = \beta_2
\end{aligned}
\right\} \quad (3)
$$

$$
\frac{d}{dx}\left[\rho_0 u_0 v_3\right] = -\frac{\gamma-1}{2\gamma}\pi^2\left[-\frac{19}{6}\rho_0(K-u_0^2) + 4\rho_1\left(K-u_1^2+\frac{\gamma+1}{\gamma-1}v_1^2\right)\right.
$$

$$- \frac{4}{3}\rho_2\left(K - u_2^2 + \frac{\gamma+1}{\gamma-1}v_2^2\right) + \frac{1}{2}\rho_3\left(K - u_3^2\right)\Big] + S\left(u_0\left(\frac{\partial B_y}{\partial y}\right)_{y=0} - B_{x_0} v_3\right) = \beta_3$$

In the curved section, the governing equations are:

$$\left.\begin{aligned}
&\frac{\partial \rho\left(K + \frac{\gamma+1}{\gamma-1}u^2 - v^2\right)}{\partial \theta} + \frac{2\gamma}{\gamma-1}\,\frac{\partial \rho u v r}{\partial r} = -\frac{2\gamma}{\gamma-1}\rho u v - \frac{2\gamma}{\gamma-1}\sigma(uB_r - vB_\theta)B_r \cdot r \\
&\frac{\partial \rho u v}{\partial \theta} + \frac{\gamma-1}{2\gamma}\,\frac{\partial \rho\left(K + \frac{\gamma+1}{\gamma-1}v^2 - u^2\right)}{\partial r} = \frac{\gamma-1}{2\gamma}\rho\left(K + \frac{\gamma+1}{\gamma-1}u^2 - v^2\right) + \sigma(uB_r - vB_\theta)B_\theta \cdot r \\
&\frac{\partial \rho u}{\partial \theta} + \frac{\partial \rho u v r}{\partial r} = 0
\end{aligned}\right\} \quad (4)$$

The dependent variables are approximated by series in r as before:

$$\begin{aligned}
\rho\left(K + \frac{\gamma+1}{\gamma-1}u^2 - v^2\right) = {} & \rho_0\left(K + \frac{\gamma+1}{\gamma-1}u_0^2\right) + \Big[-\frac{11}{2}\rho_0\left(K + \frac{\gamma+1}{\gamma-1}u_0^2\right) + 9\rho_1\left(K + \frac{\gamma+1}{\gamma-1}u_1^2 - v_1^2\right) \\
& - \frac{9}{2}\rho_2\left(K + \frac{\gamma+1}{\gamma-1}u_2^2 - v_2^2\right) + \rho_3\left(K + \frac{\gamma+1}{\gamma-1}u_3^2\right)\Big](r - r_0) \\
& + \Big[9\rho_0\left(K + \frac{\gamma+1}{\gamma-1}u_0^2\right) - \frac{45}{2}\rho_1\left(K + \frac{\gamma+1}{\gamma-1}u_1^2 - v_1^2\right) + 18\rho_2\left(K + \frac{\gamma+1}{\gamma-1}u_2^2 - v_2^2\right) - \frac{9}{2}\rho_3\left(K + \frac{\gamma+1}{\gamma-1}u_3^2\right)\Big](r - r_0)^2 \\
& + \Big[-\frac{9}{2}\rho_0\left(K + \frac{\gamma+1}{\gamma-1}u_0^2\right) + \frac{27}{2}\rho_1\left(K + \frac{\gamma+1}{\gamma-1}u_1^2 - v_1^2\right) - \frac{27}{2}\rho_2\left(K + \frac{\gamma+1}{\gamma-1}u_2^2 - v_2^2\right) + \frac{9}{2}\rho_3\left(K + \frac{\gamma+1}{\gamma-1}u_3^2\right)\Big](r - r_0)^3
\end{aligned}$$

ρu is expanded likewise.

$$
\left.
\begin{aligned}
\rho u v &= \rho_0 u_0 v_3 (r-r_0) + \left[-\tfrac{11}{2}\rho_0 u_0 v_3 + 27\rho_1 u_1 v_1 - \tfrac{27}{4}\rho_2 u_2 v_2\right](r-r_0)^2 \\
&\quad + \left[9\rho_0 u_0 v_3 - \tfrac{135}{2}\rho_1 u_1 v_1 + 27\rho_2 u_2 v_2\right](r-r_0)^3 \\
&\quad + \left[-\tfrac{9}{2}\rho_0 u_0 v_3 + \tfrac{81}{2}\rho_1 u_1 v_1 - \tfrac{81}{4}\rho_2 u_2 v_2\right](r-r_0)^4 \\
(uB_r - vB_\theta)B_r \cdot r &= \left[9(u_1 B_{r_1} - v_1 B_{\theta_1})B_{r_1}\cdot r_1 - \tfrac{9}{2}(u_2 B_{r_2} - v_2 B_{\theta_2})B_{r_2}\cdot r_2\right](r-r_0) \\
&\quad + \left[-\tfrac{45}{2}(u_1 B_{r_1} - v_1 B_{\theta_1})B_{r_1} r_1 + 18(u_2 B_{r_2} - v_2 B_{\theta_2})B_{r_2}\cdot r_2\right](r-r_0)^2 \\
&\quad + \left[\tfrac{27}{2}(u_1 B_{r_1} - v_1 B_{\theta_1})B_{r_1}\cdot r_1 - \tfrac{27}{2}(u_2 B_{r_2} - v_2 B_{\theta_2})B_{r_2}\cdot r_2\right](r-r_0)^3
\end{aligned}
\right\} \quad (5)
$$

$(uB_r - vB_\theta)B_\theta \cdot r$ is expanded as $\rho u v$

Substituting into the partial differential equations and integrating from $r = r_0$ to $r = r_0 + \frac{i}{3}$, $i = 1, 2, 3$, we obtain after some manipulation, a set of ordinary differential equations as those in the straight section.

$$\frac{d}{d\theta}\left[\rho_0\left(K + \frac{\gamma+1}{\gamma-1}u_0^2\right)\right] = -\frac{2\gamma}{\gamma-1}\rho_0 u_0 v_3 \cdot r_0 = \alpha_0$$

$$\frac{d}{d\theta}\left[\rho_1\left(K + \frac{\gamma+1}{\gamma-1}u_1^2 - v_1^2\right)\right] = \frac{2\gamma}{\gamma-1}\left[\left(\frac{r_0}{3} - \frac{1}{45}\right)\rho_0 u_0 v_3 - \left(\frac{3}{2}r_1 + \frac{4}{5}\right)\rho_1 u_1 v_1 + \left(\frac{3}{2}r_2 + \frac{1}{10}\right)\rho_2 u_2 v_2 - S(u_1 B_{r_1} - v_1 B_{\theta_1})B_{r_1}\cdot r_1\right] = \alpha_1$$

$$\frac{d}{d\theta}\left[\rho_2\left(K + \frac{\gamma+1}{\gamma-1}u_2^2 - v_2^2\right)\right] = \frac{2\gamma}{\gamma-1}\left[-\left(\frac{r_0}{3} - \frac{2}{45}\right)\rho_0 u_0 v_3 + \left(6r_1 - \frac{2}{5}\right)\rho_1 u_1 v_1 - \left(3r_2 + \frac{4}{5}\right)\rho_2 u_2 v_2 - S(u_2 B_{r_2} - v_2 B_{\theta_2})B_{r_2}\cdot r_2\right] = \alpha_2$$

$$\frac{d}{d\theta}\left[\rho_3\left(K+\frac{\gamma+1}{\gamma-1}u_3^2\right)\right] = \frac{2\gamma}{\gamma-1}\left[\left(r_0-\frac{1}{5}\right)\rho_0u_0v_3+\left(\frac{27}{2}r_1-\frac{9}{5}\right)\rho_1u_1v_1+\left(\frac{27}{2}r_2-\frac{9}{10}\right)\rho_2u_2v_2\right] = \alpha_3$$

$$\begin{aligned}
\frac{d}{d\theta}[\rho_0u_0] &= -\rho_0v_3\cdot r_0 = \xi_0 \\
\frac{d}{d\theta}[\rho_1u_1] &= -\frac{3}{2}\rho_1v_1r_1-\frac{3}{2}\rho_2v_2r_2+\frac{1}{3}\rho_0v_3r_0 = \xi_1 \\
\frac{d}{d\theta}[\rho_2u_2] &= 6\rho_1v_1r_1-3\rho_2v_2r_2-\frac{1}{3}\rho_0v_3r_0 = \xi_2 \\
\frac{d}{d\theta}[\rho_3u_3] &= -\frac{27}{2}\rho_1v_1r_1+\frac{27}{2}\rho_2v_2r_2+\rho_0v_3r_0 = \xi_3 \\
\frac{d}{d\theta}[\rho_1u_1v_1] &= \frac{\gamma-1}{2\gamma}\left[\frac{2}{9}\rho_0\left(K+\frac{\gamma+1}{\gamma-1}u_0^2\right)+\rho_1\left(K+\frac{\gamma+1}{\gamma-1}u_1^2-v_1^2\right)-\frac{1}{9}\rho_3\left(K+\frac{\gamma+1}{\gamma-1}u_3^2\right)\right]+S(u_1B_{r_1}-v_1B_{\theta_1})B_{\theta_1}\cdot r_1 \\
&\quad +\frac{\gamma-1}{2\gamma}\left[\frac{19}{9}\rho_0(K-u_0^2)r_0-3\rho_2\left(K-u_2^2+\frac{\gamma+1}{\gamma-1}v_2^2\right)r_2+\frac{8}{9}\rho_3(K-u_3^2)r_3\right] = \beta_1 \\
\frac{d}{d\theta}[\rho_2u_2v_2] &= \frac{\gamma-1}{2\gamma}\left[-\frac{1}{9}\rho_0\left(K+\frac{\gamma+1}{\gamma-1}u_0^2\right)+\rho_2\left(K+\frac{\gamma+1}{\gamma-1}u_2^2-v_2^2\right)+\frac{2}{9}\rho_3\left(K+\frac{\gamma+1}{\gamma-1}u_3^2\right)\right]+S(u_2B_{r_2}-v_2B_{\theta_2})B_{\theta_2}r_2 \\
&\quad +\frac{\gamma-1}{2\gamma}\left[-\frac{8}{9}\rho_0(K-u_0^2)r_0+3\rho_1\left(K-u_1^2+\frac{\gamma+1}{\gamma-1}v_1^2\right)r_1-\frac{19}{9}\rho_3(K-u_3^2)r_3\right] = \beta_2 \\
\frac{d}{d\theta}[\rho_0u_0v_3] &= \frac{\gamma-1}{2\gamma}\left[\frac{15}{2}\rho_0\left(K+\frac{\gamma+1}{\gamma-1}u_0^2\right)+9\rho_1\left(K+\frac{\gamma+1}{\gamma-1}u_1^2-v_1^2\right)-\frac{9}{2}\rho_2\left(K+\frac{\gamma+1}{\gamma-1}u_2^2-v_2^2\right)+3\rho_3\left(K+\frac{\gamma+1}{\gamma-1}u_3^2\right)\right] \\
&\quad +S\left(u_0\left(\frac{\partial B_r}{\partial r}\right)_{r=r_0}-B_{\theta_0}v_3\right)B_{\theta_0}r_0+\frac{\gamma-1}{2\gamma}\left[\frac{111}{2}\rho_0(K-u_0^2)r_0-81\rho_1\left(K-u_1^2+\frac{\gamma+1}{\gamma-1}v_1^2\right)r_1\right. \\
&\quad \left.+\frac{81}{2}\rho_2\left(K-u_2^2+\frac{\gamma+1}{\gamma-1}v_2^2\right)-15\rho_3(K-u_3^2)r_3\right] = \beta_3
\end{aligned} \tag{6}$$

The two sets of equations (3) and (6) are similar and can be reduced to yield the derivatives of the invididual dependent variables.

$$\left.\begin{aligned}
Du_0 &= \frac{K-u_0^2}{\rho_0\left(K-\frac{\gamma+1}{\gamma-1}u_0^2\right)}\cdot\xi_0 \\
D\rho_0 &= -\frac{3u_0}{K-\frac{\gamma+1}{\gamma-1}u_0^2}\cdot\xi_0 \\
Dv_3 &= \frac{1}{\rho_0 u_0}\left[\beta_3 - v_3\xi_0\right] \\
D\rho_3 &= \frac{1}{K-\frac{\gamma+1}{\gamma-1}u_3^2}\left[\alpha_3 - 2\cdot\frac{\gamma+1}{\gamma-1}\xi_3 u_3\right] \\
Du_3 &= \frac{1}{\rho_3\left(K-\frac{\gamma+1}{\gamma-1}u_3^2\right)}\left[K\xi_3 + \frac{\gamma+1}{\gamma-1}u_3^2\xi_3 - \alpha_3 u_3\right] \\
D\rho_i &= \frac{1}{K-\frac{\gamma+1}{\gamma-1}u_i^2-v_i^2}\left[\alpha_i - 2\frac{\gamma+1}{\gamma-1}\xi_i u_i + \frac{2v_i}{u_i}\left(\beta_i - v_i\xi_i\right)\right] \\
Du_i &= \frac{1}{\rho_i\left(K-\frac{\gamma+1}{\gamma-1}u_i^2-v_i^2\right)}\left[K\xi_i + \frac{\gamma+1}{\gamma-1}\xi_i u_i - \alpha_i u_i + \xi_i v_i^2 - 2v_i\beta_i\right] \\
Dv_i &= \frac{1}{\rho_i u_i}\left[\beta_i - v_i\xi_i\right] \qquad , \qquad i = 1, 2
\end{aligned}\right\} \quad (7)$$

'D' denotes differentiation with respect to x or θ, and α_i, β_i, ξ_i are functions of ρ_i, u_i, v_i as defined in equations (3) or (6), depending on whether they are applied in the straight or curved section. The set of equation (7) looks quite tedious, but it is actually quite simple to solve on the computer. The magnetic field intensity components B_x and B_y are simply equal in form to u and v as calculated in the incompressible flow case, since for a tightly wound coil around the bend, the magnetic field intensity satisfies the same equations and boundary conditions.

The set of equations (7) contains seven unknown variables which have to be integrated from $x = -\infty$ upstream, around the bend and to $x = +\infty$ in the downstream straight section. The boundary conditions are (i) uniform flow at upstream ∞, i.e. $u_i = 1$, $\rho_i = 1$, $v_i = 0$, $x = -\infty$ and (ii) parallel flow downstream infinity, i.e. $v_i = 0$, $x = \infty$ in downstream straight section.

Since we cannot actually integrate starting from and ending at infinity, which are singular points anyway, we have to arbitrarily terminate the region at some large finite values of x at both ends. To get the boundary conditions at these points, we find the asymptotic solutions of equation (1), valid for $x \to \infty$ in the upstream section and $x \to \infty$ in the downstream section, and require that they match the solution obtained by the method of integral relations. At large distances upstream, where the flow and magnetic field are approximately uniform and parallel, we can linearize the differential equations (1) by putting

$$u = 1 + u'$$

$$\rho = 1 + \rho'$$

$$v = v'$$

$$B_y = B_y'$$

$$B_x = 1 + B_x'$$

where the prime denotes perturbation quantities ($\ll 1$ and $\to 0$ as $x \to \infty$) Equation (1) then reduces to the following after some manipulation,

$$\text{(8)}\quad \begin{aligned} &a. \quad M_\infty^2 u' + \rho' = 0 \\ &b. \quad (1-M_\infty^2)\frac{\partial u'}{\partial x} + \frac{\partial v'}{\partial y} = 0 \\ &c. \quad \frac{\partial v'}{\partial x} - \frac{\partial u'}{\partial y} = S(\beta_y' - v') \end{aligned}$$

where M is the Mach number at upstream infinity, and

$$\beta_y' = -\sum n\pi a_n e^{n\pi x} \sin n\pi y$$

as obtained in section 2.2.1.

Equations (8b) and (8c) are solved to give a single equation in v',

$$\frac{\partial^2 v'}{\partial x} + \frac{1}{1-M_\infty^2}\frac{\partial^2 v'}{\partial y^2} + S\frac{\partial v'}{\partial x} = S\frac{\partial \beta_y'}{\partial x}$$

Using a Fourier sine transform, the complete solutions for (8) can be obtained giving the linearized solution for the equation (1) valid at large negative x.

$$\text{(9)}\begin{cases} v = \sum_p \left[A_p e^{\left[-\frac{S}{2}+\frac{1}{2}\sqrt{S^2+\frac{4p\pi^2}{1-M_\infty^2}}\right]x} - \dfrac{(1-M_\infty^2)S a_p \cdot p\pi}{(1-M_\infty^2)S - M_\infty^2 \cdot p\pi} e^{p\pi x}\right] \sin p\pi y \\ u = 1 - \sum_p \left[\dfrac{p\pi A_p}{(1-M_\infty^2)\left[-\frac{S}{2}+\frac{1}{2}\sqrt{S^2+\frac{4p\pi^2}{1-M_\infty^2}}\right]} e^{\left[-\frac{S}{2}+\frac{1}{2}\sqrt{S^2+\frac{4p\pi^2}{1-M_\infty^2}}\right]x} - \dfrac{S a_p \cdot p\pi\, e^{p\pi x}}{(1-M_\infty^2)S - M_\infty^2 p\pi}\right] \cos p\pi y \end{cases}$$

where a_p are given constants as calculated in section 2.2.1 and A_p are arbitrary constants depending on the conditions at the downstream end. In the method of integral relations, u and v are approximated by:

$$
(10)\begin{cases}
u = \left(\frac{u_0}{6} + \frac{u_1}{3} + \frac{u_2}{3} + \frac{u_3}{6}\right) + \left(\frac{u_0}{3} + \frac{u_1}{3} - \frac{u_2}{3} - \frac{u_3}{3}\right)\cos \pi y \\
\qquad + \left(\frac{u_0}{3} - \frac{u_1}{3} - \frac{u_2}{3} + \frac{u_3}{3}\right)\cos 2\pi y + \left(\frac{u_0}{6} - \frac{u_1}{3} + \frac{u_2}{3} - \frac{u_3}{6}\right)\cos 3\pi y \\
v = \left(\frac{v_1}{\sqrt{3}} + \frac{v_2}{\sqrt{3}}\right)\sin \pi y + \left(\frac{v_1}{\sqrt{3}} - \frac{v_2}{\sqrt{3}}\right)\sin 2\pi y + \left(-\frac{v_1}{\sqrt{3}} + \frac{v_2}{2\sqrt{3}} + \frac{v_3}{3\pi}\right)\sin 3\pi y
\end{cases}
$$

Comparing equations (9) and (10), we get

$$\frac{u_0}{6} + \frac{u_1}{3} + \frac{u_2}{3} + \frac{u_3}{6} = 1$$

$$\frac{u_0}{3} + \frac{u_1}{3} - \frac{u_2}{3} - \frac{u_3}{3} = -\left[\frac{\pi A_1 e^{\left(-\frac{S}{2} + \frac{1}{2}\sqrt{S^2 + \frac{4\pi^2}{1-M_\infty^2}}\right)x}}{(1-M_\infty^2)\left(-\frac{S}{2} + \frac{1}{2}\sqrt{S^2 + \frac{4\beta\pi^2}{1-M_\infty^2}}\right)} - \frac{S a_1 \pi}{(1-M_\infty^2)S - M_\infty^2 \pi} e^{\pi x}\right]$$

$$\frac{v_1}{\sqrt{3}} + \frac{v_2}{\sqrt{3}} = A_1 e^{\left[-\frac{S}{2} + \frac{1}{2}\sqrt{S^2 + \frac{4\pi^2}{1-M_\infty^2}}\right]x} - \frac{(1-M_\infty^2) S a_1 \pi}{(1-M_\infty^2)S - M_\infty^2 \pi} e^{\pi x}$$

The remaining expressions can be formed in the same way. To accommodate the boundary conditions that u_i and v_i must satisfy, the arbitrary constants A_p x ep(x) are eliminated, yielding the following four relations:

$$
\begin{aligned}
u_0 = 1 &+ \left[P_3 - P_1 - P_2\right]\frac{v_1}{\sqrt{3}} - \left[\frac{P_3}{3} + P_1 - P_2\right]\frac{v_2}{\sqrt{3}} - P_3 \cdot \frac{v_3}{3\pi} \\
&+ \left[Q_3 - Q_1 - Q_2\right]\frac{\beta_{y_1}}{\sqrt{3}} - \left[\frac{Q_3}{3} + Q_1 - Q_2\right]\frac{\beta_{y_2}}{\sqrt{3}} - Q_3 \cdot \frac{\beta_{y_3}}{3\pi}
\end{aligned}
$$

$$
(11)\begin{cases}
u_1 = 1 + \left[-P_3 - \frac{P_1}{2} + \frac{P_2}{2}\right]\frac{v_1}{\sqrt{3}} + \left[\frac{P_3}{3} - \frac{P_1}{2} - \frac{P_2}{2}\right]\frac{v_2}{\sqrt{3}} + P_3 \cdot \frac{v_3}{3\pi} \\
\qquad + \left[-Q_3 - \frac{Q_1}{2} + \frac{Q_2}{2}\right]\frac{B_{y_1}}{\sqrt{3}} + \left[\frac{Q_3}{3} - \frac{Q_1}{2} - \frac{Q_2}{2}\right]\frac{B_{y_2}}{\sqrt{3}} + Q_3\frac{B_{y_3}}{3\pi} \\
u_2 = 1 + \left[P_3 + \frac{P_1}{2} + \frac{P_2}{2}\right]\frac{v_1}{\sqrt{3}} - \left[\frac{P_3}{3} - \frac{P_1}{2} + \frac{P_2}{2}\right]\frac{v_2}{\sqrt{3}} - P_3\frac{v_3}{3\pi} \\
\qquad + \left[Q_3 + \frac{Q_1}{2} + \frac{Q_2}{2}\right]\frac{B_{y_1}}{\sqrt{3}} - \left[\frac{Q_3}{3} - \frac{Q_1}{2} + \frac{Q_2}{2}\right]\frac{B_{y_2}}{\sqrt{3}} - Q_3 \cdot \frac{B_{y_3}}{3\pi} \\
u_3 = 1 - \left[P_3 - P_1 + P_2\right]\frac{v_1}{\sqrt{3}} + \left[\frac{P_3}{3} + P_1 + P_2\right]\frac{v_2}{\sqrt{3}} + P_3 \cdot \frac{v_3}{3\pi} \\
\qquad - \left[Q_3 - Q_1 + Q_2\right]\frac{B_{y_1}}{\sqrt{3}} + \left[\frac{Q_3}{3} + Q_1 + Q_2\right]\frac{B_{y_2}}{\sqrt{3}} + Q_3 \cdot \frac{B_{y_3}}{3\pi}
\end{cases}
$$

and from equation (8a),

$$\rho_i = 1 + \rho_i' = 1 - M_\infty^2 u_i' = 1 + M_\infty^2 - M_\infty^2 u_i \quad , \quad i = 0, 1, 2, 3$$

Here, B_{y_i} are the transverse magnetic field intensity along the strip lines, and:

$$P_i = \frac{i\pi}{(1-M_\infty^2)\left(-\frac{S}{2} + \frac{1}{2}\sqrt{S^2 + \frac{4i^2\pi^2}{1-M_\infty^2}}\right)}$$

$$Q_i = \frac{S}{(1-M_\infty^2)S - M_\infty^2 i\pi}\left[1 - \frac{i\pi}{-\frac{S}{2} + \frac{1}{2}\sqrt{S^2 + \frac{4i^2\pi^2}{1-M_\infty^2}}}\right]$$

$$i = 1, 2, 3$$

Equation (11) gives eight conditions for the eleven unknowns, at some arbitrary large negative x, the other three conditions are obtained from the downstream section.

At downstream infinity the boundary conditions are: parallel flow, i.e. $v = 0$ and $\frac{\partial p}{\partial y} = 0$. Assuming that the variables reach some average values with only small fluctuations at large x, we put

$$u = U + u'$$

$$\rho = R + \rho'$$

$$p = P + p'$$

$$v = v'$$

where P, U, and R are average pressure, velocity and density at downstream infinity.

Here, $v' \rightarrow 0$, but we cannot assume u' $\rho' \rightarrow 0$ as $x \rightarrow \infty$ as in the upstream case, because the hydromagnetic interaction would have altered the flow field and a shear flow is possible downstream. Substituting as before into the governing equations and solving we get

$$v' = \sum_p \left[A_p e^{-\frac{1}{2}\left[(\bar{S}-2p\pi)+\sqrt{(\bar{S}-2p\pi)^2+4p\pi\left(\bar{S}+\frac{\bar{M}_\infty^2 p\pi}{1-\bar{M}_\infty^2}\right)}\right]x} + d_p \right] e^{-p\pi x} \sin p\pi y$$

where
$$\bar{S} = \frac{\sigma B_\infty^2 D}{RU}$$

$$\bar{M}_\infty^2 = \frac{RU^2}{\gamma P}$$

and $$d_p = \frac{\bar{S}\cdot p\pi}{\bar{S} - \frac{\bar{M}_\infty^2}{1-\bar{M}_\infty^2}p\pi} \cdot a_p$$ and A_p are arbitrary constants.

For a large enough value of x, we can assume the first term in v' to be negligible since the term in square brackets is always positive.

Therefore, as $x \to \infty$

$$v' = \Sigma d_p e^{p\pi x} \sin p\pi y$$

$$u' = \int \left[-\frac{1}{1-\bar{M}_\infty^2} \frac{\partial v'}{\partial y} \right] dx = \frac{1}{1-\bar{M}_\infty^2} \Sigma d_p e^{-p\pi x} \cos p\pi y + \Sigma \delta_p \cos p\pi y$$

$$\rho' = \frac{-\frac{R^2 U}{\gamma P}}{1-\bar{M}_\infty^2} \Sigma d_p e^{-p\pi x} \cos p\pi y + \frac{\gamma-1}{\gamma} \frac{R^2 U}{P} \Sigma \delta_p \cos p\pi y$$

where δ_p are arbitrary constants, which are eliminated by combining u' and ρ as follows,

$$u' - \frac{\gamma}{\gamma-1} \frac{P}{R^2 U} \rho' = \frac{\gamma}{\gamma-1} \frac{1}{1-\bar{M}_\infty^2} \Sigma d_p e^{-p\pi x} \cos p\pi y$$

Matching this solution with that obtained with the method of integral relations, we obtain as in the upstream case,

$$(12) \begin{cases} v_1 = \frac{1}{\sqrt{3}} \frac{\gamma-1}{\gamma} (1-\bar{M}_\infty^2) \left[\left\{ (u_0 - U) - \frac{1}{(\gamma-1)\bar{M}_\infty^2} \frac{\rho_0 - R}{R} \right\} - \left\{ (u_2 - U) - \frac{1}{(\gamma-1)\bar{M}_\infty^2} \cdot \frac{\rho_2 - R}{R} \right\} \right] \\ v_2 = \frac{1}{\sqrt{3}} \frac{\gamma-1}{\gamma} (1-\bar{M}_\infty^2) \left[\left\{ (u_1 - U) - \frac{1}{(\gamma-1)\bar{M}_\infty^2} \frac{\rho_1 - R}{R} \right\} - \left\{ (u_3 - U) - \frac{1}{(\gamma-1)\bar{M}_\infty^2} \cdot \frac{\rho_3 - R}{R} \right\} \right] \\ v_3 = \frac{\gamma-1}{\gamma} (1-\bar{M}_\infty^2) \pi \left[\frac{3}{2} \left\{ (u_0 - U) - \frac{1}{(\gamma-1)\bar{M}_\infty^2} \cdot \frac{\rho_0 - R}{R} \right\} \right. \\ \qquad \left. - \frac{4}{3} \left\{ (u_1 - U) - \frac{1}{(\gamma-1)\bar{M}_\infty^2} \cdot \frac{\rho_1 - R}{R} \right\} - \frac{1}{6} \left\{ (u_3 - U) - \frac{1}{(\gamma-1)\bar{M}_\infty^2} \frac{\rho_3 - R}{R} \right\} \right] \end{cases}$$

The quantities P, R, U are average values of p_i, ρ_i and u_i, but if the magnetic interaction is not large, we can assume they are the approximately the upstream quantities. Equation (12) provides the three equations in addition to the eight given by equation (11), giving a total of eleven equations for the eleven unknowns.

The case of compressible irrotational flow ($S = 0$) was solved first to see if any computational difficulty should arise. Here, because of symmetry, the downstream asymptotic conditions are not necessary, since $v = 0$ at $\theta = 0°$. A computer program for this non-linear two-point boundary value problem was written for the IBM 360 computer, and a brief description follows.

At some finite negative x upstream, some arbitrary values ov v_1, v_i, v_3 are assumed, and u_i and ρ_i are calculated according to equation (11). With these initial conditions equation (7) is integrated up to $\theta = 45°$, using the Runge-Kutta 4th order equations with 5th order corrections. The same procedure is repeated three times with different assumed initial values of v_1, v_2 and v_3. The next values of initial points v_1, v_2 and v_3 are then calculated according to Fox[24]. The process is repeated until $v_1 = v_2 = v_3 \sim 0$ at $\theta = 45°$. Unfortunately, except for very small values of M (10^{-8}), this process does not converge to give a solution. This is found to be due to the numerical instability of the system. As seen in section 2.2.2, the solution of the simpler incompressible case is in terms of $e^{\pm M_i \cdot \theta}$ where M_i depends on the radius of curvature r_o, and are fairly large for $r_o = 3$. For the compressible flow case, one would expect the same sort of dependence on θ, but with an even larger M_i, by drawing comparison with the fact that $v = \sum A_p e^{\frac{p\pi x}{\sqrt{1-M_o^2}}}$ (Eqn.9) for compressible flow and $v = \sum A_p e^{p\pi x}$ for incompressible flow. Therefore any error, either caused by assuming wrong values of v_i at the boundary, or by truncation or round-off in the computation, will grow exponentially according to $e^{M_i \theta}$, as θ increases. For sufficiently large M_i, this error eventually dominates and swamps the true solution (Fox [24]). To circumvent this difficulty, a method of successive approximation was adopted. Hence, we linearized the differential equations (7) and boundary conditions (11) and (12) by assuming

$$u_i = U_i + u_i'$$
$$v_i = V_i + v_i'$$
$$\rho_i = (1 + U_i^2 + V_i^2)^{\frac{1}{\gamma-1}} + \rho_i'$$

where U_i and V_i are the incompressible flow solutions. The same procedure is used to solve for u_i' , v_i' and ρ_i' . After this is done, we proceed to find the second approximation

$$u_i = (U_i + u_i') + u_i''$$
$$v_i = (V_i + v_i') + v_i''$$
$$\rho_i = (1 + U_i^2 + V_i^2)^{\frac{1}{\gamma-1}} + \rho_i' + \rho_i'', \quad \text{and so on.}$$

At every step of the approximation, a check on the accuracy was provided by calculating the error of the derivatives. For example, after second approximation the error in equation (7a) is

$$E_a = \left[DU_0 + DU_0' + DU_0''\right] - \frac{\left\{K - (U_0 + u_0' + u_0'')\right\} \cdot \xi_0 (U_i + u_i' + u_i'', V_i + v_i' + v_i'' \ldots)}{\left[\left\{1 + (U_0 + u_0' + u_0'')^2 + (V_0 + v_0' + v_0'')^2\right\}^{\frac{1}{\gamma-1}} + \rho_0' + \rho_0''\right] \cdot \left\{K - \frac{\gamma+1}{\gamma-1}(U_0 + u_0' + u_0'')^2\right\}}$$

The errors for the other equations in (7) are calculated similarly.

For upstream Mach numbers up to 0.5, the solutions converge quite well for both the irrotational and MHD case (S = 1.0), and the errors E_i are very small after the 2nd approximation. The pressure coefficients for $M_\infty = 0.5$ are shown in Figure 9. The effect of the magnetic field was seen to be quite small. It was thought that at this low Mach number, the flo· is too close to being incompressible and the stream lines therefo. coincide quite closely with the magnetic field lines, therefore producing very small $(\bar{V} \times \bar{B})$ fields. The same procedure was therefore tried for $M = 0.7$, but even the compressible irrotational case does not converge to a solution. Using other integrating schemes (e.g. Hamming's modified predictor-corrector method (Ralston and Wilf,25), does not improve the situation.

Instead of going into other schemes, it was decided to use the method of integral relations throughout. First the upstream semi-infinite region is transformed into a finite region by putting $\eta = e^{\pi x}$. This region is then divided by vertical strips $\eta = 1/3$ and $\eta = 2/3$, in addition to the horizontal strips $y = 1/3$ and $y = 2/3$ (Fig. 10). Here, instead, we shall use equation (3) for simplicity, and approximate α_i, ξ_i, and β_i in series of η. Since all the equations in (3) are of the same form, we shall just show one here. For example, equation (3h) is

$$\frac{d}{dx}[\rho_3 u_3] = \rho_0 v_3 - \frac{4\pi}{\sqrt{3}}\rho_1 v_1 + \frac{4\pi}{\sqrt{3}}\rho_2 v_2 = \xi_3$$

After transforming it becomes

$$\frac{d}{d\eta}[\rho_3 u_3] = \frac{1}{\eta}\cdot\frac{d}{dx}[\rho_3 u_3] = \frac{\xi_3}{\eta}$$

The unknowns are approximated by the interpolation formula:

$$\xi_3 = (9\xi_{31} - \tfrac{9}{2}\xi_{32} + \xi_{33})\eta + (-\tfrac{45}{2}\xi_{31} + 18\xi_{32} - \tfrac{9}{2}\xi_{33})\eta^2 + (\tfrac{27}{2}\xi_{31} - \tfrac{27}{2}\xi_{32} + \tfrac{9}{2}\xi_{33})\eta^3$$

where $\xi_{3i} = \rho_{0i} v_{3i} - \frac{4\pi}{\sqrt{3}} \rho_{1i} v_{1i} + \frac{4\pi}{\sqrt{3}} \rho_{2i} v_{2i}$

and ρ_{ji}, v_{ji} are the density and transverse velocity at $y = \frac{i}{3}$

and $\eta = \frac{i}{3}$.

After substituting into the differential equation and integrating from $\eta = \frac{1}{3}$ to $\eta = \frac{i}{3}$ where $i = 2, 3$, we obtain the following set of algebraic equations:

$$
\left\{
\begin{aligned}
&\rho_{ij}\left(K + \tfrac{\gamma+1}{\gamma-1}u_{ij}^2 - v_{ij}^2\right) - \rho_{i1}\left(K + \tfrac{\gamma+1}{\gamma-1}u_{i1}^2 - v_{i1}^2\right) = a_{i0}\left[B_{j1}\rho_{01}u_{01}v_{31} + B_{j2}\rho_{02}u_{02}v_{32} + B_{j3}\rho_{03}u_{03}v_{33}\right] \\
&\qquad + a_{i1}\left[B_{j1}\rho_{11}u_{11}v_{11} + B_{j2}\rho_{12}u_{12}v_{12} + B_{j3}\rho_{13}u_{13}v_{13}\right] \\
&\qquad + a_{i2}\left[B_{j1}\rho_{21}u_{21}v_{21} + B_{j2}\rho_{22}u_{22}v_{22} + B_{j3}\rho_{23}u_{23}v_{23}\right] \\
&\qquad - \frac{2\gamma}{\gamma-1}\cdot S\left[B_{j1}(u_{i1}B_{y_{i1}} - v_{i1}B_{x_{i1}})B_{y_{i1}} + B_{j2}(u_{i2}B_{y_{i2}} - v_{i2}B_{x_{i2}})B_{y_{i2}} + B_{j3}(u_{i3}B_{y_{i3}} - v_{i3}B_{x_{i3}})B_{y_{i3}}\right] \\
&\rho_{ij}u_{ij} - \rho_{i1}u_{i1} = a_{i0}\frac{2\gamma}{\gamma-1}\left[B_{j1}\rho_{01}v_{31} + B_{j2}\rho_{02}v_{32} + B_{j3}\rho_{03}v_{33}\right] \\
&\qquad + a_{i1}\frac{2\gamma}{\gamma-1}\left[B_{j1}\rho_{11}v_{11} + B_{j2}\rho_{12}v_{12} + B_{j3}\rho_{13}v_{13}\right] \\
&\qquad + a_{i2}\frac{2\gamma}{\gamma-1}\left[B_{j1}\rho_{21}v_{21} + B_{j2}\rho_{22}v_{22} + B_{j3}\rho_{23}v_{23}\right] \\
&\rho_{ij}u_{ij}v_{ij} - \rho_{i1}u_{i1}v_{i1} = c_{i0}\left[B_{j1}\rho_{01}(K - u_{01}^2) + B_{j2}(K - u_{02}^2)\rho_{02} + B_{j3}\rho_{03}(K - u_{03}^2)\right] \\
&\qquad + c_{i1}\left[B_{j1}\rho_{11}\left(K - u_{11}^2 + \tfrac{\gamma+1}{\gamma-1}v_{11}^2\right) + B_{j2}\rho_{12}\left(K - u_{12}^2 + \tfrac{\gamma+1}{\gamma-1}v_{12}^2\right) + B_{j3}\left(K - u_{13}^2 + \tfrac{\gamma+1}{\gamma-1}v_{13}^2\right)\rho_{13}\right] \\
&\qquad + c_{i2}\left[B_{j1}\rho_{21}\left(K - u_{21}^2 + \tfrac{\gamma+1}{\gamma-1}v_{21}^2\right) + B_{j2}\rho_{22}\left(K - u_{22}^2 + \tfrac{\gamma+1}{\gamma-1}v_{22}^2\right) + B_{j3}\rho_{23}\left(K - u_{23}^2 + \tfrac{\gamma+1}{\gamma-1}v_{23}^2\right)\right] \\
&\qquad + c_{i3}\left[B_{j1}\rho_{31}(K - u_{31}^2) + B_{j2}\rho_{32}(K - u_{32}^2) + B_{j3}\rho_{33}(K - u_{33}^2)\right] \\
&\qquad + S\left[B_{j1}(u_{i1}B_{y_{i1}} - v_{i1}B_{x_{i1}})B_{x_{i1}} + B_{j2}(u_{i2}B_{y_{i2}} - v_{i2}B_{x_{i2}})B_{x_{i2}} + B_{j3}(u_{i3}B_{y_{i3}} - v_{i3}B_{x_{i3}})B_{x_{i3}}\right]
\end{aligned}
\right. \tag{13}
$$

$$i = 0, 1, 2, 3 \qquad j = 1, 2, 3$$

The coefficients a_{i_j}, B_{i_j} and C_{i_j} are algebraic constants which are calculated during formulation of the above equations. The curved region is divided into twelve sections (Fig. 10) and the unknown functions in equation (6) are approximated by series of exponentials. For example, in equation (6h),

$$(14) \quad \xi_3 = \alpha_1 e^{-6\theta} + \alpha_2 e^{-5\theta} + \cdots \alpha_7 + \alpha_8 e^{\theta} + \alpha_9 e^{2\theta} + \cdots \alpha_{13} e^{7\theta}$$

After substituting and integrating from $\theta = -\frac{\pi}{4}$ to $-\frac{\pi}{4} + \frac{j\pi}{24}$, we obtain a similar set of algebraic equations as in (13). The downstream section is treated in the same way. The resulting set of algebraic equations is solved by linearizing and successive approximation. To check the accuracy of the method, the case for $M = 0.5$ was tried. It was found that when the curved region was divided into only six sections (i.e. the unknown functions expanded only to seven terms instead of 13 as in equation (14)), the results do not compare too well with that obtained before by integration. Since it does not involve any effort to change the computer program, the expression with 13 terms was used to ensure a good approximation. The result then obtained agreed well with previous result (Fig. 9). The pressure coefficients for the case $M = 0.7$ is shown in Figure 11, both for the irrotational and MHD case. It is seen that the effect of applying a magnetic field is small, and probably not large enough to be detected experimentally. Analysis of the computer results shows that even though the pressure coefficient profiles of compressible flow are different from the incompressible case, the difference in transverse velocity (v) is only to 1st order and is therefore very small. The inclination of the compressible flow stream line to the magnetic field line is therefore not enough to produce any sizeable induced current $\bar{J} = \sigma(\bar{V} \times \bar{B})$. It is obvious then, to change the pressure profiles significantly we have to drive a current through the plasma from some external source in order to produce a zero order effect.

3.4 Incompressible Flow Around Bend with External Current Source

In order not to complicate the problem, the simplest case is consiered here, that of an incompressible fluid flowing through a right angle bend, with an applied transverse electric field only in the curved section driving a constant current across the side walls (Fig. 12). Here again we employ both the Rayleigh-Ritz method and the method of integral relations as a check on each other to ensure a correct solution. In the method of integral relations, the following equations are used:

$$(15)\quad \left\{ \begin{aligned} &\frac{\partial(p+u^2)}{\partial x} + \frac{\partial uv}{\partial y} = 0 \\ &\frac{\partial uv}{\partial x} + \frac{\partial(p+v^2)}{\partial y} = 0 \\ &\frac{\partial u}{\partial x} + \frac{\partial v}{\partial y} = 0 \qquad \text{in straight sections} \end{aligned} \right.$$

$$(16)\quad \left\{ \begin{aligned} &\frac{\partial(p+u^2)}{\partial \theta} + \frac{\partial uvr}{\partial r} = -uv + S\cdot\left(\frac{D}{R_0}\right)B_r\cdot r \\ &\frac{\partial uv}{\partial \theta} + \frac{\partial(p+v^2)r}{\partial r} = p + u^2 - S\cdot\left(\frac{D}{R_0}\right)\cdot B_\theta\cdot r \\ &\frac{\partial u}{\partial \theta} + \frac{\partial vr}{\partial r} = 0 \qquad \text{in curved section} \end{aligned} \right.$$

where u, v = velocity components non-dimensionalized with respect to upstream velocity,

$$p = \frac{\text{pressure}}{\text{upstream dynamic pressure}} = \frac{\text{pressure}}{\rho_\infty u_\infty^2}$$

$$S = \frac{J B \ell}{\rho_\infty u_\infty^2}$$

The computer program developed for the compressible flow was employed here, and the pressure coefficients are given in Figure 13. In the Raleigh-Ritz method we follow the same procedure as in section 2.2.1. Consider the equations:

$$(17) \qquad \bar{V} \cdot \nabla \bar{V} + \frac{\nabla p}{\rho} = \frac{\bar{J} \times \bar{B}}{\rho}$$

$$\nabla \cdot V = 0$$

Taking the curl and combining the equations, we find

$$(18) \qquad \bar{V} \cdot \nabla \bar{\omega} = \frac{B_x}{\rho} \frac{\partial \bar{J}}{\partial x}$$

where $\omega = \nabla \times \bar{V}$ is the vorticity.

The other terms drop out since $\bar{\omega}$ and $\bar{J}$ have components in z-direction only.

At the junction between the straight and curved sections, it is assumed that the current jumps from zero to a constant value given by $\bar{J} = \sigma \bar{E}$, where $\bar{E}$ is the applied electric field. Therefore the vorticity $\bar{\omega}$ also jumps from zero to the value $\frac{J \cdot B_x(y)}{\rho \cdot u(y)}$ at the junction.

In the upstream straight section the governing equation is $\nabla^2 \psi = 0$ whereas in the other sections the governing equation is $\nabla^2 \psi = \omega(\psi)$ since from equation (18) $\bar{V} \cdot \nabla \bar{\omega} = 0$ because $\bar{J}$ is assumed constant in the bend. The form of solution in the straight section is that of section 2.2.1. In order to solve the MHD flow in the bend, we approximate ω as some function of ψ (say a polynomial in ψ) and solve the above equation, by successive approximation.

Assuming that ψ has an asymptotic expansion $\psi = \psi_0 + \epsilon\psi_1 + \cdots$ where ϵ is some small parameter defined later, the problem reduces to the following.

In upstream straight section: $\nabla^2\psi = \nabla^2\psi_0 + \epsilon\nabla^2\psi_1 + \cdots = 0$

$$(19)\quad \begin{cases} \nabla^2\psi_0 = 0 & \Rightarrow \quad \psi_0 = y + \sum a_n e^{\frac{n\pi x}{D}} \sin\frac{n\pi y}{D} \\ \nabla^2\psi_1 = 0 & \Rightarrow \quad \psi_1 = \sum a_n' e^{\frac{n\pi x}{D}} \sin\frac{n\pi y}{D} \end{cases}$$

At junction $(x = 0)$,

$$u = 1 + \sum n\pi a_n \cos\frac{n\pi y}{D} + \epsilon \sum n\pi a_n' \cos\frac{n\pi y}{D} + \cdots$$

$$v = -\sum n\pi a_n \sin\frac{n\pi y}{D} - \epsilon \sum n\pi a_n' \sin\frac{n\pi y}{D} + \cdots$$

$$B_x = 1 + \sum n\pi A_n \cos\frac{n\pi y}{D}$$

In the curved section:

At $\theta = -45^\circ$, $\omega = S\cdot\left(\frac{R_0}{D}\right)\cdot\frac{B_x}{u}$

$$(20)\qquad = S\left(\frac{R_0}{D}\right)\left[\frac{\frac{1}{D} + \sum n\pi A_n \cos\frac{n\pi y}{D}}{\frac{1}{D} + \sum n\pi a_n \cos\frac{n\pi y}{D} + \epsilon\sum n\pi a_n' \cos\frac{n\pi y}{D} + \cdots}\right]$$

$$= S\cdot\frac{R_0}{D}\cdot\left[1 + (A_1 - a_1)\frac{\sum n\pi \frac{A_n - a_n}{A_1 - a_1}\cos\frac{n\pi y}{D}}{\frac{1}{D} + \sum n\pi a_n \cos\frac{n\pi y}{D}} + \cdots\right]$$

approximating ω as a polynomial in ψ,

$$(21)\quad \omega = S\cdot\left(\frac{R_0}{D}\right)\cdot\left[1 + (A_1 - a_1)(\alpha\psi + \beta\psi^2 + \gamma\psi^3)\right]$$

$$= S \cdot \frac{\ell_0}{D} \cdot \Big[1 + (A_1 - a_1)\alpha \big(y + \sum a_n \sin \frac{n\pi y}{D} + \epsilon \sum a_n' \sin \frac{n\pi y}{D} + \dots \big)$$

$$+ (A_1 - a_1)\beta \big(y + \sum a_n \sin \frac{n\pi y}{D} + \epsilon \sum a_n' \sin \frac{n\pi y}{D} + \dots \big)^2$$

$$+ (A_1 - a_1)\gamma \big(y + \sum a_n \sin \frac{n\pi y}{D} + \epsilon \sum a_n' \sin \frac{n\pi y}{D} + \dots \big)^3 \Big]$$

Taking $\epsilon = A_1 - a_1$, the constants α, β, γ can be calculated if a_n are known.

The differential equation in the curved section is then

$$\nabla^2 \psi_0 + \epsilon \nabla^2 \psi_1 + \dots = \omega = S \left[1 + \epsilon (\alpha \psi_0 + \beta \psi_0^2 + \gamma \psi_0^3) + \dots \right]$$

The zero and first order solutions are:

$$\nabla^2 \psi_0 = S$$

$$\therefore \psi_0 = \sum\sum \alpha_{mn} \sin \frac{n\pi \ln r}{\ln R} \cos 2(2m-1)\theta + \frac{r-1}{D} \sum \left[\frac{p_n - a_n}{2 \sin \frac{n\pi}{4}} \sin n\theta + \frac{p_n + a_n}{2 \cos \frac{n\pi}{4}} \cos n\theta \right] \sin \frac{n\pi (r-1)}{D}$$

$$\nabla^2 \psi_1 = S (\alpha \psi_0 + \beta \psi_0^2 + \gamma \psi_0^3)$$

$$\therefore \psi_1 = \sum\sum \alpha_{mn}' \sin \frac{n\pi \ln r}{\ln R} \cos 2(2m-1)\theta + \frac{r-1}{D} \sum \left[\frac{p_n' - a_n'}{2 \sin \frac{n\pi}{4}} \sin n\theta + \frac{p_n' + a_n'}{2 \cos \frac{n\pi}{4}} \cos n\theta \right] \sin \frac{n\pi (r-1)}{D}$$

from which

$$v \doteq -\frac{1}{r} \Big[\sum\sum \alpha_{mn} \sin \frac{n\pi \ln r}{\ln R} \{-2(2m-1)\} \sin 2(2m-1)\theta + \sum n \Big\{ \frac{p_n - a_n}{2 \sin \frac{n\pi}{4}} \cos n\theta + \frac{p_n + a_n}{2 \cos \frac{n\pi}{4}} \sin n\theta \Big\} \sin \frac{n\pi (r-1)}{D}$$

$$+ \epsilon \sum\sum \alpha_{mn}' \sin \frac{n\pi \ln r}{\ln R} \{-2(2m-1)\} \sin 2(2m-1)\theta + \sum n \Big\{ \frac{p_n' - a_n'}{2 \sin \frac{n\pi}{4}} \cos n\theta + \frac{p_n' + a_n'}{2 \cos \frac{n\pi}{4}} \sin n\theta \Big\} \sin \frac{n\pi (r-1)}{D} \Big]$$

In the downstream section, the current is zero and the vorticity is reduced by $\frac{J}{\rho} \cdot \frac{B}{u}$. The equations are similar to upstream section.

The zero order is therefore:

$$\nabla^2 \psi_0 = 0 \qquad\qquad \psi_0 = y + \Sigma p_n e^{-n\pi x} \sin n\pi y$$

At $\quad x = 0 \quad , \quad v = \Sigma n\pi p_n \sin \frac{n\pi y}{D}$

Requiring that v be continuous at both junctions

$$-\Sigma n\pi a_n \sin \frac{n\pi y}{D} = \frac{1}{r} \Sigma\Sigma \alpha_{mn} \sin \frac{n\pi l_n r}{l_n R}\, 2(2m-1) \sin 2(2m-1)\frac{\pi}{4} - \frac{1}{r} \Sigma n \left\{ \frac{p_n - a_n}{2\sin\frac{n\pi}{4}} \cos\frac{n\pi}{4} + \frac{p_n + a_n}{2\cos\frac{n\pi}{4}} \sin\frac{n\pi}{4} \right\} \sin \frac{n\pi y}{D}$$

$$\Sigma n\pi p_n \sin \frac{n\pi y}{D} = -\frac{1}{r} \Sigma\Sigma \alpha_{mn} \sin \frac{n\pi l_n r}{l_n R}\, 2(2m-1) \sin 2(2m-1)\frac{\pi}{4} - \frac{1}{r} \Sigma n \left\{ \frac{p_n - a_n}{2\sin\frac{n\pi}{4}} \cos\frac{n\pi}{4} - \frac{p_n + a_n}{2\cos\frac{n\pi}{4}} \sin\frac{n\pi}{4} \right\} \sin \frac{n\pi y}{D}$$

Combining the two equations we find that $p_n = a_n$. The solution is therefore symmetric about $\theta = 0^{\circ}$ and the unknowns a_n can be found by forming the integral and finding the minimum as in section 2.2.1. With known values of a_n; α, β, γ are calculated from (21), and the first order solution is obtained by obtaining a_n' using the same procedure. The result obtained for $S = 0.6$, $\frac{R}{D} = 3.0$ is plotted in Figure (13), and even the zero order seems to agree quite well with the results from the method of integral relations. It was concluded therefore that the pressure coefficients calculated from the zero order equation are solutions to a sufficient degree of accuracy; so that for other values of interaction parameter, only the zero order solutions are computed.

4. EXPERIMENTS

4.1 Experimental Verification Using Two-Dimensional Flow of Electrolyte Around a Right-Angle Bend

As shown in section 3.4, the low-speed flow of plasma around a two-dimensional right-angle bend under applied, crossed electric and magnetic fields can be approximated by a simplified set of MHD equations, assuming incompressible flow of the plasma. In practice, the flow is complicated by side effects, such as non-uniformity of plasma temperature and conductivity, electrode effects (arcing and non-uniform current distribution), and sheath effects. Since the theory presupposes incompressible conditions, it seems justified to simulate the conducting plasma using aqueous electrolytes. A search of the electrochemical properties of various substances revealed the relative superiority of copper nitrate for the following reasons:

(1) The chemical compound is cheap and readily available in quantity.

(2) The solution of copper nitrate is safe to use (unlike acids or alkalines) and has fairly low resistivity.

(3) Using copper electrodes, the passage of current does not result in net production of new substances, hence no polarization effects or bubble formation is noted at the electrodes and the composition of the fluid remains constant.

(4) The solution has bright blue colouring and hence facilitates the reading of the meniscus position in the inclined manometers.

4.1.1 Experimental Set-Up

The experimental rig is shown in Figures 14 and 15. The settling chamber, test section and downstream and efflux sections were fabricated out of plexiglass since it is transparent, easily assembled, glued and sealed, is readily machined and bent into the required shape by application of heat. The test section was placed right behind the converging inlet section to make the entrance velocity profile as uniform as possible. Copper screens were placed in the settling chamber to even out the velocity distribution and eliminate vortices generated by the water pump. Beyond a certain current density, the metallic copper deposited on the electrode did not adhere to it firmly but was swept back into the stream; moreover, iron particles originating in the cast iron pump also contaminated the working fluid. These solids were filtered out partly by fibreglass batts inserted between the copper screens, to prevent clogging of the small pressure ports or deposition on the manometer walls. The fluid was circulated by a centrifugal pump driven by a variable speed D.C. motor. Additional copper screens were used at the outlet of the downstream section to further reduce and adjust the fluid velocity. A total of 28 pressure ports were drilled into the curved walls of the bend. These were connected by tygon tubing to glass tubes pressed firmly against a thick flat-ground plate forming a bank of inclined manometers, the slope of which could be adjusted. The magnetic field was generated by a coil of approximately 270 turns of formel coated magnet wire wound around the bend section. The current was supplied by a D.C. motor-generator set capable of delivering 300 amps. At a current of 120 amps. the average field inside the coil was found to be about 2000 Gauss. The current through the electrolyte was supplied by car batteries giving 24 volts. This current can be adjusted by varying the supply voltage or changing the concentration of the electrolyte. Because of the above-mentioned difficulty experienced with metallic copper in the fluid, deposited by excessive current density, the current was limited to 30 amps (about 2.7 amp/in.^{2}). To reduce the temperature rise of the field coils owing to this current, jets of compressed air were directed upon it to increase convection cooling. Even then the current had to be turned off after 40 seconds at 120 amps. and after 2 minutes at 80 amps. to avoid overheating the wire and damaging the insulation.

4.1.2 Results and Discussion

Due to limitations on magnetic field and applied current discussed above, the electromagnetic force acting on the electrolyte flow was quite small. With a field strength of 0.2 Weber/Meter^2 and an applied current of 2.7 amp/in.^{2}, the electromagnetic force is equivalent to a pressure of 0.08 inches of water or 0.072 inches of electrolyte. In order to render the electro-magnetic effect measurable, the manometer bank had to be inclined at a very small angle. The smallest slope used in the experiments was about 1 in 40. The dynamic head (and therefore the flow velocity) was also adjusted to comparable values. At such small inclination angles, surface tension plays a large part and even though the glass tubes and the whole assembly were cleaned frequently, they were quickly contaminated by the residual metallic suspension escaping filtration. A small admixture of Photo-Flo solution was found very effective in reducing the surface tension effects. Commercial grade glass tubing was used, and although the uniformity was not assured, neither in diameter or straightness, calibration showed that only a few tubes had deviations in meniscus level of 0.2 inch at the smallest inclinations.

Figure 16 shows the pressure profiles along the bend for test runs in water at various elevated speeds. The agreement with theoretical results seems to be within experimental error except for the static pressure drop due to frictional and other losses. Upstream of the inlet into the test section the static pressure at the inner and outer walls is not equal, indicating a slight velocity gradient across the inlet section. This section, made three-dimensional for maximum contraction ratio, is difficult to fabricate due to warping and contraction of the plexiglass upon cooling. Consequently, the apparatus can only be levelled approximately each time it is set up after cleaning (especially after the magnet coil was wound around the test section), giving rise to slight deviations in the pressure measurements. Figure 17 shows some runs with the electrolyte. The procedure adopted with each run was to adjust the pressure head by setting the pump speed, wait until the pressure readings are steady, take a polaroid photograph of the manometer bank, switch on electric and magnetic fields, wait for the manometers to stabilise and again take a photograph. It was previously established that the electrolytic current alone did not alter the pressure readings, hence the observed change during a run must be attributed to MHD effects. As stated before, heating of the magnet coil and accumulation of solids in the electrolyte put a limit on the time allowed for each run. With a coil current of 120 amps the running time was only 40 seconds, yielding pressure readings of only 30 percent of the expected value. Closer observatior revealed that the manometer level did not quite reach the equilibrium height within that time. Depressing the manometer level below the expected values and letting it rise under the action of the MHD forces showed that in 40 seconds the levels attained 40 percent of equilibrium height. The subsequent runs were therefore carried out with magnetic coil currents of 60 and 80 amps and a running time of 2.5 minutes. For most runs the manometer levels seem to reach equilibrium within that time. As seen in Figure 17, there is quite a scatter of readings among the non-magnetic runs. This is most likely due to the fact that each time the apparatus is dismantled and cleaned, it is difficult to reassemble it again in exactly the same position and a slight misalignment or lack of level of the test section produces deviations. To counteract these effects, it seems more appropriate to demonstrate the MHD effects by comparing the pressure readings of individual runs with and without magnetic field. Figures 18-21 show some typical pressure plots obtained in this manner, indicating the flattening of the profiles due to MHD forces. Unfortunately, for the MHD force to be comparable with the dynamic head, the flow velocity had to be so low that separation occurred and the manometer readings became scattered, indicating some deviation from laminar flow around the bend. It therefore seems impossible to run at conditions where the MHD force would significantly flatten the pressure profiles, a case where one could expect to observe some change in pressure loss in the bend flow. Ignoring the discrepancy in pressure profile due to losses and other effects (such as shape and position of the apparatus) it can be seen in Figures 18-21 that the change in pressure due to the MHD force is slightly less but quite close to the calculated change. Figure 18, a run with magnetic interaction parameter of 0.3 and a magnetising current of 120 amps, shows a comparatively small MHD effect owing to the fact that the manometer levels had insufficient time to come to equilibrium.

4.2 Experimental Verification Using a Plasma Arc Jet

4.2.1 Experimental Set-Up

Most of the experimental MHD work using compressible fluids was carried out either in shock tubes or in plasma arc jets. Both are capable of attaining flow of high-temperature plasma at various densities and both can be used in conjunction with an external supply of seeding material to produce high electrical conductivity. The first is relatively simple, but the flow so produced is of very short duration. This could be somewhat lengthened by expanding the flow behind the reflected shock through a suitable nozzle (shock tunnel), but the useful flow duration is still relatively short, requiring the measuring devices to possess low response times. In the latter method, however, the flow can be maintained for times of the order of several seconds, thus allowing the use of simple liquid manometers to measure pressure.

The device used in the present investigation was a plasma arc jet (E.H. Dudgeon and I.R.G. Lowe)[26] capable of maximum power input of 70 kW which could be operated for over 10 seconds continuously without damage. An estimate of the power required to produce plasma with high enough velocity and electrical conductivity to yield an interaction parameter $S \sim 1$, shows that the jet would have to be operated at a working pressure of about 1/10 - 1/20 of an atmosphere. A schematic of the experimental set-up is shown in Figure 22. The settling chamber was incorporated to provide adequate mixing of gas and seed material and to produce a fairly uniform velocity profile at the outlet. This was dimensioned in consideration of the work of Lipstein[27] who found that the potential core of the primary jet extended to less than $x/(D_2-D_1) = 3.33$ at $D_1/D_2 = 0.4$ (see Fig. 22). Since we have $D_1 = 1.5"$, $D_2 = 3.75"$, therefore $D_1/D_2 = 0.4$, hence the jet should extend to about $3.33 \times 2.25 = 7.5"$. The mixing chamber was therefore designed to be about 9" long, together with a profile approximately in the shape as calculated by Batchelor and Shaw[28]. The cross-section of the uniform plasma flow was limited to the dimensions 1.5" x 1.4", in view of the limited mass flow available. A glass section 4" long was attached immediately behind the mixing chamber to check the flow uniformity and to measure temperature and velocity profile. This section was removed before measurements on the bend were taken. A 2" long section made of machinable ceramic was used on either end of the bend to insulate the electrode-carrying walls of the bend electrically. The flow was then allowed to expand into a water-cooled heat exchanger, where the plasma temperature was reduced and the potassium seed condensed before reaching the vacuum pump. Because of the high volume flow rate required, high-capacity Fuller vacuum pumps (VC-300, No. 3223-3226, 600 RPM, displacement 1720 CFM) were used to lower the test section pressure to about 1.5" Hg. Runs with higher pressures were achieved by opening to atmosphere a valve located somewhere between the pumps and the heat exchanger.

4.2.2 The Plasma Arc Jet

The plasma arc jet used in the present experiment was designed a few years ago by Dudgeon[26]. Its detailed design and operating range will form the subject of a forthcoming report, hence only a brief description will be given here. A schematic diagram is shown in Figure 23. Argon from a storage bottle is fed through a swirl ring into chamber A. The vortex action carries the gas along the wall to the end of the chamber and out again near the axis. This design enables the gas to maintain contact with the arc for a considerable distance, thereby increasing the thermal energy imparted to the gas. The electric arc strikes from the anode in chamber A to the walls of channel B which act as cathode, and is imparted a swirl by an applied axial magnetic field. The heated argon is then ejected into the mixing chamber through channel B. Seeding is accomplished in a small section ahead of the mixing chamber. All parts of the arc jet except the tungsten cathode were made of copper and water cooled. The voltage drop across the arc was about 100 V and the current of the order of 500 amperes during a normal run in argon. Because of the voltage-current characteristic of the arc, the 70 kW power capacity of the supply could not be applied in its entirety, but a sufficient proportion of this went to heat the argon with the present arrangement.

4.2.3 The Seeder

In order to attain a reasonably high electrical conductivity, a pure argon jet would have to be heated to about 8000°K. This imposes a serious material problem, together with excessive boundary layer losses, and a necessary reduction in mass flow because of power limitations. The usual way of overcoming this problem is to seed the gas with alkali metal (Na, K, or Cs) (Lau[29], Dudgeon[30], Rosa[31]). At about 3000-4000°K, which is about the temperature used in the present work, practically all the argon atoms remain non-ionized, but any alkaline seed added, because of its low ionizational potentials, becomes highly ionized. Depending on the amount of seed added, the electrons thus produced act as current carries and greatly enhance the electrical conductivity. Quite a few forms of seed addition have been tried, i.e. feeding as a powder, smoke, liquid or vapour at different parts of the jet. Due to either non-uniformity, insufficiency, clogging of apparatus, or corrosion and material problems, these have not been too successful. The arrangement finally adopted is shown schematically in Figure 24. Preheated argon is fed through the top of the stainless steel seeder, forcing the molten potassium up the inner section and then bubbling through it. This carries some potassium, both in the form of vapour and minute droplets, into the main plasma jet through the middle top valve. This valve, together with the seeder is enclosed in an oven and heated normally to about 1000°F. The seeded argon enters the jet through an opening in a stainless steel section ahead of the settling chamber.

An attempt was made to observe and measure the seed flow rate in the seeded argon flow by passing the out-flow from the seeder into a stainless steel cylinder fitted with a sintered stainless steel filter, and a thick glass plate on top. Even though the seeder seemed to work fairly well at atmospheric pressure, it did not function as expected at reduced pressures. The idea underlying this seeding arrangement is that as the pre-heated argon is bubbled through the molten potassium, it will be saturated with potassium vapour at the partial pressure governed by the temperature of the liquid potassium. Unfortunately, when the temperature was adjusted to near the boiling point of potassium at the design pressure, liquid potassium was forced out of the seeder. On the other hand, when the temperature was somewhat below the boiling point, smoke was generated and on measuring the amount of potassium that was filtered out, the percentage seed was usually about 0.01 percent. Attempts to pass current through the argon plasma jet seeded with this seeder outflow proved to be unsuccessful. The reason for this is that even though the mass flow of argon through the seeder is small (about 2 percent of the total argon jet flow), the volume flow was large because of the high temperature and low pressure. The velocity through the molten potassium is therefore quite high and the argon does not have sufficient time to become saturated with potassium vapour. On the other hand, when the temperature is at the boiling point the fast-flowing argon picks up drops of liquid potassium that is bubbling on the surface of the molten metal and carries it through the constrictions in the valves and tubings out of the seeder. However, attempts to pass current through the argon plasma with the seeder operated in this mode seems to be quite satisfactory. Currents up to 10 amperes were passed quite successfully through the plasma from electrodes about 1.4" square, so that in all the subsequent runs requiring seeding, the seeder temperature was adjusted to the boiling point of potassium at the design pressure (1/10 atmosphere). The seeder section, the settling chamber and the test section have periodically to be cleaned out due to accumulation of potassium.

4.2.4 The Bend Section

Fabrication of the bend section proved difficult. Tests with a dummy bend section showed that its temperature rose to about 600^{o}F after a few seconds of running, hence all materials used have to be able to withstand at least that temperature. The two plane side walls act as electrodes, and because of the corrosive nature of the seed, stainless steel was used. the curved walls, however, have to be insulators, and in order to observe any flow irregularities inside the bend, pyrex was the obvious choice. These walls were made by bending two rectangular slabs of pyrex on a form in an oven. At a certain temperature, the pyrex softens and conforms to the shape of the form. These were then ground, drilled for pressure taps, and glued onto the stainless steel side walls with high temperature glue (RTV) which also acts as a vacuum seal (Fig. 12). Since the electrodes have to be insulated from the rest of the apparatus, the bend section was attached at both ends to straight sections, 2 inches long, and machined from solid blocks of Aremcolox machinable ceramics (Grade 502-1100). Vacuum sealing was accomplished by rubber "O" rings.

4.2.5 The Magnet Coil

In order to obtain an appreciable interaction, a magnetic field of about 5000 Gauss had to be generated. With a motor generator set available, capable of producing 250 amperes, the density of windings required is about 300 turns per foot. To allow space for inserting the pressure probes and electrical leads, and to enable the test section to be slipped out of the magnet coils in order to replace or clean the electrodes, the coils were wound with larger internal dimensions of 2" x 2.5". A gauge, No. 24 formel coated rectangular section magnet wire was used and the coil was wound in four sections with spaces between for pressure probes, each secting having 12 layers. The magnetic field inside the bend was measured with a Hall effect device and with 200 amperes through the coil, the average field inside the coil was 5500 Gauss in the middle of the coils, dropping to 4700 Gauss between the coils and to 2700 Gauss right at the ends of the coil. The resistance of the coil increases noticeably due to ohmic heating, so that the voltage had to be constantly adjusted to give a steady current. The time of current passage was limited to about 10 seconds to avoid overheating and thus damaging the formel coating on the magnet wire.

4.2.6 Instrumentation

4.2.6.1 Pressure

To prolong the life of the components of the plasma jet, each run was limited to a maximum duration of 20 seconds. Since the flow takes a while to steady down, the actual time available for measurement was only about 7 seconds. Trial runs with inclined differential water manometers showed that the liquid column still oscialated about its equilibrium level at the end of 5 seconds. Moreover, taking the pressure from 16 pressure ports along the channel during that short time requires a bank of manometers properly mounted and a camera to take a picture. This proved quite cumbersome, therefore a method commonly used in recording pressure profiles on models in wind tunnel testing was employed here. This consists of a pressure transducer mounted in a "scanivalve" which is driven by an approximately square wave voltage pulse with a variable frequency. This drives a rotor in the scanivalve, connecting the different pressure ports to the transducer. The time that the rotor takes to go from one port to the other and the time it stays on a particular port is adjustable by varying the frequency and length of the voltage pulse. The most sensitive pressure transducer available was used since the pressure differences encountered in the bend ($p_{OUT}-p_{IN}$) was less than 4" H_2O. This was a Statham transducer model PM131TC ± 2.5 - 350 (Serial No. 33093), which has a pressure range $\pm$ 2.5 psid., with a nominal calibration factor of 1729 microvolts/volt/psi. A type J scanivalve was used which on test runs showed that it had a fast enough response to record 20 pressure signals within the 5 seconds time. The transducer was calibrated by pumping down two chambers to about 3" Hg. and adjusting to give a pressure difference of about 5" H_2O, measured with an inclined manometer. One port of the transducer was then connected into one chamber, and the backing pressure into the other, and the voltage output was recorded either on a Brush chart recorder or on an oscilloscope, when the rotor is scanned through the 48 ports. On the oscilloscope, the single square pulse shows up quite well, but on the recorder, which is the fastest on the market, the pen does not follow the step too well. As shown in Figure 25, where two consecutive ports are connected, the pressure trace shows a portion of flat top when time between ports is adjusted to 400 msec. When the interval is adjusted to 200 msec., however, the pen barely reaches the top, which is just about the lower time limit tolerable. The calibration factor during these runs was found to be 1643 microvolts/volt/psi.

Another difficulty in using this scanning system was connected with the fact that the current passing through the plasma was not quite steady, and the pressure was affected by ohmic heating of the gas. The pressures recorded were therefore pressures along the bend at different times. This therefore introduces another source of error, dependent on the steadiness of the current both spatially and temporally.

4.2.6.2 Velocity

Because of the high temperature of the gas flow, the usual methods of inserting a pitot probe into the gas stream was not feasible. Moreover, the plasma flows through a contracting section, and the velocity profile may not be as flat as desired. To measure the velocity profile, one of the best ways is to use the method of successive sparks, which has been used quite successfully in hypersonic tunnels (Ref. 32, 33) and shock tubes (Lau and Mills[34]). The principle used is based on the fact that an electric arc will follow preferentially a path with the least resistance. In this method, a fast discharge from a condenser strikes an arc across the plasma flow, from two electrodes inserted on the wall (Fig. 2). This ionizes a thin column of gas, producing a bright streak across the plasma. The column of ionized gas is then swept downstream with the same velocity as the plasma flow. At an adjustable delay time, another high voltage pulse is applied across the strip electrodes. If this delay time is adjusted so that the previously ionized gas column is passing the strip electrodes, a new arc will jump across, following the shape of this column. This delay time, however, has to be less than about 100 μsec. to avoid excessive recombination of the ionized gas in the column.

The signals from two pick-ups on the discharge circuit are recorded on the oscilloscope, from which the time between discharges is obtained (Fig. 27). An open shutter photograph shows two bright columns some distance apart (Fig. 26). From this distance and the time between discharges, the velocity profile across the channel and gas flow velocity can be calculated. With relatively cold gases (Ref. 32, 33) or hot gases at atmospheric pressures or above, fairly clear pictures can be obtained (Fig. 26a). In the present experiment, however, the power across the main arc, the mass flow, the pressure, and the velocity were chosen such that the temperature is around $3500^{\circ}K$, the pressure is 1/10 - 1/20 atmosphere and the Mach number below 0.3. At these conditions the difficulty arises that in the extreme case of high temperature and low pressure all the discharge energy is used up in forming a corona discharge at the electrode tips (Fig. 26b), so that no arc is formed. Varying the voltage, the energy, the discharge time and using carbon electrodes and auxiliary spark gaps does not improve the situation. At less extreme conditions, the corona discharge still forms, but an arc forms as well, so that an approximate velocity profile can still be obtained. The final arrangement of the electrodes (Fig. 27) seemed to improve the picture somewhat, since the gas around the electrode tip was not as hot and any bright region due to corono discharge did not mar the picture. To avoid sharp corners where the discharge may start, a bent round wire was used instead of strip electrodes. It was found that when the delay time was adjusted by trial and error such that the previously ionized gas column was around the middle of the strip when the second discharge formed, a good second bright column is formed which conformed approximately to the shape of the first discharge.

The arcs formed at a typical running condition are shown in Figure 26a. The velocity there is approximately 1000 fps, and from the mass flow rate measured with a flowrator, the density was calculated to be about 0.765×10^{-3} lb/cu.ft. The measured pressure was about 3" Hg, giving a temperature of approximately 4000°K. This. however, is only an average temperature, since wall effects and heat conduction are certain to cause a fairly uneven temperature profile (Kyoichi Kuriki[35]). The true temperature profile is measured by spectroscopic means discussed in the next section.

Because of the difficulty in establishing a uniform current across the bend in a high speed stream, it was decided to reduce the velocity somewhat. In the final series of runs, the mass flow was reduced by about 50 percent by changing the argon swirl inlet ring and adjusting the pressure and mass flow. After the whole series of runs, the spark tracing apparatus was set up again to check the velocity. Clean arcs, as seen previously, could not be established, but the two arc columns can still be seen (Fig. 26d). The velocity was then calculated to be 592 fps. for the final series of runs.

4.2.6.3 Temperature

Normally, the average temperature of the plasma produced by an arc jet can be determined by measuring the electrical energy supplied to the arc jet and the heat loss to the cooling water. At lower temperatures, radiation losses are small, so that this 'heat balance' method will give fairly accurate results. In the present arrangement, however, a significant amount of heat is lost in the settling chamber even though it is not water cooled to avoid excessive heat loss and seed condensation. The temperature obtained by the heat balance method is therefore lower than that obtained by inferring from velocity and pressure measurement. In order to confirm that the temperature obtained is approximately correct and to gain some idea of the temperature distribution across the channel, a spectroscope was used to measure the plasma temperature. The temperature measurements in the plasma jet and different spectroscopic techniques will be described in detail in a forthcoming report and so will not be discussed here. Suffice it here to say that both the relative line intensity method and the line reversal method with a Xenon arc lamp were used and the results obtained for an open jet were in fair agreement with the result from heat balance method.

4.2.6.4 External Current Source and Electrode Performance

Since the possibility of MHD power generation came to light a few years ago, many investigations have been carried out on the phenomenon of current conduction between electrodes immersed in plasma flow (Ref. 31, 36-41). The voltage drop in the main inviscid stream is found to be relatively small because of the high electronic conductivity. For example, in the present experiment, with conductivity σ = 300 mho/meter and a current of 5 amperes/sq.in., the voltage drop across the channel width is only about 1/3 volt. Most of the voltage drop occurs at the electrodes, due either to the cold and hence less conducting boundary layer, or to insufficient electron emission from the cathode. Various mechanisms of electron emission are described by Cobine[42] and a detailed description on conduction across cold electrodes is given in Chung and Blankenship[39] and Hoppman[40], where all electron emission is neglected. The latter experiment was carried out in a shock tube, hence the electrodes were essentially cold, and only ionic conduction was present. However, a uniform current of 0.4 amps/cm^2 was obtained with a voltage of about 28 volts across the electrodes.

On a clean electrode at temperature T under an electric field E, the emission is given by Hayden[43],

$$J = 1.2 \times 10^6 T^2 \exp(-\emptyset/kT)\exp(0.438\sqrt{E}/T)$$

where $\emptyset$ is the work function of the electrode material. At around room temperatures, this emission current is extremely small, since most electrode materials have a work function of about 4.5 eV. However, when the electrode surface is coated with an oxide layer or impregnated with foreign particles, various effects come into play and the electron emission can increase by orders of magnitude. This is summarized by Hayden[43].

In a practical MHD device, the plasma flow is steady and the electrodes are heated to some degree. Rose[31] found that quite significant currents can be drawn across a seeded plasma jet. Zukoski and Pinchak[36], Bekiarian[37], Maslennikov and Germanyuk[38], Toshitsuya and Uchica[41], have experimentally investigated hot contaminated electrodes in a plasma stream and found that the current is strongly dependent on the temperature of the electrodes. However, the geometry, material, temperatue and other parameters vary in these experiments and there is no absolute way of calculating the electrode performance in a particular arrangement. In order to pass a uniform current through the plasma, one must therefore resort to trying various schemes bearing these results in mind.

To begin with, top and bottom walls of the straight 4" long glass section were machined out to fit two stainless steel electrodes about 1.25 x 1.4 inches. These were flush with the walls to avoid boundary layer build up, and were connected in series with a 10 ohm resistor to a variable voltage source, This voltage was varied between runs and the current flowing through and voltage across the electrodes were recorded. With this set-up up to 10 amperes and 50 volts across the electrodes were recorded when the electrodes were coated sufficiently with seed. However, when the test section was inserted, it was impossible to pass any current between the stainless steel side walls which acted as electrodes. This was due to the fact that these massive walls were not sufficiently heated during each run. To correct the situation, a sheet of tungsten, 0.005 inch thick, insulated thermally from the steel side walls by a thin mica sheet, was attached to the walls with small rivets. Trials to pass current with this scheme show that arcs form at the upstream end of the tungsten sheet, get swept downstream by the flowing plasma and stay at the downstream end. Near the end of each run, only about 2 or 3 inches of the downstream end of the tungsten sheet was passing current. This can be observed quite clearly through the curved side walls. However, since the maximum pressure difference between inside and outside curved walls occurs at the centre of the bend, it was desirable that the bulk of the current should pass here, if it should not be possible to have a uniform current distribution across the whole bend. To achieve this, all the rivets holding the tungsten sheet were insulated electrically from the steel walls except the last pair downstream. The mica insulation separating the tungsten from the steel side walls does not run all the way to the downstream end, so that the tungsten sheet is attached to steel side wall at the downstream end to keep it relatively cool. Current is fed in from the upstream end to counteract any tendency for the conducting column to be swept downstream. With this scheme, a few good runs were obtained with quite uniform current in the middle of the bend, up to 78 amperes. The pressure traces for these runs are shown in Figure 28, where it can be seen that the average pressure drops, beginning from about 30° of the bend due to ohmic heating of the plasma. However, these runs are difficult to repeat, especially when the magnetic field is turned on, and in most of the runs either insufficient current was passed or it was confined to a small region either upstream or downstream of the centre. A typical pressure trace for this is shown in Figure 29, where the current passed in a small region (about 1 inch diameter) near the upstream end of the tungsten sheet. A further attempt to force the current to pass consistently in a desired region was made by having small thoriated tungsten rods protruding through the steel walls, but the current was still not distributed uniformly. Some tungsten rods invariably take over and carry the bulk of the current. It was concluded when that the tungsten sheets heated by the plasma flow would make better electrodes, as long as they were not too large. To investigate this, a tungsten sheet, 1-1/2 inches long, was placed near the centre of the bend. Each time, a fairly uniform current was passed between these tungsten electrodes as long as no magnetic field was applied. Unfortunately, when the field was turned on, the current seemed to be either extinguished or forced to flow a little ahead of the tungsten electrode. A typical pressure trace with this electrode arrangement is shown in Figure 30, where it can be seen that without the magnetic field the average pressure begins to drop at about the upstream edge of the tungsten electrode, whereas with the field on, the decrease in pressure difference occurs a little ahead. During these runs the tungsten electrode was not electrically insulated from the steel side walls, so that the current might have attached onto the wall, and with the field coils around the bend, it was difficult to see precisely where the current was flowing. The final electrode arrangement is shown in Figure 31. All three sets of tungsten electrodes are electrically insulated from the steel walls, and are connected to the power supply through resistors of about 0.5 ohms each. The total current and the voltage across each pair of electrodes are recorded, and with no magneitic field present, these records show the currents flow quite uniformly through the three sets of electrodes. When the field is turned on, however, the individual currents through these electrodes are different and not quite constant, and sometimes the current is actually extinguished when the field is turned on rapidly. This is probably due to the $\bar{J} \times \bar{B}$ force acting on the tiny arc spots on the electrodes and driving them towards the inside curved wall. More could probably be done to improve this electrode conduction mechanism, for example, by heating these tungsten electrodes by external electrical means, or by segmenting them into even more separate smaller electrodes. However, since runs with magnetic field on do show roughly the desired result, and since the test section was being slowly chipped and cracked, it was felt that much further work in this respect would not drastically change the final result.

4.3 Experimental Results and Discussion

The primary purpose of the present experiment is to investigate the change of pressure profile in the plasma flow around a bend produced by a magnetohydrodynamic force. Unlike the hydraulic analog using electrolytes, other side effects tend to complicate the matter. First, in order to be able to pass sufficient current through the plasma, seeding is necessary, and this proved to be rather difficult at low pressures. In order to have sufficient seed, liquid potassium is sometimes forced out of the seeder, and this coats the walls of the test section, making them rather rough. Ocassionally some pressure ports are plugged up by this deposit during a run. Secondly, passing current between electrodes is just as difficult, especially when a crossed magnetic field is present. In the final electrode arrangement, as discussed in the previous section, the three tungsten electrode pairs did pass current quite evenly from about 15^o to 75^o of the bend, when no magnetic field was present. When the field is turned on, however, the current is not as evenly distributed between the three electrodes. Moreover, when the tungsten electrode sheets are heated, they expand and bulge out. This, in addition to the slight constriction due to mounting of the tungsten and mica sheet on the side walls, cause some variation in the pressure readings. Finally, as distinct from the electrolyte flow, the plasma is heated quite significantly by the current passing through it. As seen in Figures 32-34, where current is passing, the average pressure drops. The mechanism of heating and the amount of heat added by the current is difficult to formulate, because most of the voltage drops occur at the relatively cool electrode surfaces where energy is dissipated in the form of tiny arcs. This heated layer of gas at the side wall is eventually swept into the main stream either by turbulence or the secondary flow that is present. A rough estimate on the change in pressure, velocity, etc. can be made by assuming one-dimensional flow and that the amount of ohmic heating is given by J^2R where R is the calculated resistance of the main stream plasma. Taking, as an example, a case (Fig. 32) where the current seemed to pass quite uniformly across the three electrodes, we have approximately, at entrance into the bend:

Velocity, V = 592 fps.

Pressure, p = 1/10 atmosphere

Mass flow, $m = \rho VA$ = 0.734×10^{-2} lb/sec.

= 0.44 lb./min.

Density, $\rho = \frac{m}{VA}$ = 2.82×10^{-5} slugs/ft.^{3}

Temperature, $T = \frac{p}{\rho R} \doteq 3350^{\circ}$K

Sound Speed = $\sqrt{\gamma RT}$ = 3460 fps.

Mach No., $M = \frac{592}{3460}$ = 0.17

The theoretical conductivity at this temperature with 0.1 percent seeding is about 3 mho/cm (Dudgeon[30]). However, due to heat loss along the channel, the conductivity drops and, according to Rosa's estimate[31], the conductivity in the channel was probably about 1.5 mho/cm. In the above reference, a similar arc jet was used and plasma temperature was about 3000°K, so it can be roughly assumed that the electrical conductivity in the present experiment was also about 1.5 mho/cm.

Resistance of current path $= \frac{\ell}{\sigma A} \doteqdot 0.062$ ohms

Ohm heat dissipated to main stream $d\varphi \doteqdot I^2R \doteqdot 92^2 \times 0.062 = 524$ joules/sec.

$\doteqdot 170$ joules/gm.

Assuming one-dimensional flow and that $M^2-1 \doteqdot -1$, and that changes are small,

$$\frac{dV}{V} = \frac{\gamma-1}{\gamma}\,\frac{1}{1-M^2}\,\frac{d\varphi}{RT} \doteqdot \frac{\gamma-1}{\gamma}\,\frac{d\varphi}{RT}$$

$$\frac{dT}{T} = (1-\gamma M^2)\,\frac{dV}{V} \doteqdot \frac{dV}{V}$$

Integration gives

$$\frac{V_{exit}}{V_{entrance}} = \frac{T_{exit}}{T_{entrance}} \doteqdot 1.37$$

$$\therefore \quad \frac{M_{exit}}{M_{entrance}} = \frac{V_{exit}}{V_{entrance}}\sqrt{\frac{T_{entrance}}{T_{exit}}} = 1.17$$

$\therefore$ Average Mach No. along bend $\doteqdot 0.17 \times \frac{2.17}{2} = 0.182$

$$\frac{dp}{p} = \frac{(\gamma-1)M^2_{aver}}{M^2_{aver}-1}\,\frac{d\varphi}{RT} = 0.00582$$

$$\Delta p = 0.00582 \times 40.5'' \; H_2O \doteqdot 0.23'' \; H_2O$$

The drop in pressure at the exit from the bend in this case (Fig. 32) is about 0.22" H_2O; so that this rough calculation does show that for a uniform current distribution across the channel, the pressure drop can be accounted for by the ohmic heating of the plasma core. The voltage drop across the plasma core is 92A x 0.062Ω = 5.7 volts, whereas the total voltage drop across the electrodes is about 18 volts, so that most of the voltage drop and ohmic dissipation occurs at the relatively cool boundary layer. In most other runs, the total current is smaller, but the voltage drop across electrodes is higher, especially in runs with magnetic field present, showing that the boundary layers and hence electrodes are relatively cooler. Small, unsteady arc spots occasionally appear on both cathodes and anodes. This shows that the electrode voltage drop is due mainly to the cool boundary layer and not due to insufficient cathode emission. Whereas the above calculation accounts roughly for the pressure drop due to ohmic heating of the main plasma stream, most other runs with a smaller current (Fig. 32-34) show a higher pressure drop. In these cases, the assumptions made in the above calculation must be invalid. There are a few plausible explanations for the higher pressure drop. First, the current conduction across the electrodes may not be uniform, resulting in a higher resistance and higher ohmic heating. Secondly, even though the current is smaller, the voltage drop at the electrodes is high, and some of the heated gas near the electrode may be convected into the main stream by the secondary flow that is present in the bend. Finally, due to the ohmic heating, the boundary layer thickens, effectively reducing the cross-sectional area of the channel. This change in area also tends to decrease the pressure in the main stream. To investigate these possibilities, one method is to insert electrostatic probes into the plasma and to study the potential distribution. However, because of the unrepeatability of the runs and the limited accessible space, and to avoid weakening the glass test section, this investigation was not carried out. Instead, we shall ignore the change in average pressure along the bend, and study the effectiveness of the J x B force in suppressing the pressure difference between the inner and outer curved walls. To isolate this heating effect, it was assumed that the current was evenly distributed radially; so that while the average pressure drops appreciably, the pressure difference between inner and outer wall is not significantly affected, and this quantity is plotted alongside the pressure curves to show the effect of the MHD force.

Before discussing the experimental results obtained, a few comments on the possible sources of error are necessary. First, because of the difficulty of machining glass, the test section is tied onto the insulating ceramic section rather loosely, unavoidably creating slight steps each time the apparatus is assembled. This, together with the potassium coating and the protruding electrodes which expand and buckle under heat, makes the channel walls a rather uneven surface. The Reynolds number for the latter series of runs is about 700

$$(Re = \frac{\rho VL}{\mu} = 1.43 \times 10^{-2}\ \frac{\text{kgm}}{\text{m}^3} \times 183\ \frac{\text{m}}{\text{sec}} \times \frac{1.4}{39.37}\ \text{m} \times \frac{\text{m-sec.}}{1.21 \times 10^{-4}\ \text{kgm}}$$

$$= 770)$$

so that a thick laminar boundary layer is expected. All these effects cause some unpredictable errors in the flow variables inside the bend. Because of this, during each series of runs when the test section is re-assembled, the pressure records show some deviation, even for runs without field or current. Secondly, the electrical energy transferred to the argon in the arc source depends on the length of the arc and the voltage across it. The voltage and current across the arc vary slightly for every run. This, coupled with the fact that the mass flow and pressure, even though preset, change slightly when the jet is turned on, makes it difficult to maintain the same dynamic head for all the runs. It is, unfortunately, not feasible to measure the velocity for each run, so that for the final series the velocity was only measured once and we assumed that it (592 fps.) did not vary appreciably from run to run. Thirdly, as seen in the current records for the run with magnetic field on, the current decreases quite significantly when the field is turned on. As a matter of fact, in most of the runs, when the electric field is applied, the current jumps sharply to over a hundred amperes, but drops immediately to zero when the magnetic field is turned on very rapidly. In order to maintain some steady current, it was found necessary to increase the magnetic field slowly. Even so, the current always decreases when the magnetic field is on.

This could not have been due to Hall effect because the Hall current is inhibited by geometry of the test section, so that the transverse conductivity should not be reduced by Hall effect.

The most probable reason is that tiny arc spots form at the electrodes, and these arcs are driven by the J x B forces towards the inner wall. The current distribution is therefore not uniform and concentrates more on the inner curved wall. Finally, the accuracy of the experiment is limited greatly by the time factor. To avoid overheating and thus damaging the apparatus, the time for each run is not allowed to exceed about 20 seconds. Because of the time delay in slowly attaining a desired magnetic field and the time required for the current to steady down, the actual time available for scanning all the pressure ports is limited to about 7 seconds. Because of the ohmic heating of the electrodes and gas flow, the flow properties may not be able to reach a steady state during this small testing time. Moreover, because it is necessary to use a scanning system, the pressures on the outer curved wall are taken at different times from those on the inner curved wall, so that any transient or unsteadiness could introduce large errors. Also spurious signals sometimes appear because of the scanning action of the scanivalve.

Figures 32-34 are the experimental results of the final series of runs which show the effect of the MHD force, with each figure showing the runs between which the apparatus is disassembled and cleaned.

In all these runs the static pressure (p) ahead of the bend is assumed to be 3" Hg, the velocity (V) is assumed to be 592 fps. Inside the bend, as discussed previously, the magnetic field is not quite homogeneous, and the current magnitude and distribution are both unrepeatable and non-uniform. Because of the difficulty in formulating and computing a solution allowing for this inhomogeneity, and the amount of experimental error involved, it was not worth the effort to initiate a new computer program. In order to compare with the present theory, the magnetic field and current are assumed to be uniformly distributed across the entire bend section, so that $B \doteqdot 0.4$ webers/m^2 (with a current of 180A through the coils) and J = recorded total current/area of side walls of the bend. The interaction parameter indicated in these figures is therefore calculated according to $S = \frac{JBR_o}{\rho V^2}$.

Figure 29 shows a typical run where a single tungsten electrode extends along the entire channel side wall as discussed in section 4.2.6.4. The current was confined in this case to a small area near the entrance into the bend. This is evidenced by visual observation and by examining the tungsten electrodes after the run. Near the region of current flow, a dip in the pressure difference is shown in Figure 29. This region is close to the edge of the magnet coil, so that the magnetic field is quite small. Accordingly, for the magnitude of current flowing, the dip in the pressure difference is much smaller than expected. Figure 30 shows the pressure record where the tungsten electrode is about 1-3/4 inches long, located near the middle of the bend. A larger suppression of the pressure difference occurs ahead of the electrode position. It appears that the current is pushed by the fringe magnetic field towards the edge of the field coil. From these earlier runs it seems that the amount of suppression of pressure difference is smaller than anticipated and that it is difficult to locate the current at a desired region with a single electrode. Therefore, for the next series of runs, the three electrode system was used, and the setting on the motor generator set was increased somewhat to allow for larger currents. Figures 32-34 show some of the representative runs where there is distinct suppression of the pressure difference. The general characteristics for these runs are summarized below:

(1) The pressure records for the runs without field or current are slightly different, but have the same general shape.

(2) The pressure records with current only also have the same general shape. The average pressure drops quite steadily from where the current starts flowing, but the pressure difference between inner and outer wall is not affected.

(3) The average pressure for the runs with field and current also drops in the same fashion, but in general, the total drop in pressure is larger or equal to that of the cases without magnetic field, even when the current is generally smaller.

(4) The pressure difference between inner and outer wall is partially suppressed by the MHD force, but the amount of suppression is less than predicted by theoretical calculation assuming uniform field and current.

(5) The profiles of the pressure records for the runs with field and current differ in shape, showing that for each case, the distribution of current was non-uniform.

(6) The voltages across the three sets of electrodes are approximately equal for most of the runs except for run No. 2 S=.077 in

Figure 34, where the voltage at the first electrode is about half the voltage at the second electrode, showing that very little current is passing through the second one.

(7) The suppression is, in most cases, much more pronounced near the centre portion of the bend where current flows. Near the two ends beyond the region of the electrodes, the suppression is small or even zero.

Without much more detailed work and better electrode and magnetic field coil arrangement, it is difficult to identify the reason why the suppression of pressure difference is smaller than expected. One obvious reason is that the increased heating of the gas increases the kinetic energy, so that the effective interaction parameter ($\frac{JBR_o}{\rho V^2}$) is smaller than the theoretical value, resulting in a smaller suppression than the calculated amount. Another reason is the different amount of heat added to the gases near the inner and outer wall. This can be due to two reasons. First, as discussed previously, the magnetic field tends to force a concentration of current near the inner curved wall, so that there is a higher rate of heat addition. Second, the inner wall pressures are scanned at a later time than those of the outer wall, so that there is a longer time for conditions to reach the steady heated state. Because addition of heat reduces the static pressure, the pressure at the inner wall therefore drops relatively more than the pressure at the outer wall. This in effect widens the pressure difference, opposing the action of the MHD force. Consequently, the effect that is measured is probably just the resultant of these two opposing phenomena. This difficulty can undoubtedly be solved with more careful design of the test section, magnetic field coil and electrodes. For example, the test section could be designed to withstand a higher temperature and, consequently, a longer testing time. The pressure connections could be taken out of the ends of the coil so that the windings could be done uniformly. The coil should extend beyond entrance and exit of the bend to provide a uniform field region inside the bend. Finally, the electrodes could be properly insulated from and embedded into the side walls to provide a smooth surface. They could be made in smaller segments, separated electrically by resistors and capable of being heated by external electrical means previous to running the experiment. Probes could be inserted into the test section to study the potentials and electrical conductivities at various regions. With more effort in making these studies, it is conceivable that the process can be better understood and different sources of error isolated and eliminated individually.

5. CONCLUSION

The fluid flow in a 2-D right angle bend under crossed electric and magnetic fields has been investigated both theoretically and experimentally. On the theoretical side, three methods were used in computing the flow. The method of characteristics was used for the case of supersonic flow with a magnetic field aligned with the bend. Assuming no boundary layer and electrode sheath effects, it was found that the induced current ($J = \sigma(\overline{V} \times \overline{B})$) delays the formation of the standing shock formed inside the bend. With sufficient field strength, the shock is inhibited. The method of integral relations and the Rayleigh-Ritz method were used for incompressible and subsonic flows around the bend. The results from these two methods were compared with each other and with previous work wherever possible, and good agreement was found. The theoretical results for compressible flow under the influence of a magnetic field only show that the MHD effect is very small since the induced current is only to the first order. To obtain the desired effect, it was found necessary to drive a substantial current across the electrodes by means of a battery or some external current source. The theoretical results of incompressible flow around a 2-D right-angle bend under the influence of crossed electric and magnetic fields show that noticeable effects can be obtained with the available experimental apparatus.

Two separate experiments were performed to verify the theoretical results. In the first case, an electrolyte was used. This circumvents a great deal of difficulty in heat transfer, electrode effects and heating of plasma by the current. The main difficulty here is in measuring the pressure because the levels in the manometer used take a fairly long time to stabilize at the equilibrium level. The magnetic field that can be used is limited because the coils heat up excessively. Consequently, only a small interaction parameter can be achieved, but the results show that the effect of the cross field, even though slight, is clearly visible and the experimental results are in fair agreement with theory. The drop in average pressure along the bend is unavoidable because of frictional and other losses inherent in flow around bends.

In the second experiment, a plasma arc jet was used to produce the electrically conducting medium. The main difficulty in this experiment is the attainment of uniform current across the entire bend section. This affects the pressure measurements in two ways. First, because of non-uniform distribution, the effective electrical resistance of the current path is higher than in the uniform case. This, together with voltage drops at the electrodes, causes more ohmic dissipation than expected. As a result, the average pressure drops more rapidly than anticipated, as can be shown by analogy with pipe flow with heat addition. This pressure drop does not represent an additional loss because it is associated with increase in kinetic energy. Actually, in bends where separation is likely to occur, this transfer from pressure to kinetic energy is expected to help prevent separation. The increased heat addition, however, increased the kinetic energy of the flow (ρV^2), so that the effective interaction parameter ($\frac{JBR_o}{\rho V^2}$) is smaller, resulting in a smaller measured MHD effect. Secondly, this non-uniformity of current has an adverse effect on the pressure difference. However, with improved test section and electrode design, this difficulty could be overcome, and judging from the experiment with the electrolyte, the pressure difference between inner and outer walls in bend flow could be suppressed entirely or in part, depending on the electric and magnetic fields available. Because of the relative ease in shaping magnetic fields, one could, if necessary, change the pressure profile at different regions in the bend, thereby suppressing or altering the form or magnitude of the secondary flow. To study this process and its effect on the total loss in a bend would require quite elaborate experimental fabrication and is beyond the scope of the present work.

REFERENCES

1. Wetstone, David M., Ehrlich, Melvin P. and Finkelstein, David: Experiments on Plasmoid Motion Along Magnetic Fields. Phys. of Fluids, Vol. 3, No. 4, July 1960.

2. Schmidt, George: Plasma Motion Across Magnetic Fields. Phys. of Fluids, Vol. 3, No. 6, Nov. 1960.

3. Eubank, Harold P. and Wilkerson, Thomas D.: Plasma Motion in a Curved Magnetic Field. Phys. of Fluids, Vol. 4, No. 11, Nov. 1961.

4. Eubank, H. P. and Wilkerson, T.D.: Further Studies of Plasma Motion in a Curved Magnetic Field. Phys. of Fluids, Vol. 6, No. 7, July 1963.

5. Batanov, G. M. and Ivanovskii, M. A.: Particle Losses and Configuration of a Plasma Jet Moving in a Curvilinear Magnetic Field. Soviet Physics JETP, Vol. 19, No. 5, Nov. 1964.

6. Hains, F.D., Yoler, Y.A. and Ehlers, E.: Axially Symmetric Hydromagnetic Channel Flow. Dynamics of Conducting Gases, edited by A.B. Cambel and J.B. Fenn, N.W. University Press, 1960.

7. Courant, R. and Friedrichs, K.O.: Supersonic Flow and Shock Waves. Interscience Publishers Inc., New York, 1948.

8. Hawthorne, W. R.: Flow in Bent Pipes. Proc. of the Seminar on Aeronautical Sciences, Nov. 1961.

9. Eichenberger, H. P.: Shear Flow in Bends. Office of Naval Research T.N. No. 2, April 1952.

10. Higginbotham, J.T., Wood, C.C. and Valentine, E.F.: A Study of High Speed Performance Characreristics of 90° Bends in Circular Ducts. NACA TN 3696, June 1956.

11. Szczeniowski, Boleslaw: Design of Elbows in Potential Motion. J. of Aero Sciences, Jan. 1944.

12. Carrier, G.F.: Elbows for Accelerated Flow. J. of Applied Mechanics, June 1947.

13. Kamiyama, S.: Two-Dimensional Potential Theory on Flow Through Bend of Arbitrary Profile. Rept. Inst. High Speed Mech., Japan, Vol. 15, No. 147, 1963/64.

14. Kantorovich, L.V. and Krylov, V.I.: Approximate Methods of Higher Analysis. Interscience Publishers Inc., New York, 1958.

15. Chushkin, P. I.: Subsonic Gas Flow Around Ellipses and Ellipsoids. Vychislitel'naya Matematika, 2, 20, 1957.

16. Alikhashkin, Ya. I., Favorskii, A.P. and Chushkin, P.I.: On the Calculation of the Flow in a Plane Laval Nozzle. Computation Mathematics and Mathematical Physics, Vol. 3, No. 6, 1963.

17. Chushkin, P.I.: Hypersonic Flow Around a Circle and a Sphere in a Magnetic field. PMM, Vol. 27, No. 6, 1963.

18. Popov, F. D.: One Approach to the Method of Integral Relations in the Problem of Supersonic Flow Past Blunt Bodies. Soviet Physics--Technical Physics, Vol. 11, No. 2, 1966.

19. Holt, M.: The Design of Plane and Axisymmetric Nozzles by the Method of Integral Relations. Symposium Transonicum, ed. K. Oswatitsch. IUTAM Symposium, Aachen, 1962. (Springer-Verlag).

20. Dorodnitsyn, A. A.: Exact Numerical Methods in the Boundary Layer Theory. Fluid Dynamics Transactions, Vol. 1. Ed. Fiszdon. PWN. Polish Scientific Publishers, 1964.

21. Dorodnitsyn, A. A.: General Method of Integral Relations and Its Application to Boundary Layer Theory. Advances in Aeronautical Sciences, Vol. 3, 1960. Pergamon Press.

22. Belotserkovskii, O. M. and Chushkin, P. I.: The Method of Integral Relations. Basic Developments in Fluid-dynamics, ed. Maurice Holt. Acad. Press, 1965.

23. Belotserkovskii, O. M. and Chushkin, P. I.: A Numerical Method of Integral Relations. Zh. vych. mat. 2, No. 5, 731-759, 1962.

24. Fox, L.: Numerical Solution of Ordinary and Partial Differential Equations. Pergamon Press, 1962.

25. Ralston, A. and Wilf, H. S.: Mathematical Methods for Digital Computers. John Wiley and Sons, 1960.

26. Dudgeon, E. H. and Lowe, I. R. G.: On the 70KW Plasma Jet. (To be published).

27. Lipstein, N. J.: Low Velocity Sudden Expansion Pipe Flow. Trans. American Society of Heating, Refrigerating and Air Conditioning Engineers, Vol. 68, 1962.

28. Batchelor, G. K. and Shaw, F. S.: A Consideration of the Design of Wind-Tunnel Contractions. Australian Report ACA-4, ARC 7306, March 1944.

29. Lau, J.: Electrical Conductivity of Inert Gases-Seed Combination in Shock Tubes. Canadian Journal of Physics, Vol. 42, Aug. 1964.

30. Dudgeon, E. H. and Michaud, G.: Calculations of the Electrical Conductivity of Helium and Argon Seeded with Potassium. NRC Mech. Eng. Report MT-52, Dec. 1963.

31. Rosa, R. J.: Physical Principles of Magnetohydrodynamic Power Generation. Physics of Fluids, Vol. 4, No. 2, Feb. 1961.

32. Kyser, J. B.: Development of a Tracer-Spark Technique for the Stüdy of Hypervelocity Flow Fields. Stanford Univ. Dept. of Aeronautics and Astronautics, Tech. Rept. No. 2, May 1964.

33. Kyser, J. B.: Additional Study and Further Development of the Tracer-Spark Technique for Flow Velocity Measurements. NASA Cr 760, May 1967.

34. Lau, J. and Mills, E.: Electrical Conductivity of Inert Gases-Seed Combination in Shock Tubes. II. Reflected Shock Measurements in Argon. Can. Journal of Physics, Vol. 43, July 1965.

35. Kyoichi Kuriki: An Experimental Study on the Plasma Flow Through a Magnetic Nozzle. Aeronautical Research Institute, Univ. of Tokyo, Rept. No. 380, March 1964.

36 Zukoski, E. E. and Pinchak, A. C.: Gas Phase and Surface Phenomena in Seeded Plasmas. AIAA Jnl., Vol. 3, No. 2, 1965.

37. Bekiarian, A.: Etude des Limitations de la densite de courant au voi sinage d'une electrode. International Symposium on MHD Electrical Power Generation, Paris, July 1964.

38. Maslennikov, N. M. and Germanyuk, V. N.: Experimental Investigation of the Electrical Conductivity in a Stream of Argon and Potassium. High Temperature, Vol. 3, No. 4, July 1965.

39. Chung, P. M. and Blankenship, V. D.: Theory of Electrostatic Double Probe Comprised of Two Parallel Plates. AIAA Paper No. Second Annual Meeting, July 1965.

40. Hoppmann, R. F.: An Experimental Investigation of the Conduction of Electric Current Between Cold Electrodes in Shock-Ionized Air Plasmas. Aerospace Research Laboratories Report ARL 66-0182, Sept. 1966.

41. Toshitsugii Hara and Motokazu Uchida: Electrode Voltage Drop in a Seeded Plasma. Jap. Jnl. of Applied Physics, Vol. 7, No. 2, Feb. 1968.

42. Cobine, J. D.: Gaseous Conductors. Dover, 1958.

43. Haydon, S. C.: Discharge and Plasma Physics. Dept. of Univ. Extension, Univ. of New England, Armidale, 1964.

44. Squire, H. B. and Winter, K. G.: The Secondary Flow in a Cascade of Airfoils in a Non-Uniform Stream. Jnl. of Aero. Sciences, April 1951.

45. Hawthorne, W. R. and Martin, Moira E.: The Effect of Density Gradient and Shear on the Flow Over a Hemisphere. Proc. Royal Society of London, Ser. A, Vol. 232, 1955.

46. Von Karman, Theodore and Tsien, Hsue-Shen: Lifting-Line Theory for a Wing in Non-Uniform Flow. Quarterly of Applied Maths., Vol. III, April 1945.

47. Hawthorne, W. R.: Secondary Circulation in Fluid Flow. Proc. Royal Society of London, Ser. A, Vol. 26, 1951.

48. Dean, W. R.: Streamline Motion of Fluid in a Curved Pipe. Phil. Mag. (7), Vol. 5, 1928.

49. White, C. M.: Streamline Flow Through Curved Pipes. Proc. Royal Society of London, 123A, 1929.

50. Adler, M.: Strömung in gekrümmten Rohren. Zeitschr. f. angew Math. u Mech., Vol. 14, Oct. 1934.

51. Cumming, H. G.: The Secondary Flow in Curved Pipes. A.R.C. R and M 2880, 1955.

52. Ward-Smith, A. J.: The Flow and Pressure Losses in Smooth Pipe Bends of Constant Cross-Section. Jnl. of Royal Aero. Society, Vol. 67, July 1963.

APPENDIX

INFLUENCE OF CROSSED ELECTRIC AND MAGNETIC FIELD ON SECONDARY FLOW IN A CURVED PIPE FLOW

The equations governing the flow of fluid under the action of an electromagnetic body force are given by (refer to Fig. 2):

$$v\frac{\partial v}{\partial r} + \frac{u}{r}\frac{\partial v}{\partial \theta} + w\frac{\partial v}{\partial z} - \frac{u^2}{r} = -\frac{1}{\rho}\frac{\partial p}{\partial r} + \frac{\bar{J}\times\bar{B}}{\rho}$$

$$v\frac{\partial u}{\partial r} + \frac{u}{r}\frac{\partial u}{\partial \theta} + w\frac{\partial u}{\partial z} - \frac{uv}{r} = -\frac{1}{\rho r}\frac{\partial p}{\partial \theta}$$

$$\frac{u}{r}\frac{\partial w}{\partial \theta} + v\frac{\partial w}{\partial r} + w\frac{\partial w}{\partial z} = -\frac{1}{\rho}\frac{\partial p}{\partial z}$$

The first equation can be simplified as follows:

$$\frac{\partial\left(\frac{v^2}{2}+\frac{u^2}{2}+\frac{w^2}{2}\right)}{\partial r} - u\frac{\partial u}{\partial r} - w\frac{\partial w}{\partial r} + \frac{u}{r}\frac{\partial v}{\partial \theta} + w\frac{\partial v}{\partial z} - \frac{u^2}{r} = -\frac{1}{\rho}\frac{\partial p}{\partial r} - \frac{|JB|_r}{\rho}$$

$$\frac{\partial \frac{V^2}{2}}{\partial r} - \frac{u}{r}\left(\frac{\partial ur}{\partial r} - \frac{\partial v}{\partial \theta}\right) + w\left(\frac{\partial v}{\partial z} - \frac{\partial w}{\partial r}\right) = -\frac{1}{\rho}\frac{\partial p}{\partial r} + \frac{|JB|_r}{\rho}$$

Similarly the other two equations become:

and $$\frac{1}{r}\frac{\partial \frac{V^2}{2}}{\partial \theta} + v\left(\frac{1}{r}\frac{\partial ur}{\partial r} - \frac{1}{r}\frac{\partial v}{\partial \theta}\right) - w\left(\frac{1}{r}\frac{\partial w}{\partial \theta} - \frac{\partial u}{\partial z}\right) = -\frac{1}{\rho r}\frac{\partial p}{\partial \theta}$$

$$\frac{\partial \frac{V^2}{2}}{\partial z} + u\left(\frac{1}{r}\frac{\partial w}{\partial \theta} - \frac{\partial u}{\partial z}\right) - v\left(\frac{\partial v}{\partial z} - \frac{\partial w}{\partial r}\right) = -\frac{1}{\rho}\frac{\partial p}{\partial z}$$

In cylindrical coordinates

$$\bar{\omega} = \nabla\times\bar{V} = \bar{i}\xi + \bar{j}\eta + \bar{k}\zeta$$

where $$\xi = \frac{\partial v'}{\partial z} - \frac{\partial w}{\partial r} \quad , \eta = \frac{1}{r}\frac{\partial w}{\partial \theta} - \frac{\partial u}{\partial z} \quad , \zeta = \frac{1}{r}\frac{\partial ur}{\partial r} - \frac{1}{r}\frac{\partial v}{\partial \theta}$$

are the components of vorticity along the θ, r, and z directions respectively.

The three equations are therefore:

$$(1) \quad \frac{\partial \frac{V^2}{2}}{\partial r} - (u\zeta - w\xi) = -\frac{1}{\rho}\frac{\partial p}{\partial r} - \frac{|JB|_r}{\rho}$$

$$(2) \quad \frac{1}{r}\frac{\partial \frac{V^2}{2}}{\partial \theta} - (w\eta - v\zeta) = -\frac{1}{\rho}\frac{\partial p}{\partial \theta}$$

$$(3) \quad \frac{\partial \frac{V^2}{2}}{\partial z} - (v\xi - u\eta) = -\frac{1}{\rho}\frac{\partial p}{\partial z}$$

Taking derivatives of (1) and (3):

$$\frac{\partial^2 \frac{V^2}{2}}{\partial r \partial z} - u\frac{\partial \zeta}{\partial z} - \zeta\frac{\partial u}{\partial z} + w\frac{\partial \xi}{\partial z} + \xi\frac{\partial w}{\partial z} = -\frac{1}{\rho}\frac{\partial^2 p}{\partial r \partial z} - \frac{\partial \left|\frac{JB}{\rho}\right|_r}{\partial z}$$

$$\frac{\partial^2 \frac{V^2}{2}}{\partial r \partial z} - v\frac{\partial \xi}{\partial r} - \xi\frac{\partial v}{\partial r} + u\frac{\partial \eta}{\partial r} + \eta\frac{\partial u}{\partial r} = -\frac{1}{\rho}\frac{\partial^2 p}{\partial r \partial z}$$

Subtracting:

$$-u\left(\frac{\partial \zeta}{\partial z} + \frac{\partial \eta}{\partial r}\right) + w\frac{\partial \xi}{\partial z} + v\frac{\partial \xi}{\partial r} + \xi\left(\frac{\partial w}{\partial z} + \frac{\partial v}{\partial r}\right) - \zeta\frac{\partial u}{\partial z} - \eta\frac{\partial u}{\partial r} = -\frac{\partial \left|\frac{JB}{\rho}\right|_r}{\partial z}$$

But $$\frac{\partial \zeta}{\partial z} + \frac{\partial \eta}{\partial r} + \frac{\eta}{r} + \frac{1}{r}\frac{\partial \xi}{\partial \theta} = 0$$

and $$\frac{\partial w}{\partial z} + \frac{\partial v}{\partial r} + \frac{v}{r} + \frac{1}{r}\frac{\partial u}{\partial \theta} = 0$$

$$\therefore \quad (4) \quad \frac{u}{r}\frac{\partial \xi}{\partial \theta} + \frac{v}{r}\frac{\partial \xi r}{\partial r} + w\frac{\partial \xi}{\partial z} - \left[\frac{\xi}{r}\frac{\partial u}{\partial \theta} + \frac{\eta}{r}\frac{\partial ur}{\partial r} + \zeta\frac{\partial u}{\partial z}\right] = -\frac{\partial \left|\frac{JB}{\rho}\right|_r}{\partial z}$$

the other equations become:

$$(5)\qquad \frac{u}{r}\frac{\partial \zeta}{\partial \theta} + \frac{v}{r}\frac{\partial \zeta r}{\partial r} + w\frac{\partial \zeta}{\partial z} - \left[\frac{\xi}{r}\frac{\partial w}{\partial \theta} + \frac{\eta}{r}\frac{\partial wr}{\partial r} + \zeta\frac{\partial w}{\partial z}\right] = \frac{1}{\rho r}\frac{\partial \left|\frac{JB}{\rho}\right|_r}{\partial \theta}$$

$$(6)\qquad \frac{u}{r}\frac{\partial \eta}{\partial \theta} + \frac{v}{r}\frac{\partial \eta r}{\partial r} + w\frac{\partial \eta}{\partial z} - \left[\frac{\xi}{r}\frac{\partial v}{\partial \theta} + \frac{\eta}{r}\frac{\partial vr}{\partial r} + \zeta\frac{\partial v}{\partial z}\right] = 0$$

or, in vector form:

$$\bar{V}\cdot\nabla\bar{\omega} - \bar{\omega}\cdot\nabla V = \nabla\times\frac{\bar{J}\times\bar{B}}{\rho}$$

In the following we shall estimate roughly the development of secondary flow due to a small shear upstream of the bend in a main flow under the influence of an electromagnetic force (as calculated in section 3.4). As seen in the results of section 3.4, the flow consists mainly of a longitudinal velocity $U \doteq U(r)$ and $v \doteq 0$, and $\bar{\xi} = \frac{JB}{\rho u}$ along a greater part of the bend. As a first approximation, we shall assume

$$u = U(r) + u'(r,\theta,z)$$

$$v = v'(r,\theta,z)$$

$$w = w'(r,\theta,z)$$

$$\xi = \xi'(r,\theta,z)$$

$$\eta = \eta'(r, \theta, z)$$

$$\zeta = \frac{|JB|_r}{\rho u} + \zeta'(r, \theta, z)$$

$$u'(r, 0, z) = u_0(z)$$

$$\eta'(r, 0, z) = -\frac{\partial u_0(z)}{\partial z}$$

$$v'(r,0,z) = w'(r,0,z) = \xi'(r, 0, z) = \zeta'(r, 0, z) = 0$$

where primed quantities denote small perturbations which constitute the secondary flow.

Substituting into equation (4) and linearizing,

$$\frac{U}{r}\frac{\partial \xi'}{\partial \theta} - \eta'\frac{\partial U}{\partial r} + \frac{\eta' U}{r} - \zeta\frac{\partial u'}{\partial z} = -\frac{\partial \left|\frac{JB}{\rho}\right|_r}{\partial z}$$

$$(7) \quad \therefore \quad \frac{\partial \xi'}{\partial \theta} = \eta'\left(\frac{r}{U}\frac{\partial U}{\partial r} - 1\right) + \frac{|JB|_r\, r}{\rho U^2}\frac{\partial u'}{\partial z} - \frac{r}{U}\frac{\partial \left|\frac{JB}{\rho}\right|_r}{\partial z}$$

The variation of U is approximated as follows:

$$\zeta = \frac{|JB|_r}{\rho u} + \zeta' = \frac{1}{r}\frac{\partial U_r}{\partial r} + \frac{1}{r}\frac{\partial u' r}{\partial r} - \frac{1}{r}\frac{\partial v'}{\partial \theta}$$

$$\therefore \quad \frac{1}{r}\frac{\partial U_r}{\partial r} = \frac{|JB|_r}{\rho u}$$

$$\therefore \quad \frac{\partial U}{\partial r} = \frac{|JB|_r}{\rho u} - \frac{U}{r}$$

Substituting in equation (7),

$$(8) \quad \frac{\partial \xi'}{\partial \theta} = \eta'\left(\frac{r}{U}\frac{|JB|_r}{\rho u} - 2\right) + \frac{|JB|_r\, r}{\rho U^2}\frac{\partial u'}{\partial z} - \frac{r}{U}\frac{\partial \left|\frac{JB}{\rho}\right|_r}{\partial z}$$

$$= -2\eta' + \frac{|JB|_r}{\rho U^2}\frac{\partial w'}{\partial \theta} - \frac{r}{U}\frac{\partial \left|\frac{JB}{\rho}\right|_r}{\partial z}$$

Since $\frac{U}{r}\frac{\partial w'}{\partial \theta} = -\frac{1}{\rho}\frac{\partial p}{\partial z}$ is assumed zero at inlet into bend, the second term is comparatively small, at least close to the inlet. Therefore, the growth of the longitudinal vorticity (ξ') which is responsible for most of the excess loss in a bend is modified by the electromagnetic term $\frac{r}{U} \frac{\partial \left|\frac{JB}{\rho}\right|_r}{\partial z}$. With appropriate shaping of magnetic field, equation (8) shows that it is possible to reduce this rate of growth depending on the current and magnetic field intensity available.

D	a_1	a_2	a_3	a_4	a_5	a_6	a_7	a_8	a_9	a_{10}
4	.09217	.01558	.00712	.00282	.00191	.00082	.00087	.00037	.00025	.00003
2	.06766	.00833	.00391	.00124	.00092	.00035	.00038	.00010	.00016	.00001
1	.04405	.00351	.00202	.00045	.00045	.00012	.00017	.00002	.00011	−.00002
.5	.02604	.00122	.00105	.00017	.00017	.00000	.00009	.00011	.000066	−.00004
.2857	.01623	.00046	.00065	.00005	.00015	.00001	.00006	−.00000	.00004	−.00004

TABLE 1

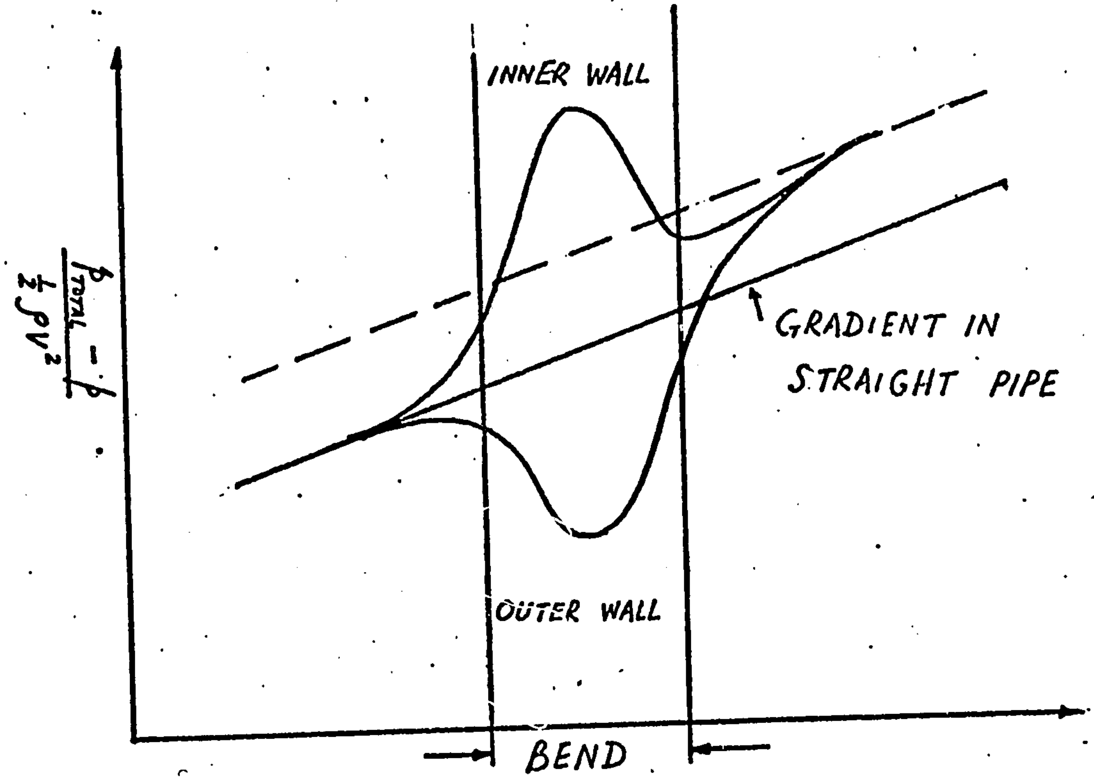

FIG. 1 PRESSURE DISTRIBUTION ALONG A BEND

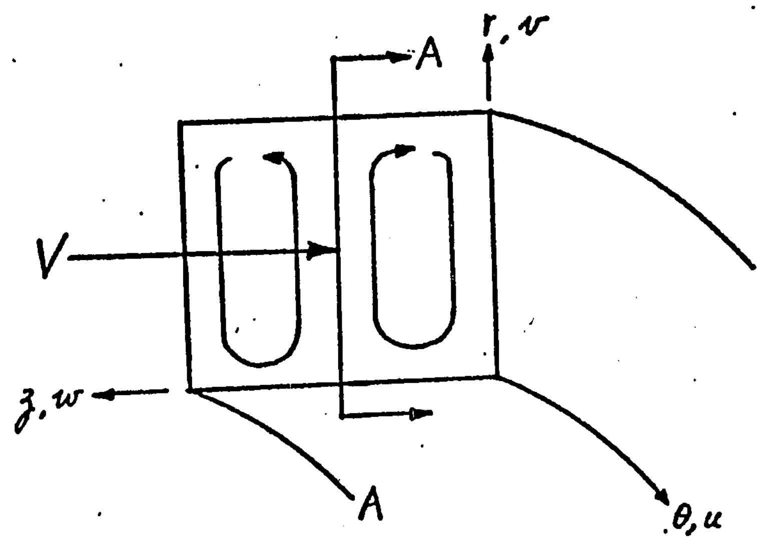

FIG. 2 SECONDARY FLOW IN A BEND

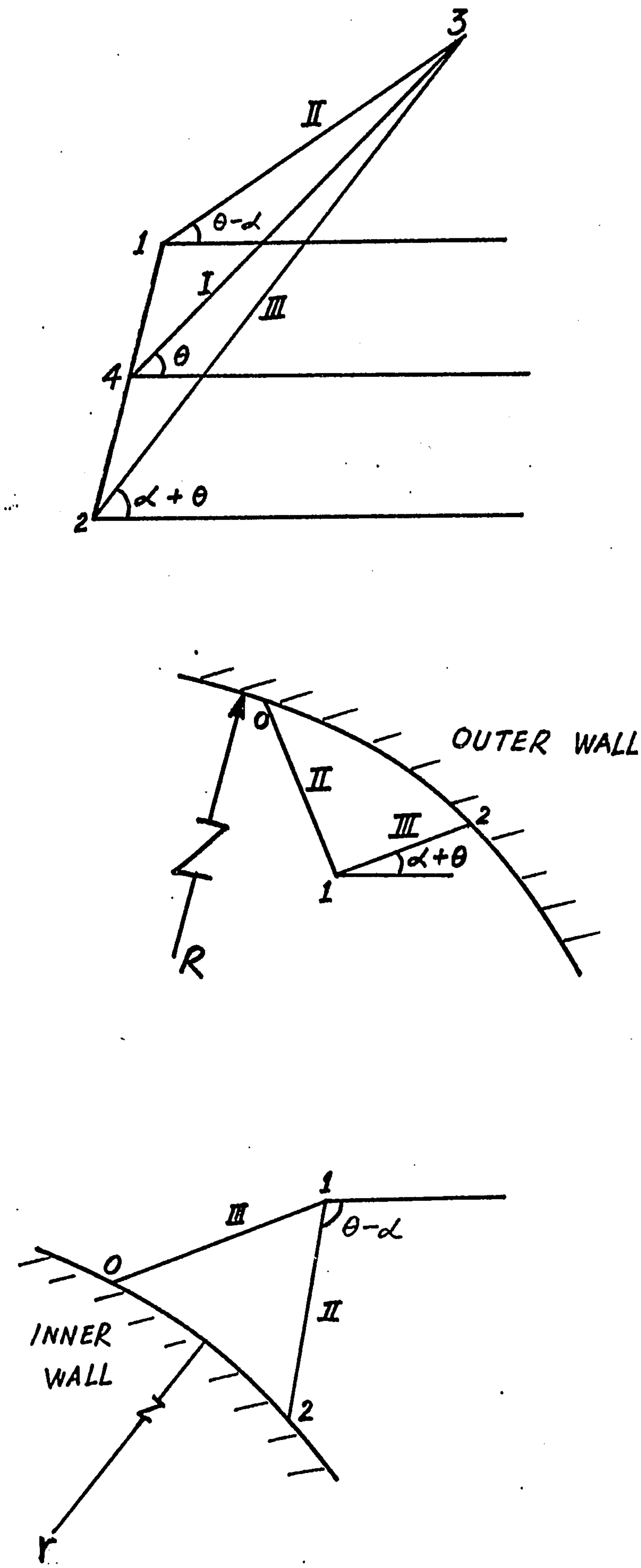

FIG. 3 CHARACTERISTIC NET CONSTRUCTION

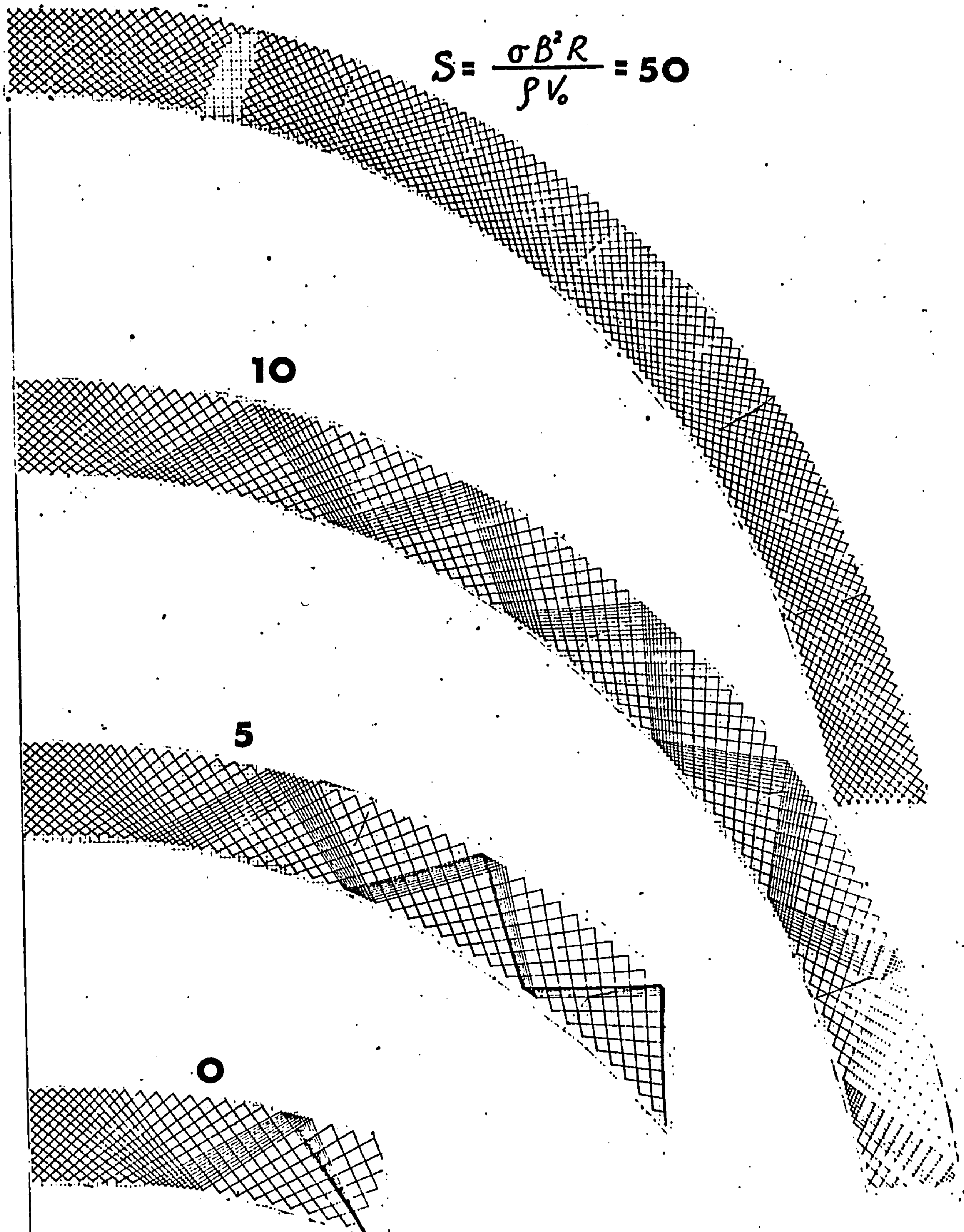

FIG. 4 $M_0 = 1.5$ $\frac{\text{CHANNEL HEIGHT}}{\text{RADIUS R}} = .1$

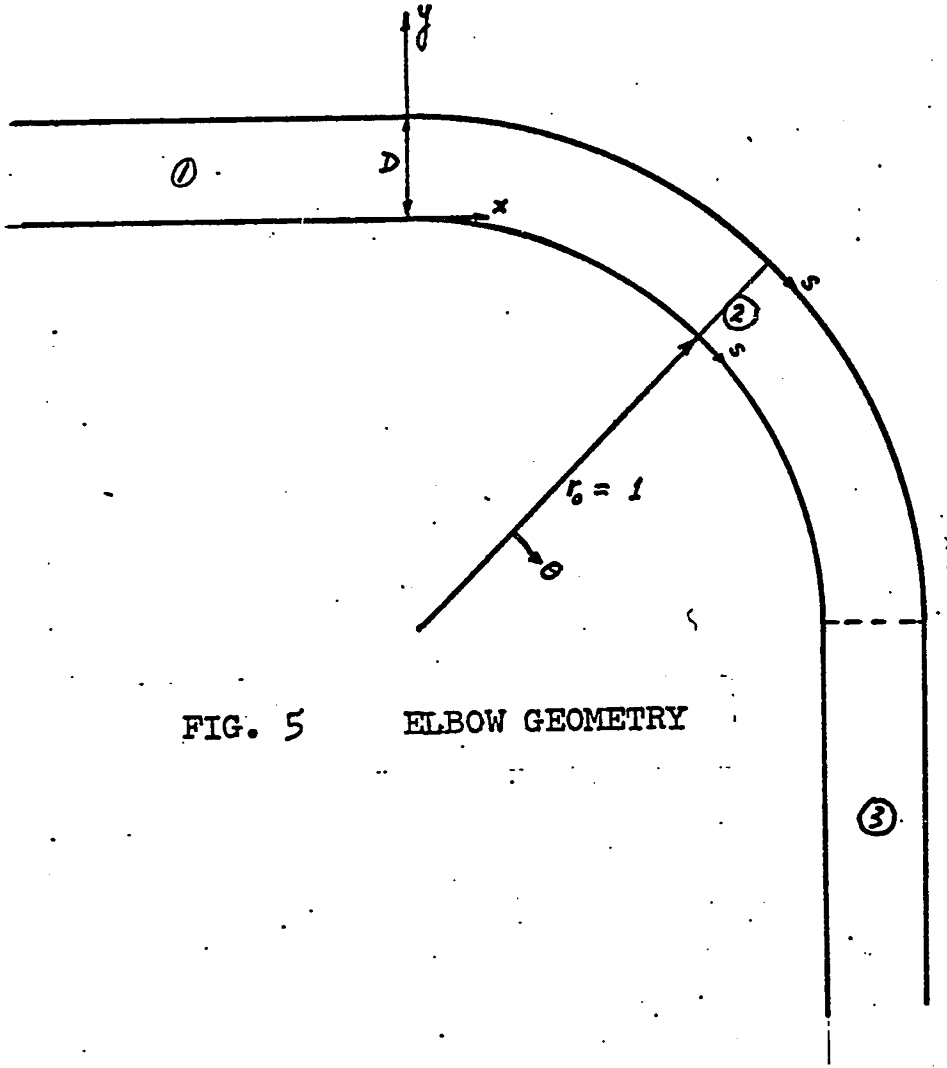

FIG. 5 ELBOW GEOMETRY

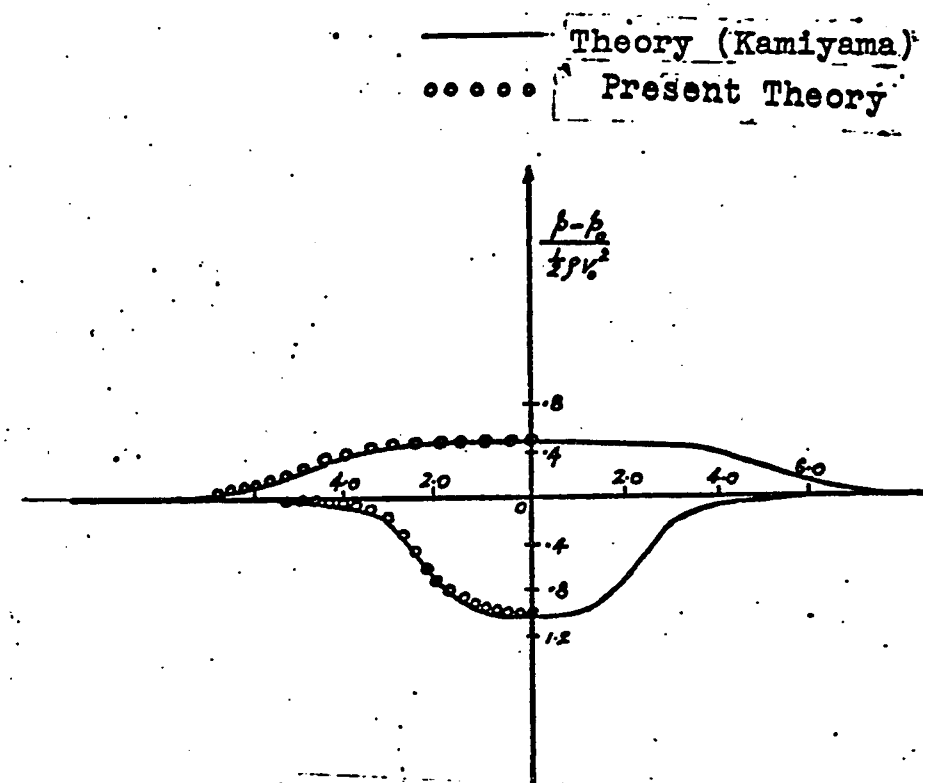

FIG. 6a D = 1

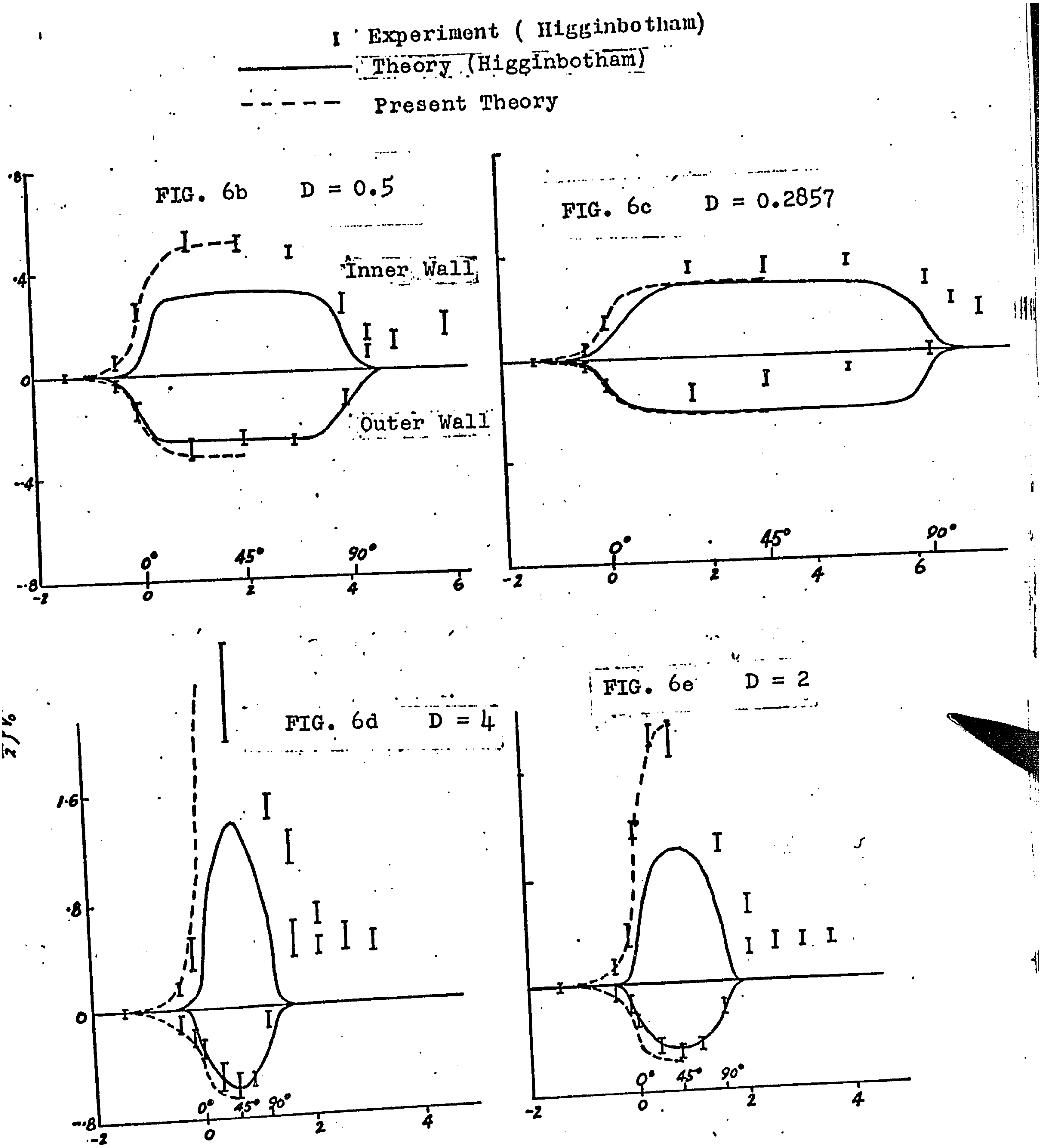
I Experiment (Higginbotham)
Theory (Higginbotham)
Present Theory
FIG. 6b D = 0.5
Inner Wall
Outer Wall
FIG. 6c D = 0.2857
FIG. 6d D = 4
FIG. 6e D = 2
0°
45°
90°
·8
·4
0
-·4
-·8
1·6
-2
2
4
6

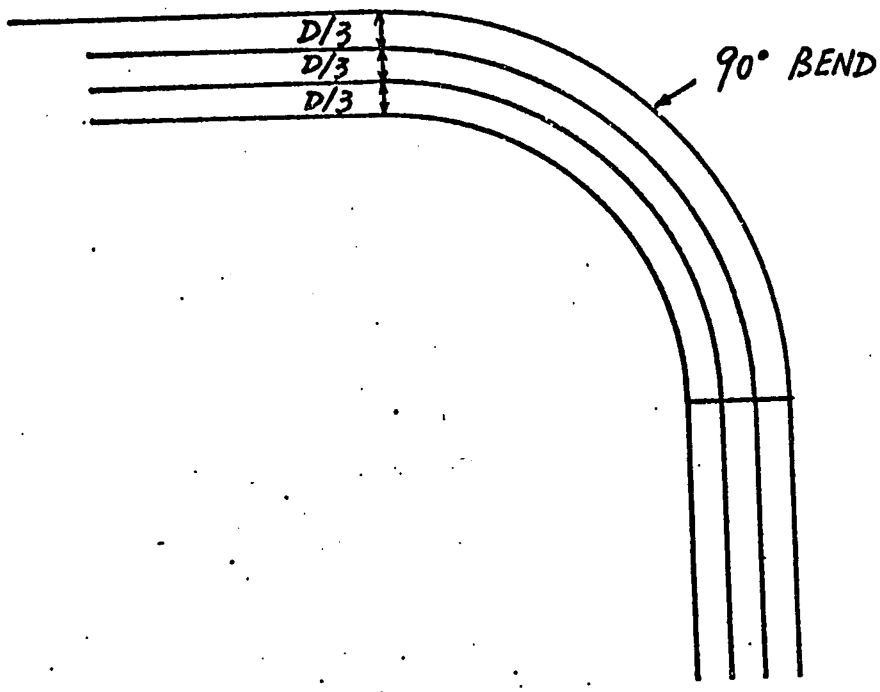

FIG. 7 DIVISION OF FLOW FIELD INTO STRIPS

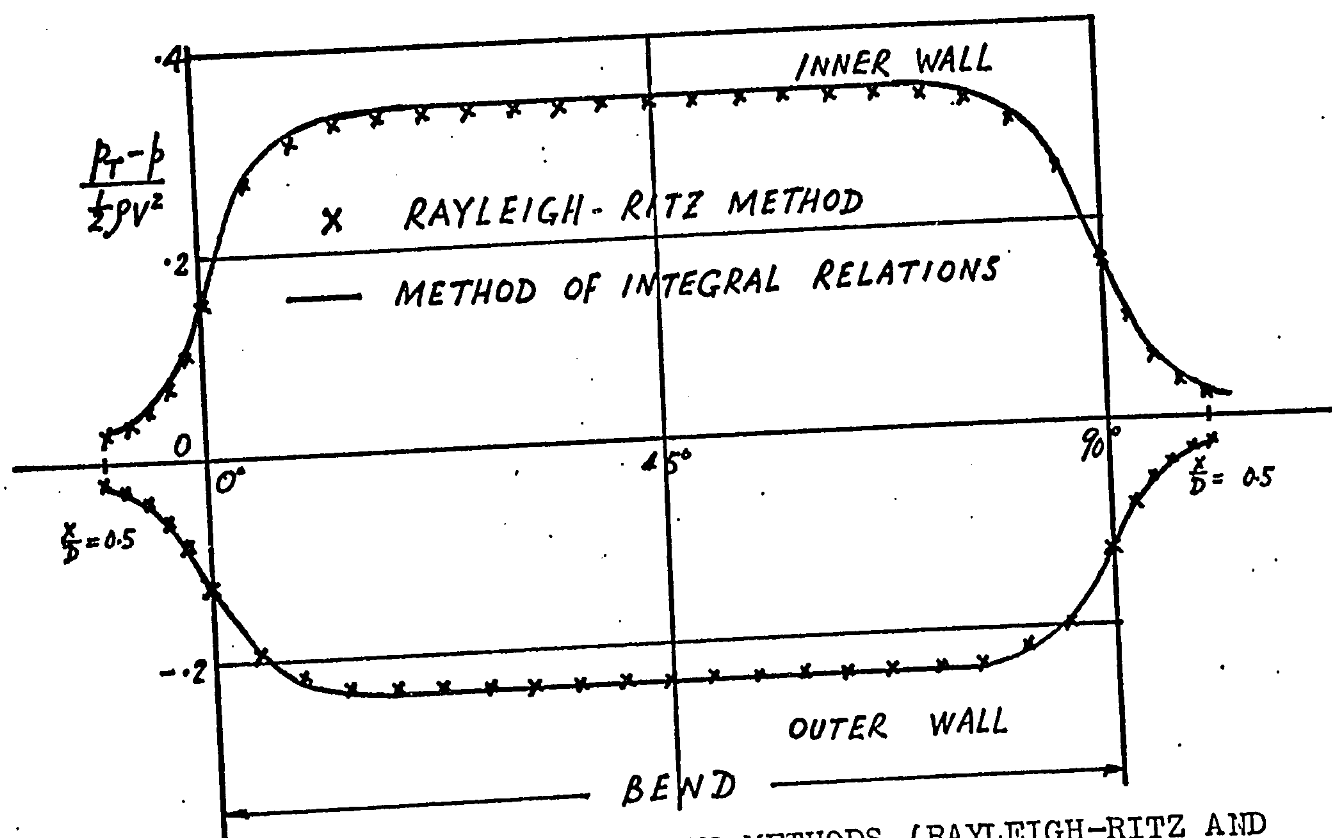

FIG. 8 COMPARISON OF TWO METHODS (RAYLEIGH-RITZ AND INTEGRAL RELATIONS)

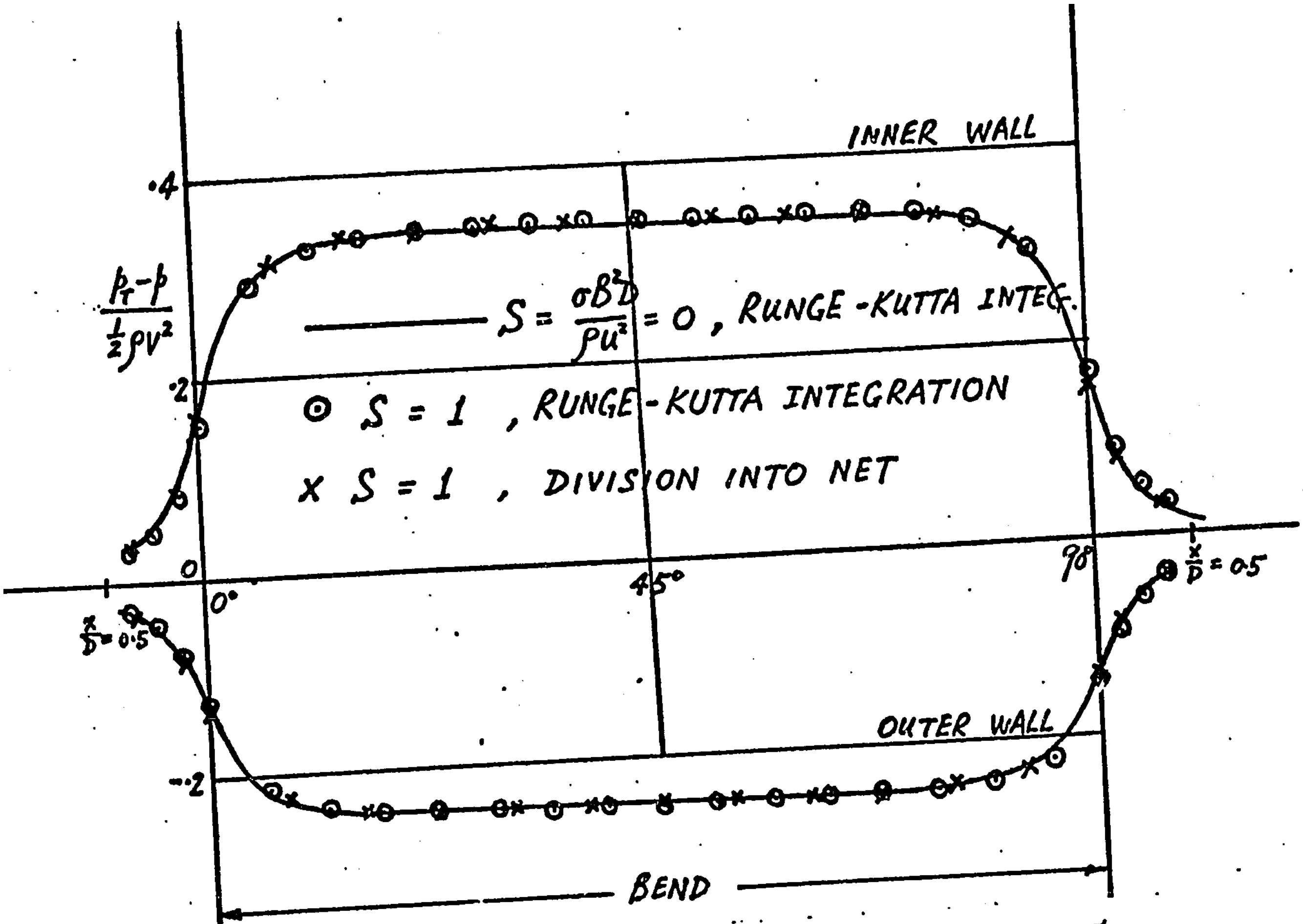

FIG. 9 PRESSURE COEFFICIENTS, M = 0.5 (METHOD OF INTEGRAL RELATIONS)

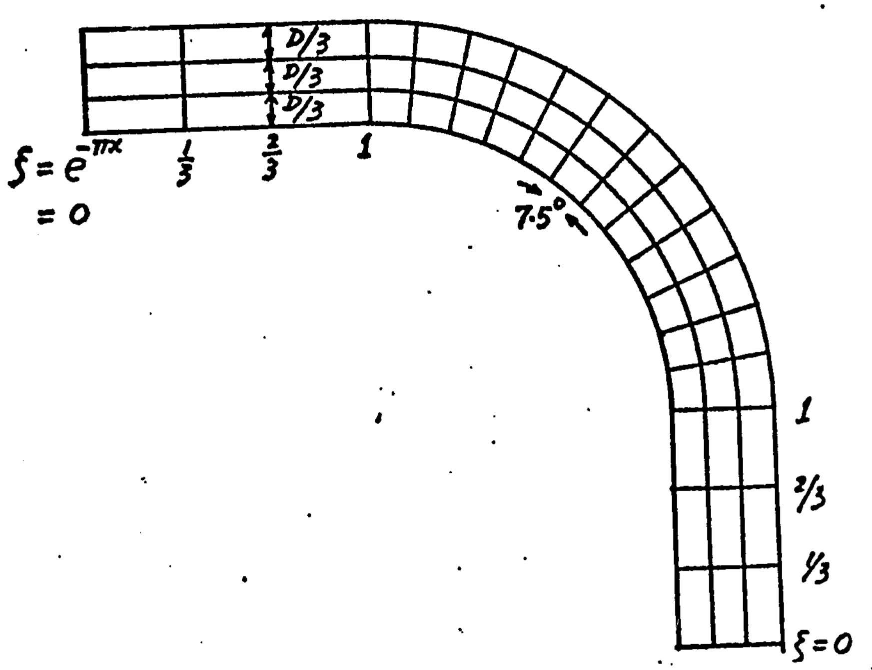

FIG. 10 DIVISION OF FLOW FIELD INTO NET

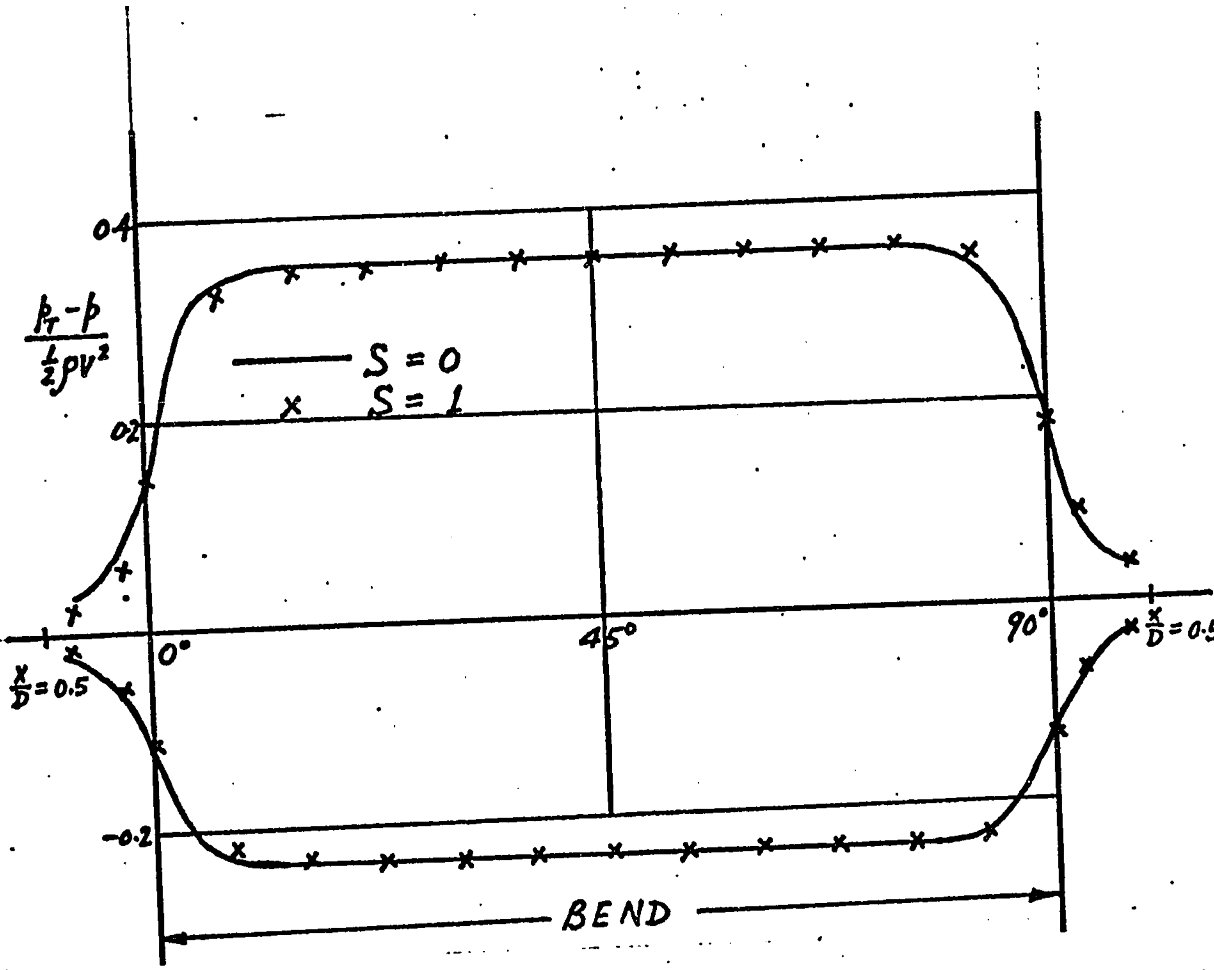

FIG. 11 PRESSURE COEFFICIENTS, M = 0.7 (METHOD OF INTEGRAL RELATIONS, DIVISION INTO NET)

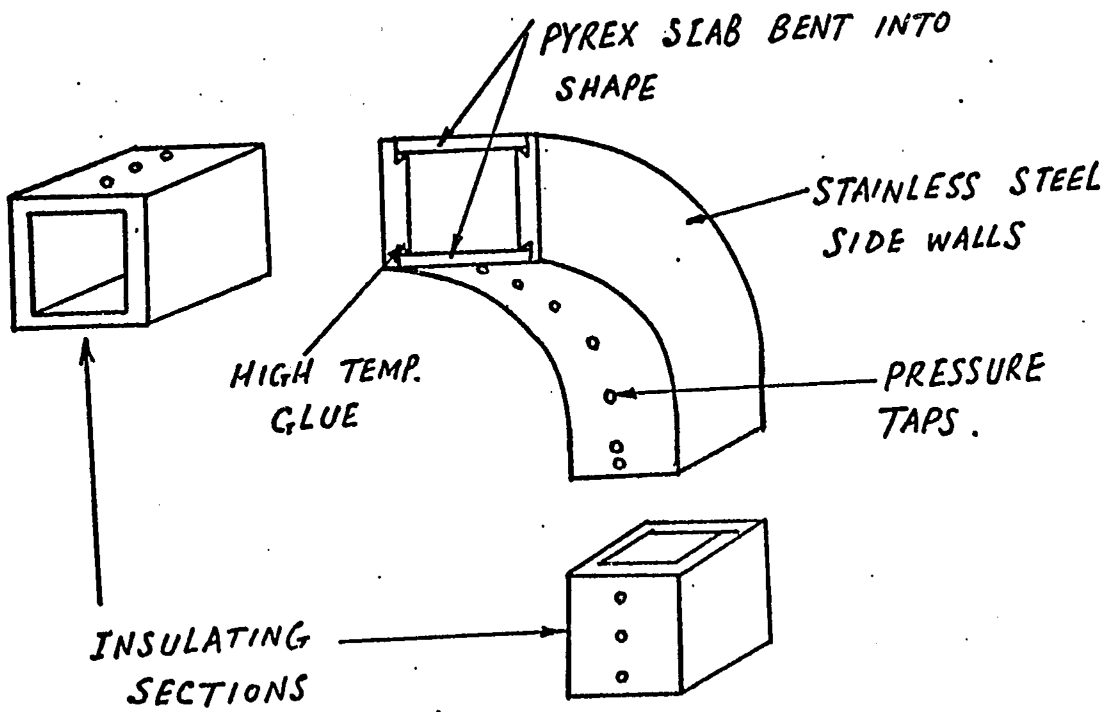

FIG. 12 BEND CONSTRUCTION

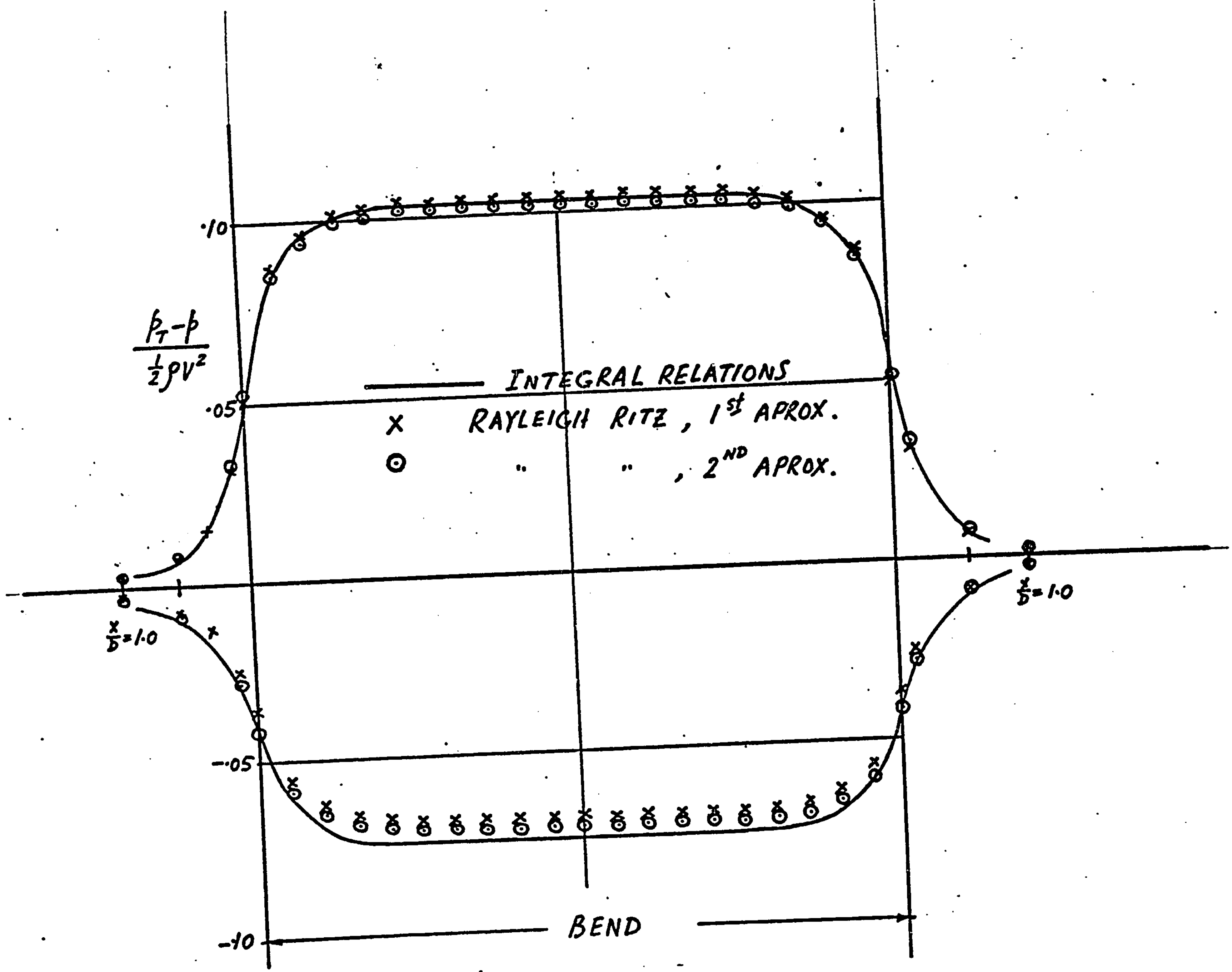

FIG. 13 INCOMPRESSIBLE FLOW (S = 0.6, COMPARISON OF TWO METHODS)

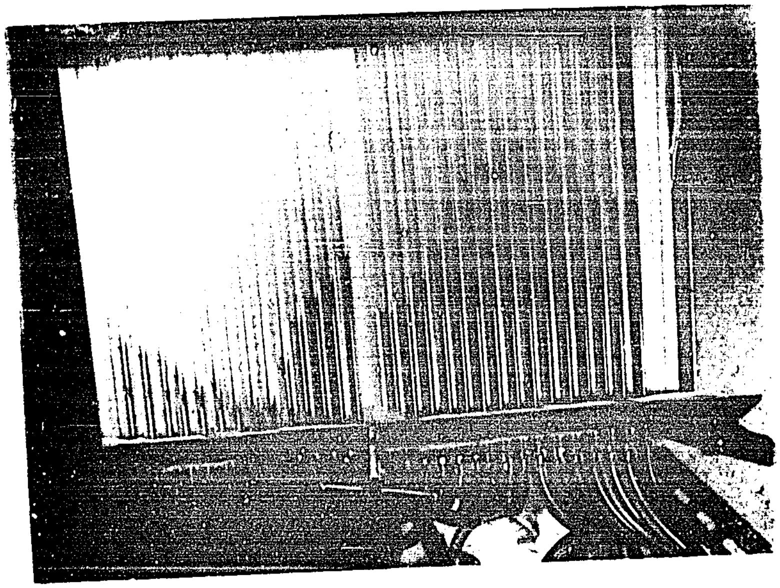

FIG. 14 a. TYPICAL MANOMETER RECORD

b. EXPERIMENTAL SET-UP

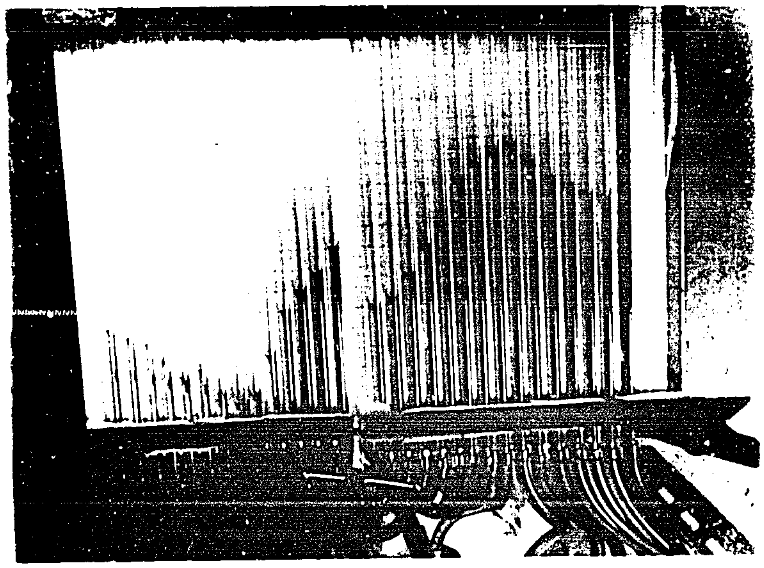

FIG. 14 a. TYPICAL MANOMETER RECORD

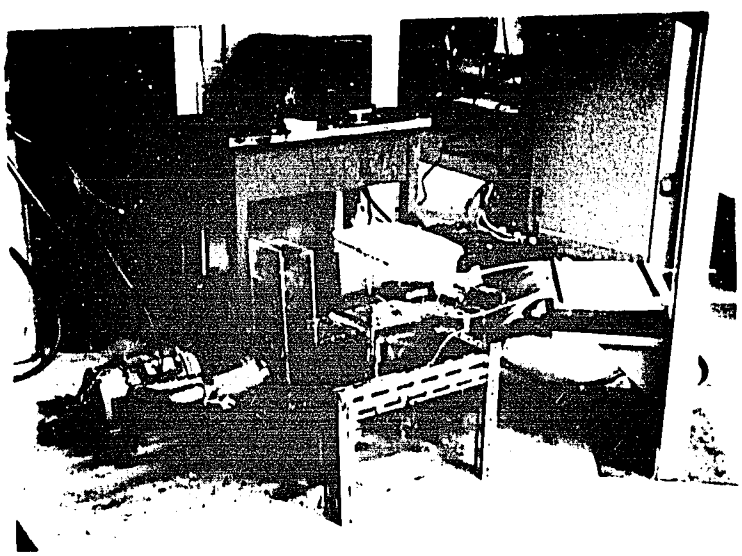

b. EXPERIMENTAL SET-UP

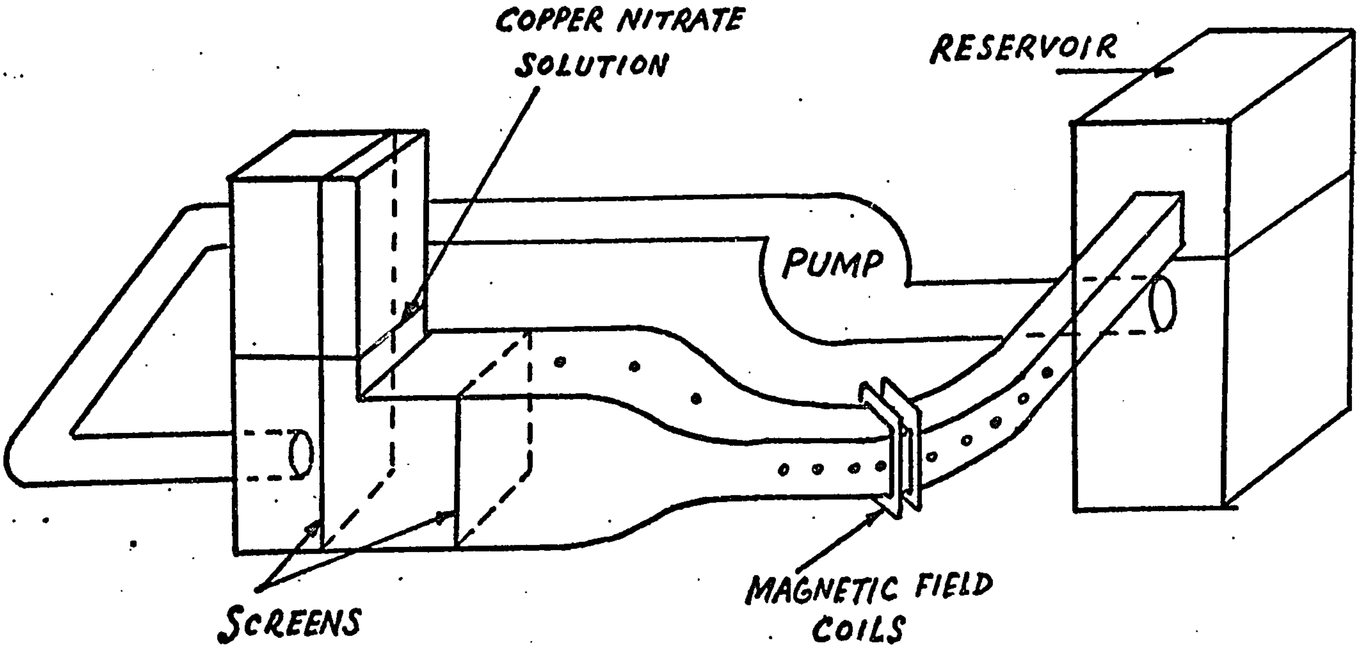

FIG. 15 SCHEMATIC OF SET-UP

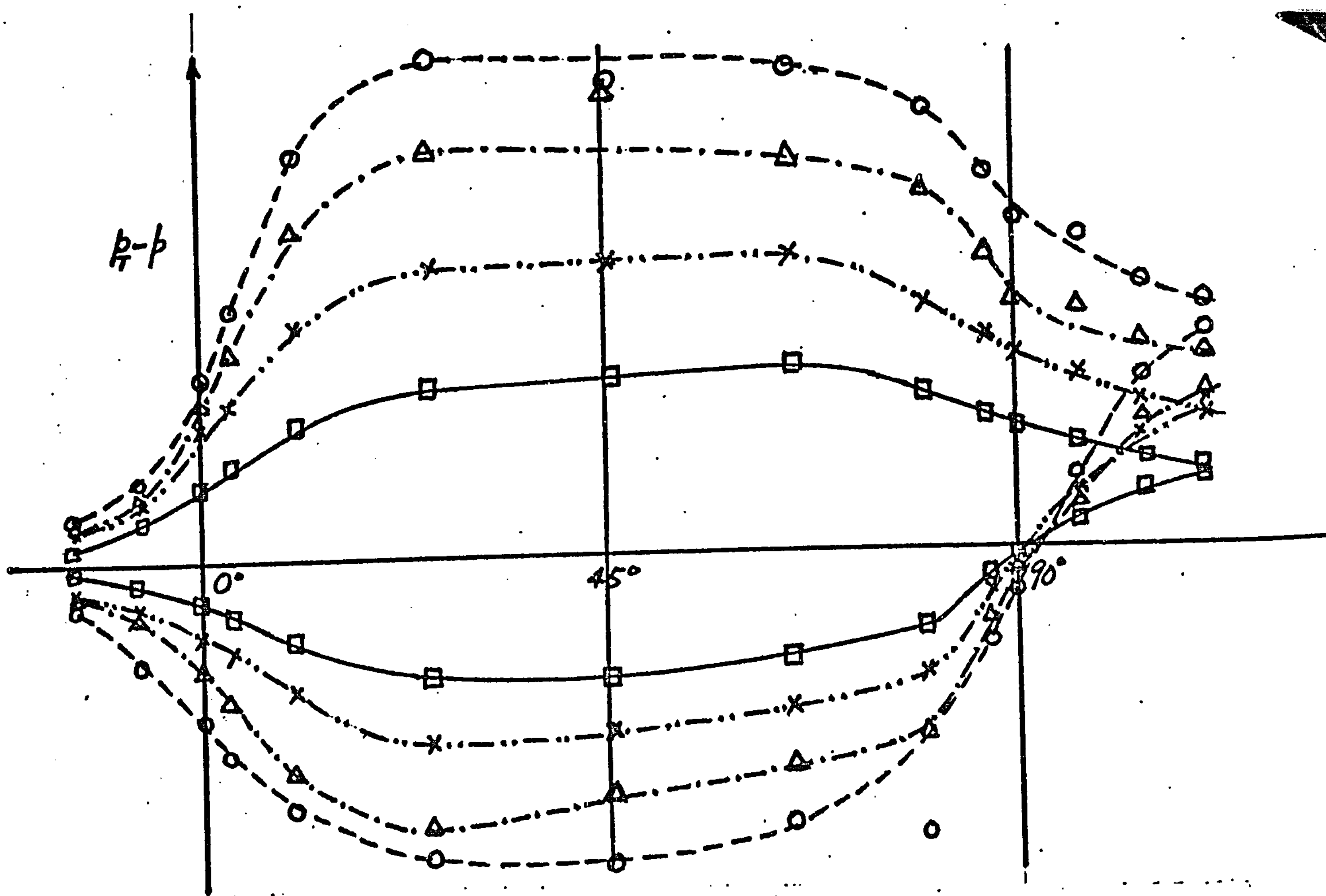

FIG. 16 PRESSURE ALONG BEND WITH WATER AT DIFFERENT SPEEDS

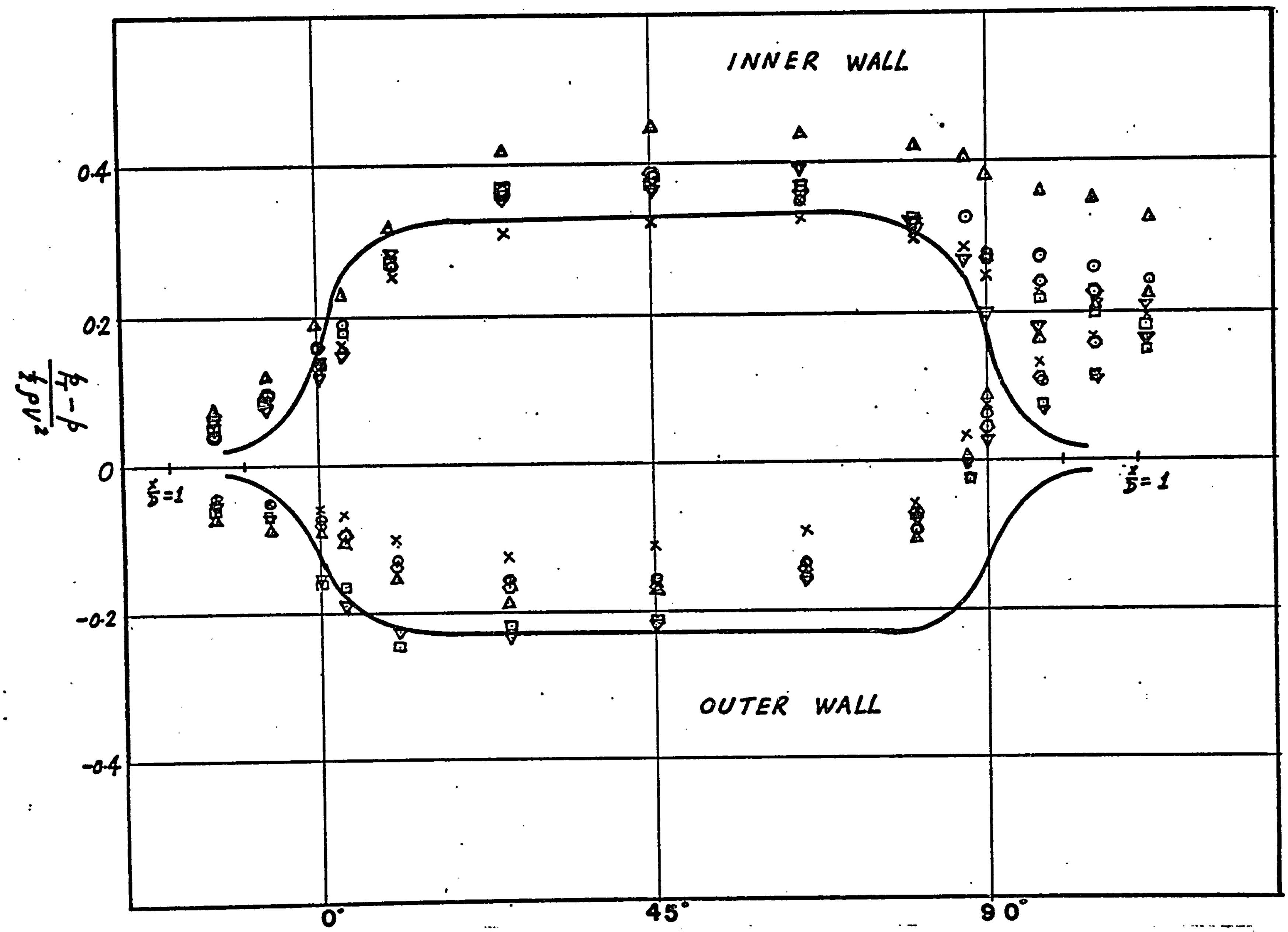

FIG. 17 PRESSURE COEFFICIENTS WITH ELECTROLYTES AT DIFFERENT SPEEDS

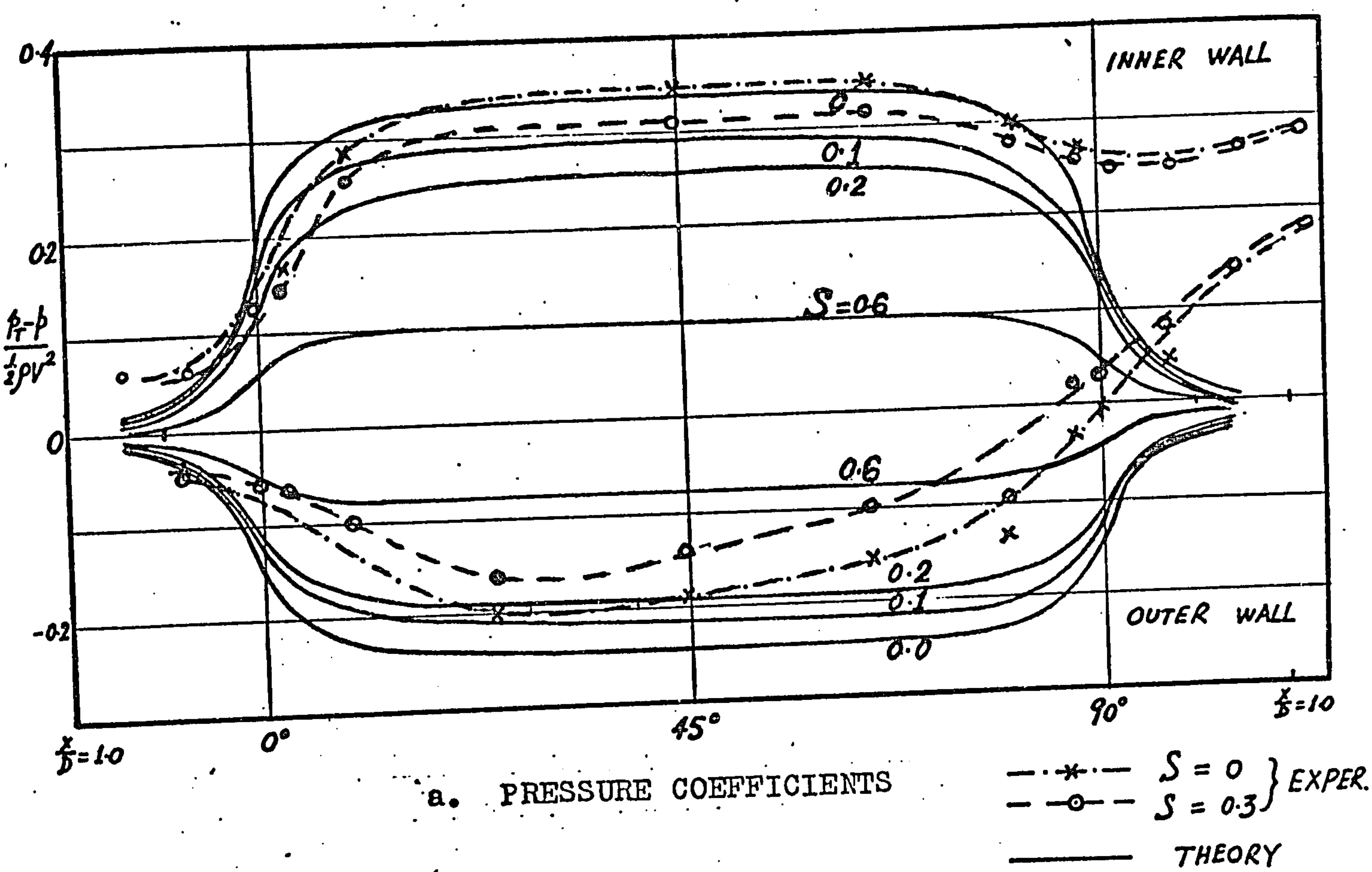

a. PRESSURE COEFFICIENTS

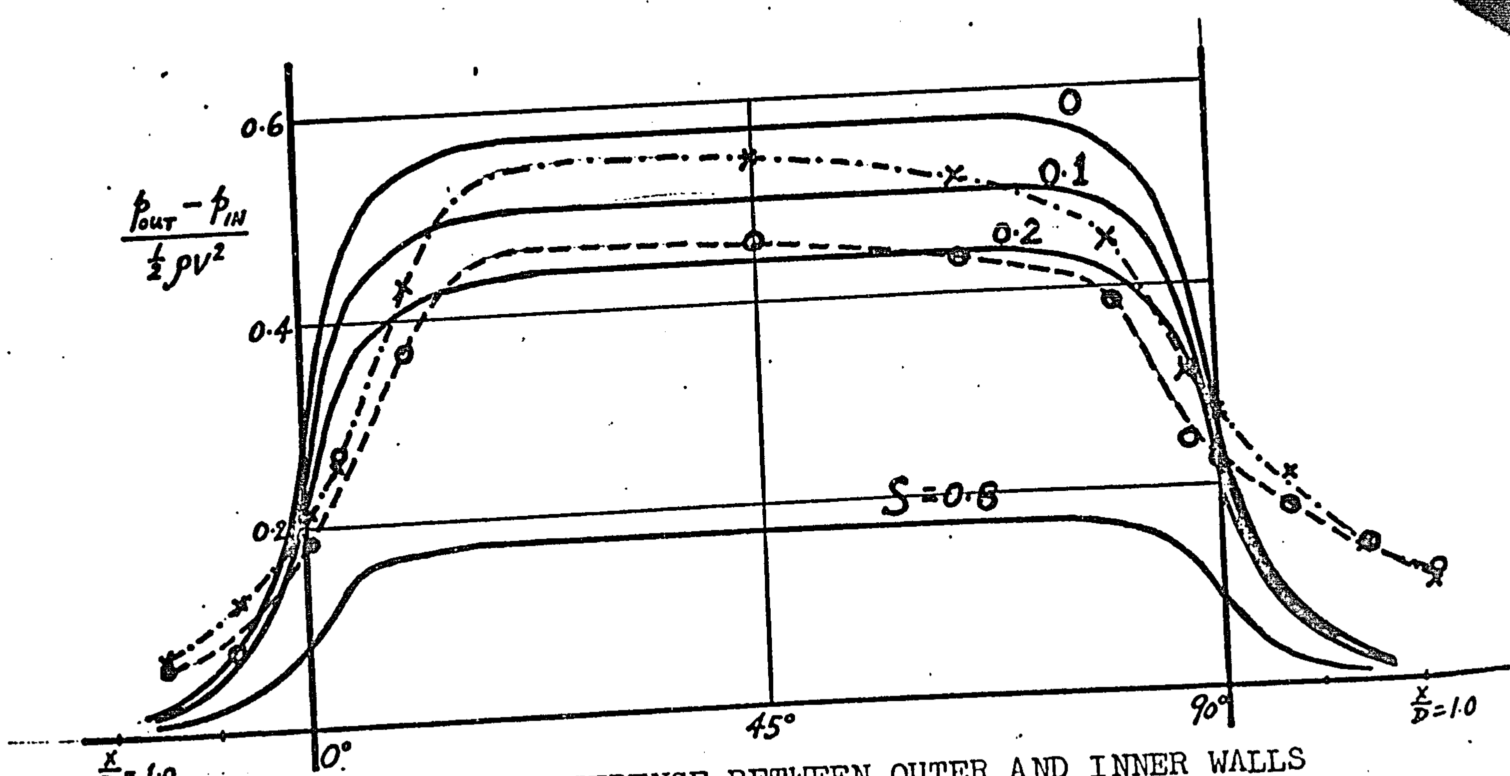

b. PRESSURE DIFFERENCE BETWEEN OUTER AND INNER WALLS

FIG. 18 EXPERIMENTAL RESULTS WITH ELECTROLYTE

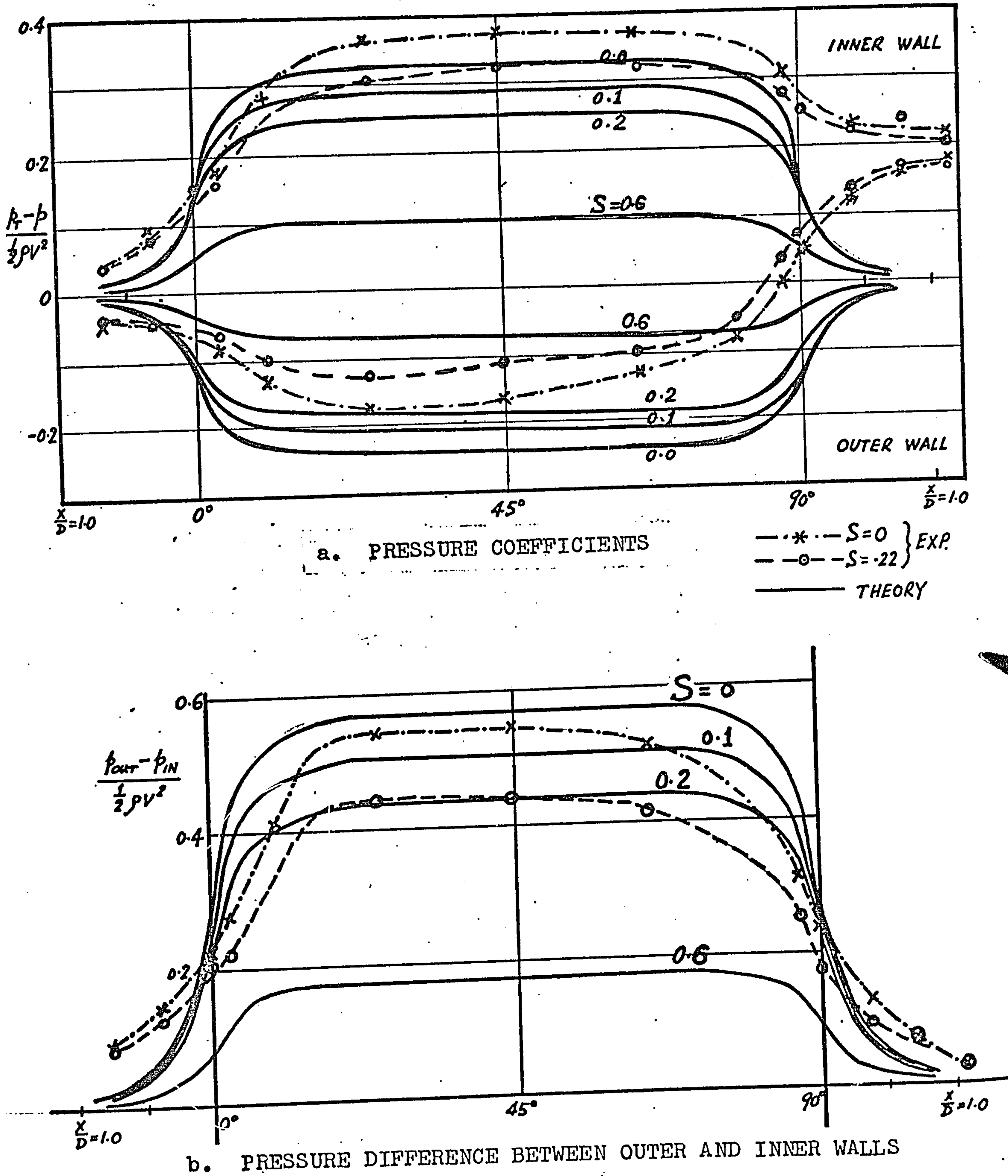

b. PRESSURE DIFFERENCE BETWEEN OUTER AND INNER WALLS

FIG. 19 EXPERIMENTAL RESULTS WITH ELECTROLYTE

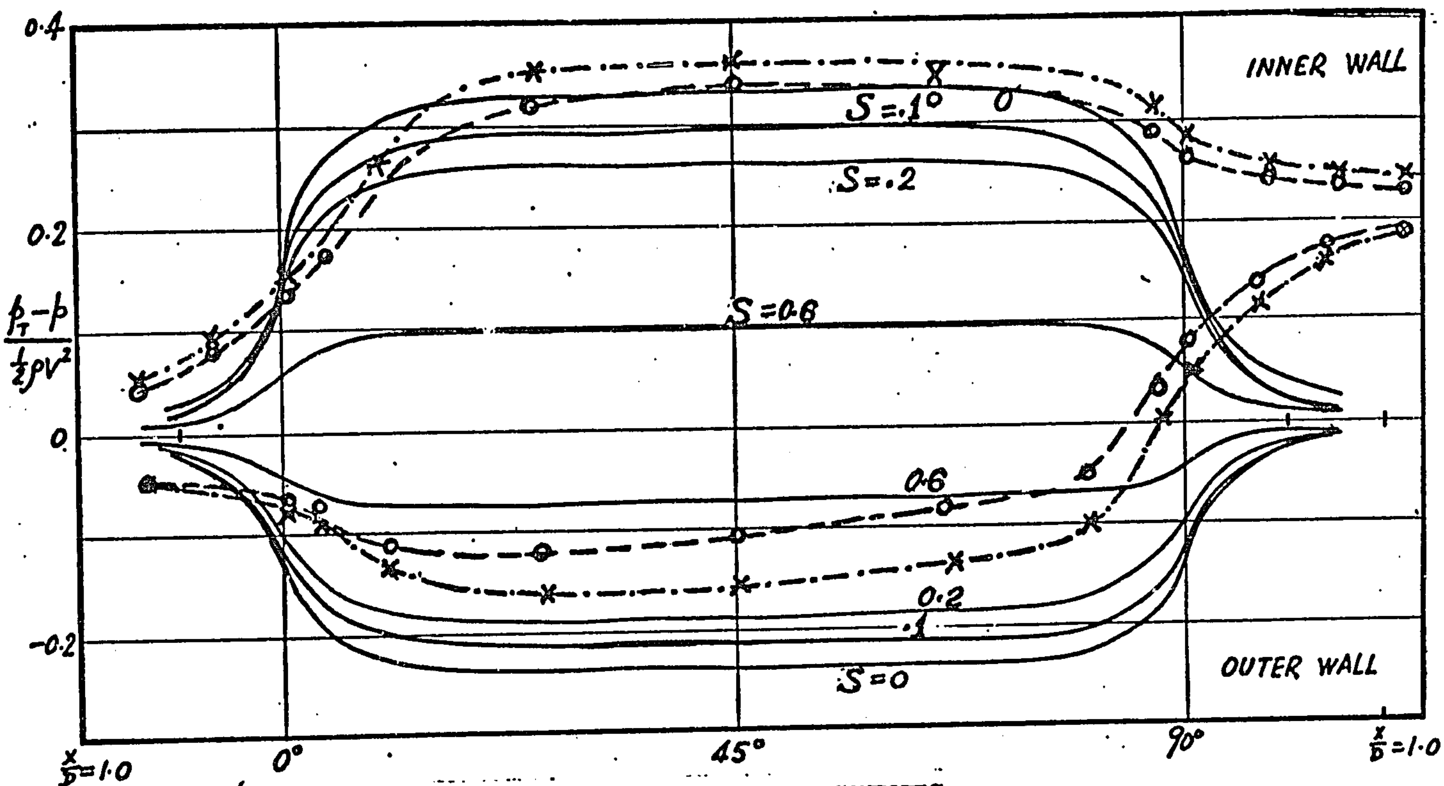

a. PRESSURE COEFFICIENTS

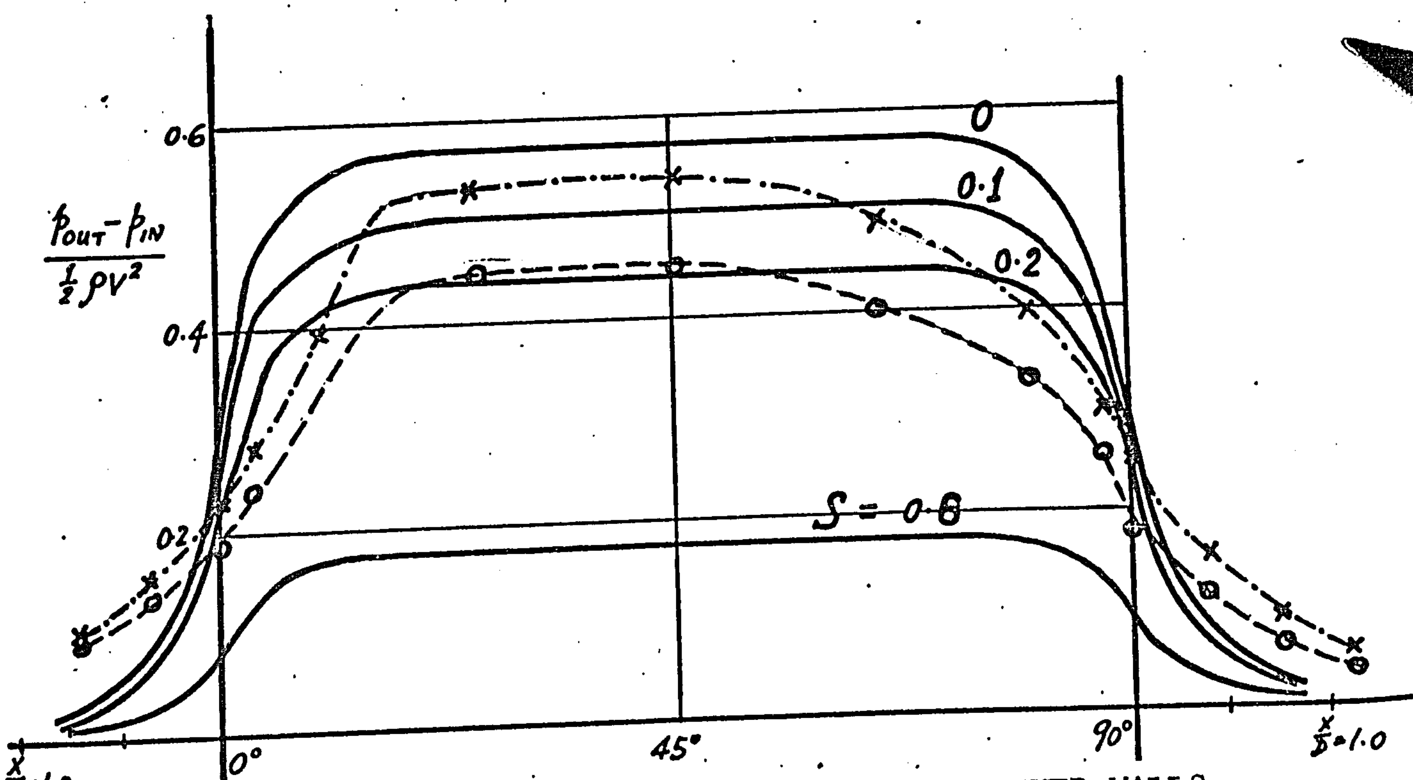

b. PRESSURE DIFFERENCE BETWEEN OUTER AND INNER WALLS

FIG. 20 EXPERIMENTAL RESULTS WITH ELECTROLYTE

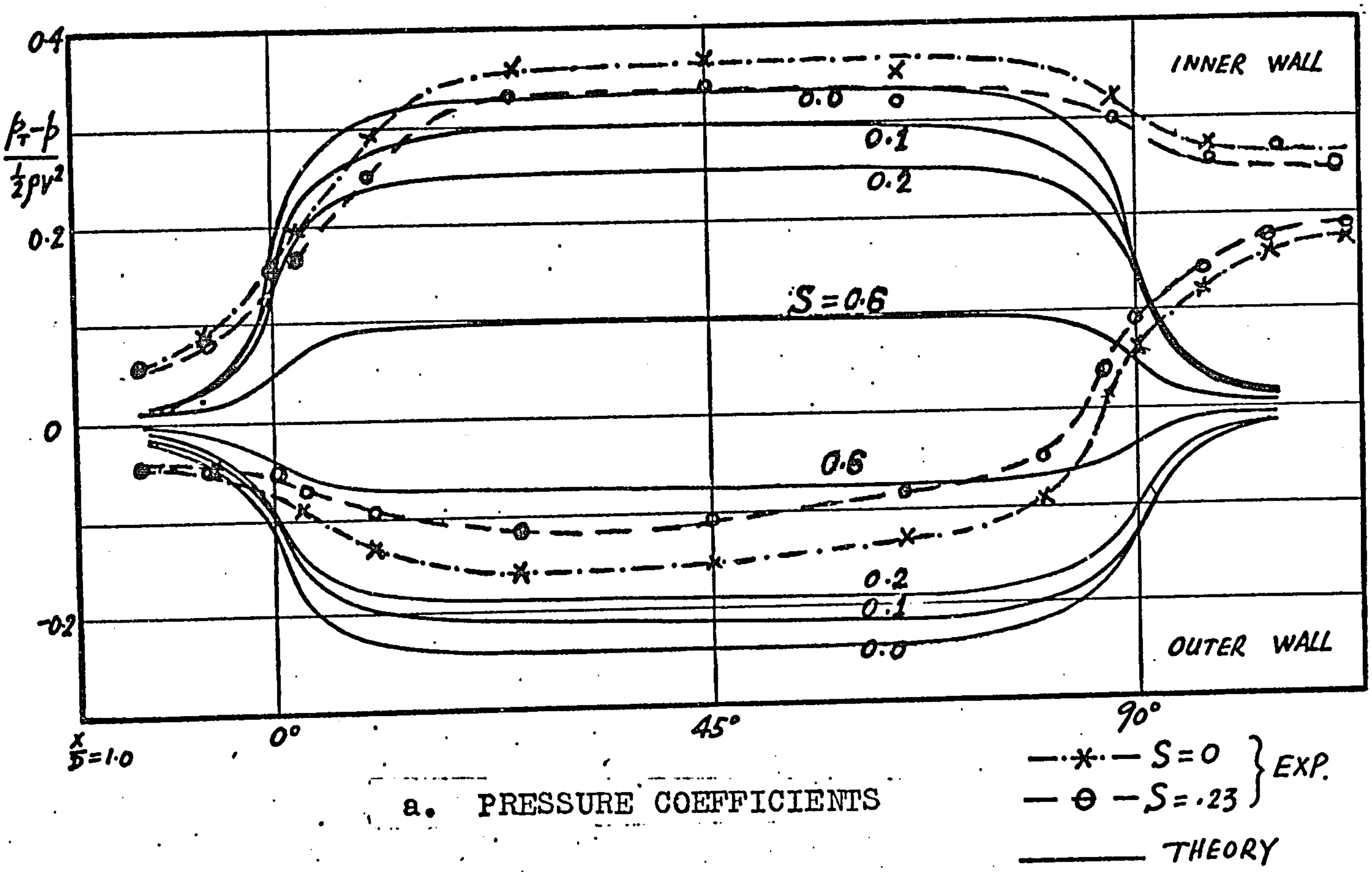

a. PRESSURE COEFFICIENTS

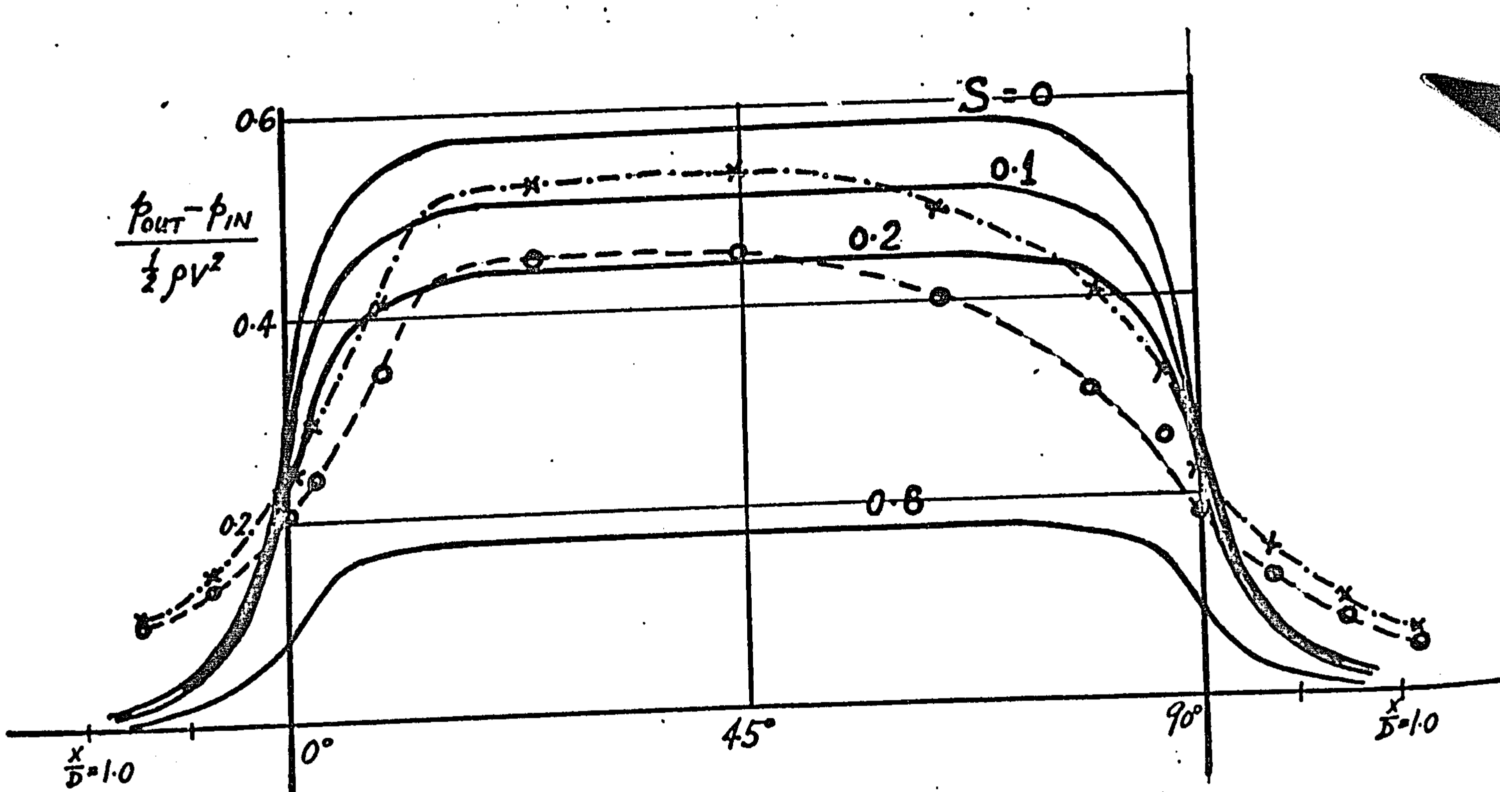

b. PRESSURE DIFFERENCE BETWEEN OUTER AND INNER WALLS

FIG. 21 EXPERIMENTAL RESULTS WITH ELECTROLYTE

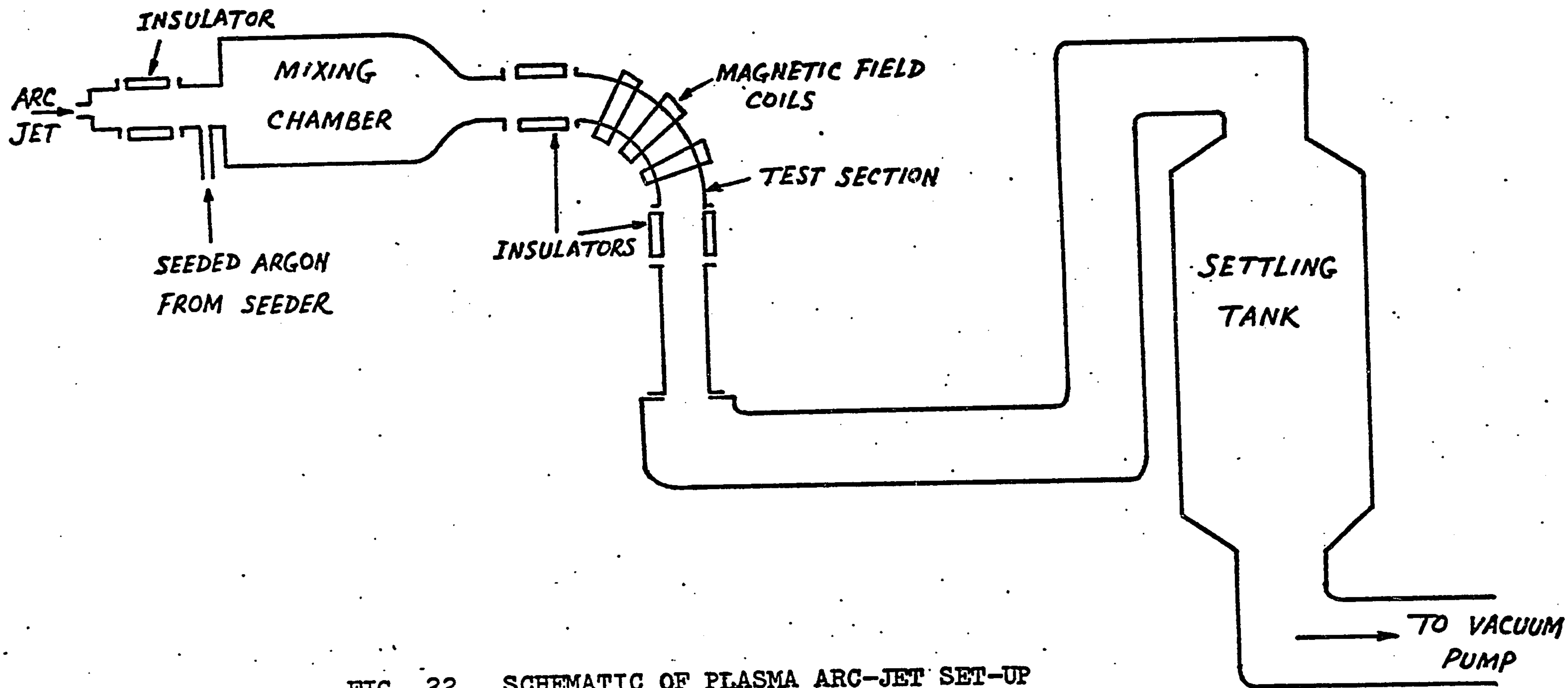

FIG. 22 SCHEMATIC OF PLASMA ARC-JET SET-UP

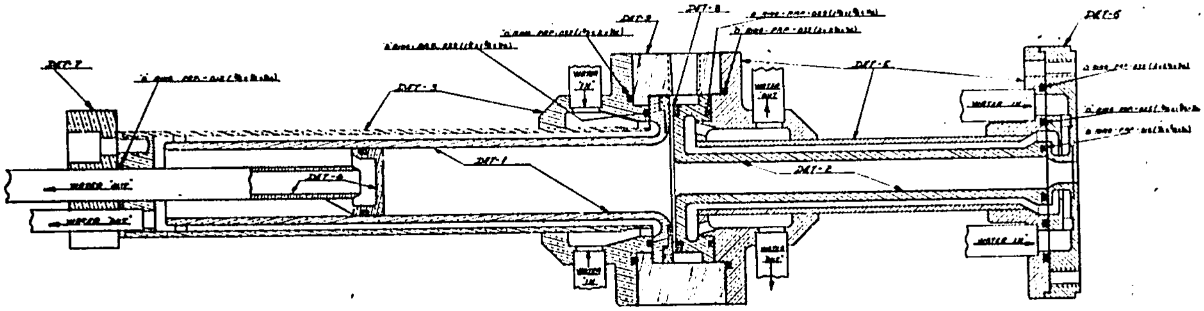

a. SCHEMATIC

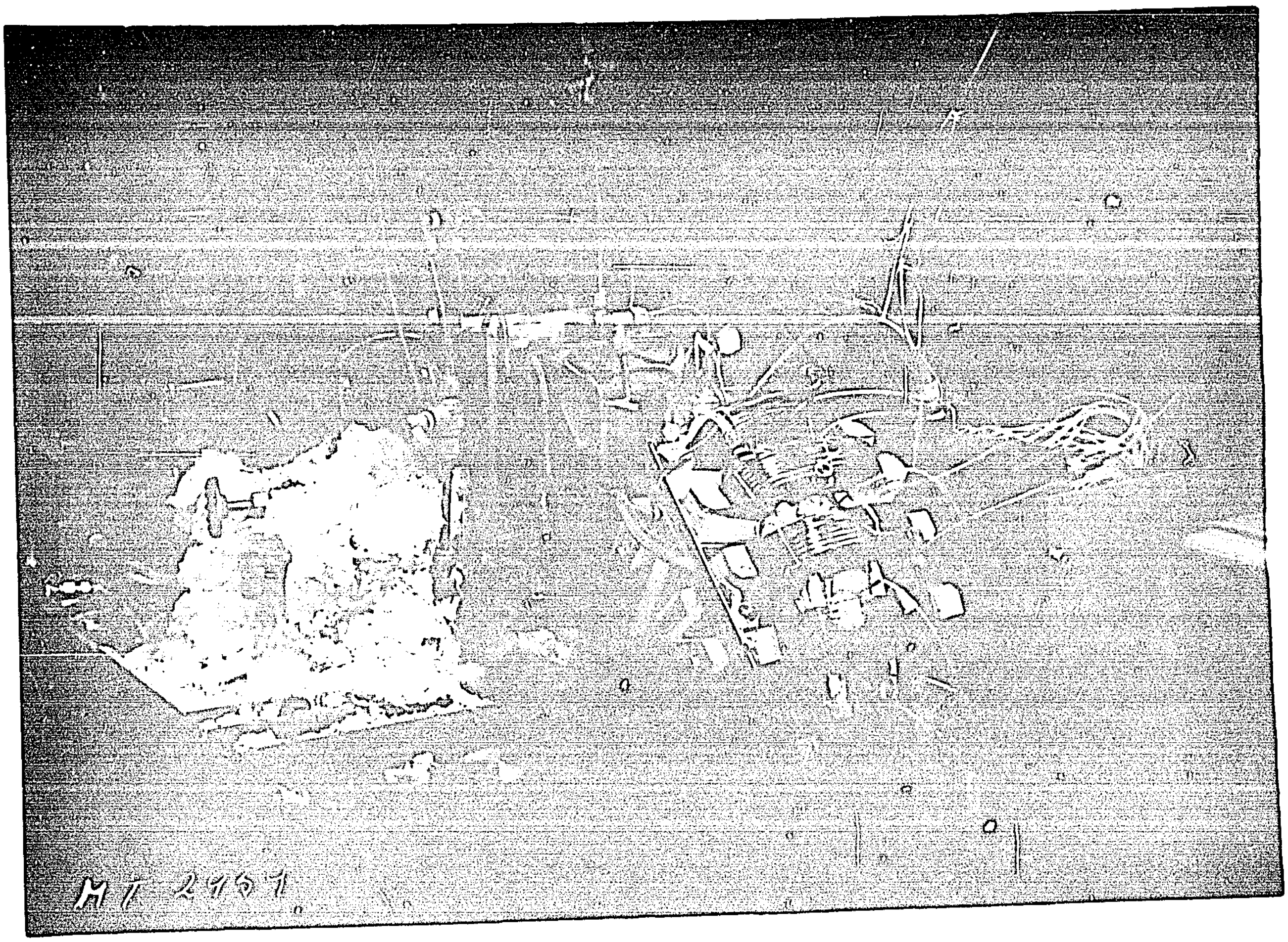

b. PHOTOGRAPH OF ARC-JET AND TEST SECTION

FIG. 23 PLASMA ARC-JET

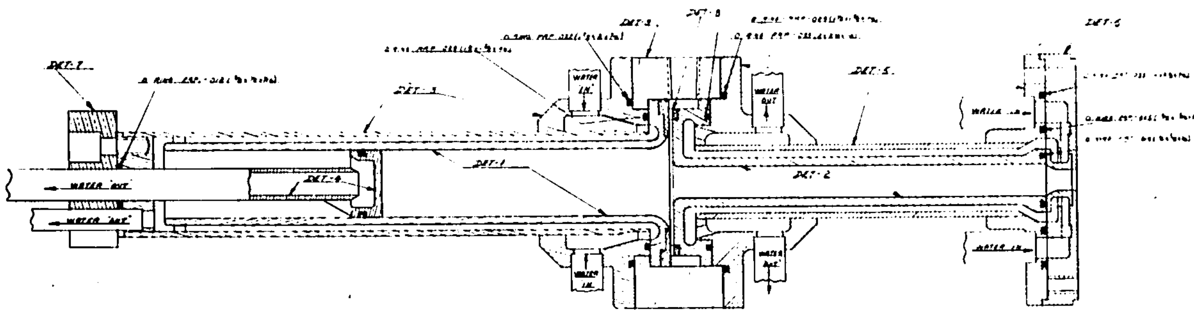

a. SCHEMATIC

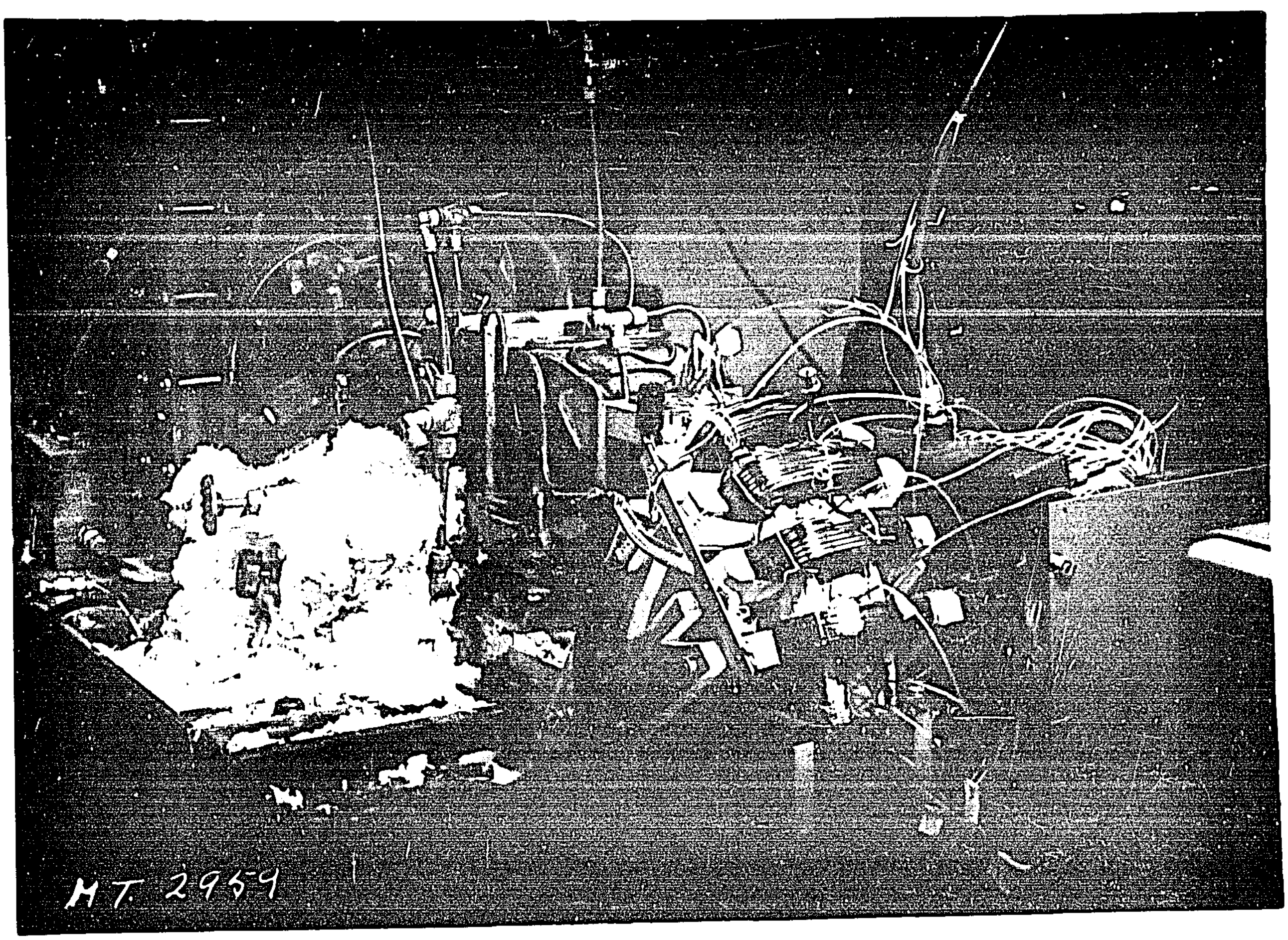

b. PHOTOGRAPH OF ARC-JET AND TEST SECTION

FIG. 23 PLASMA ARC-JET

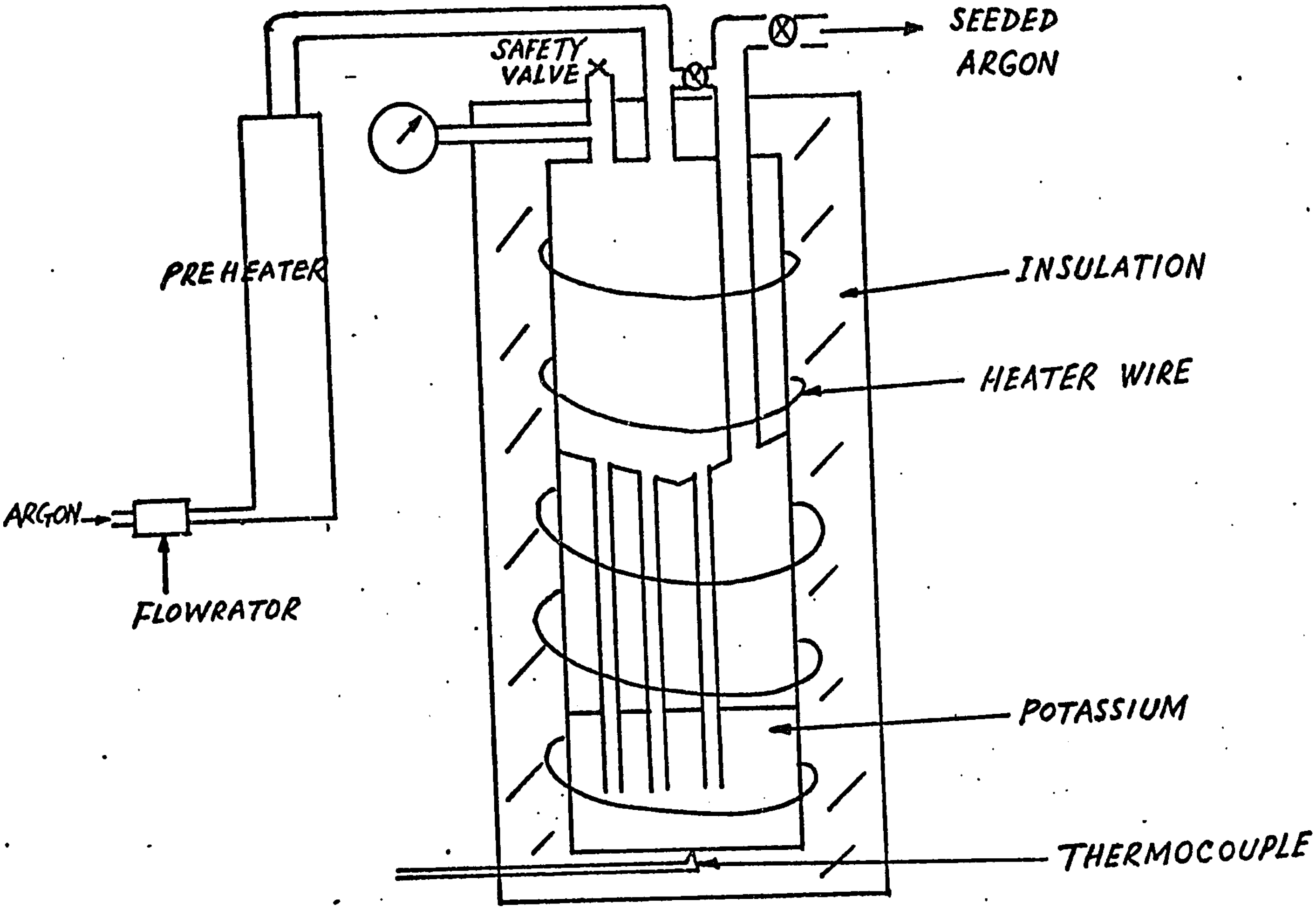

FIG. 24 SCHEMATIC OF SEEDER

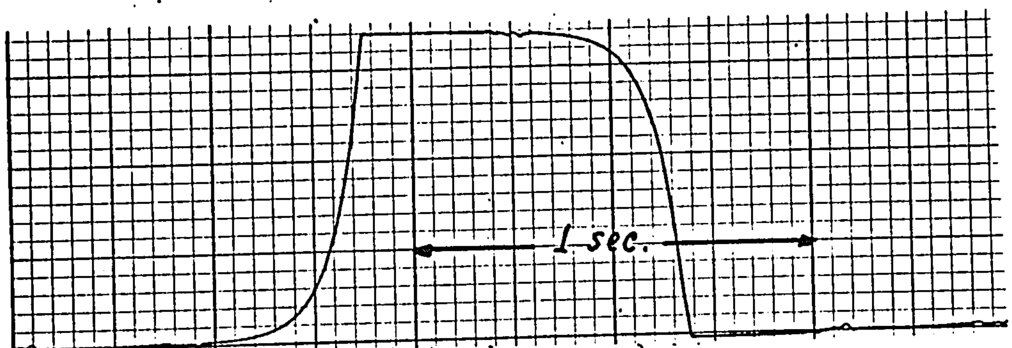

a. CALIBRATION

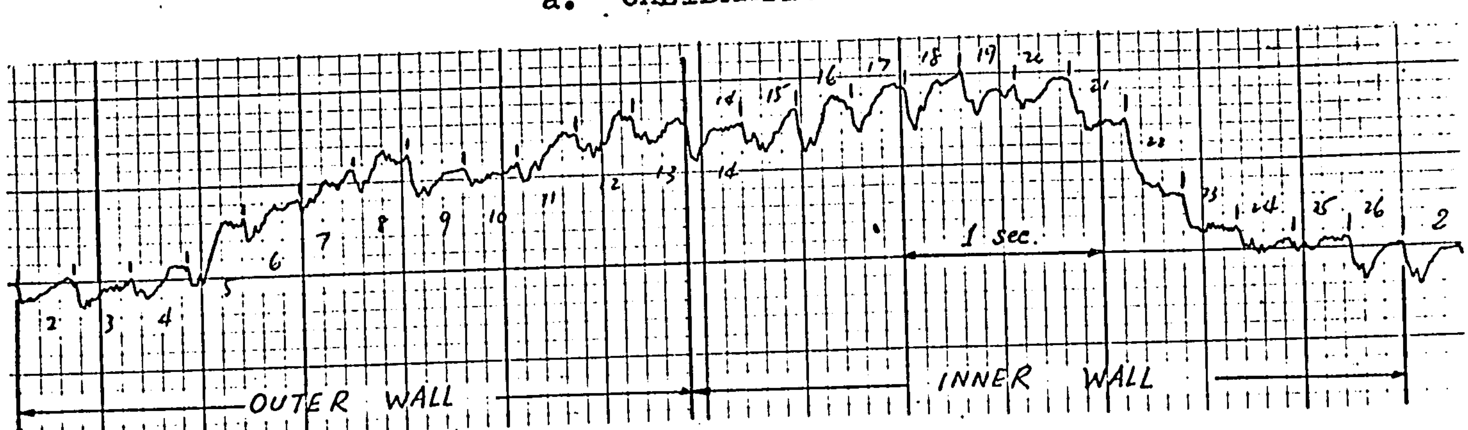

b. TYPICAL PRESSURE RECORD OF PLASMA RUN

FIG. 25 PRESSURE RECORDS

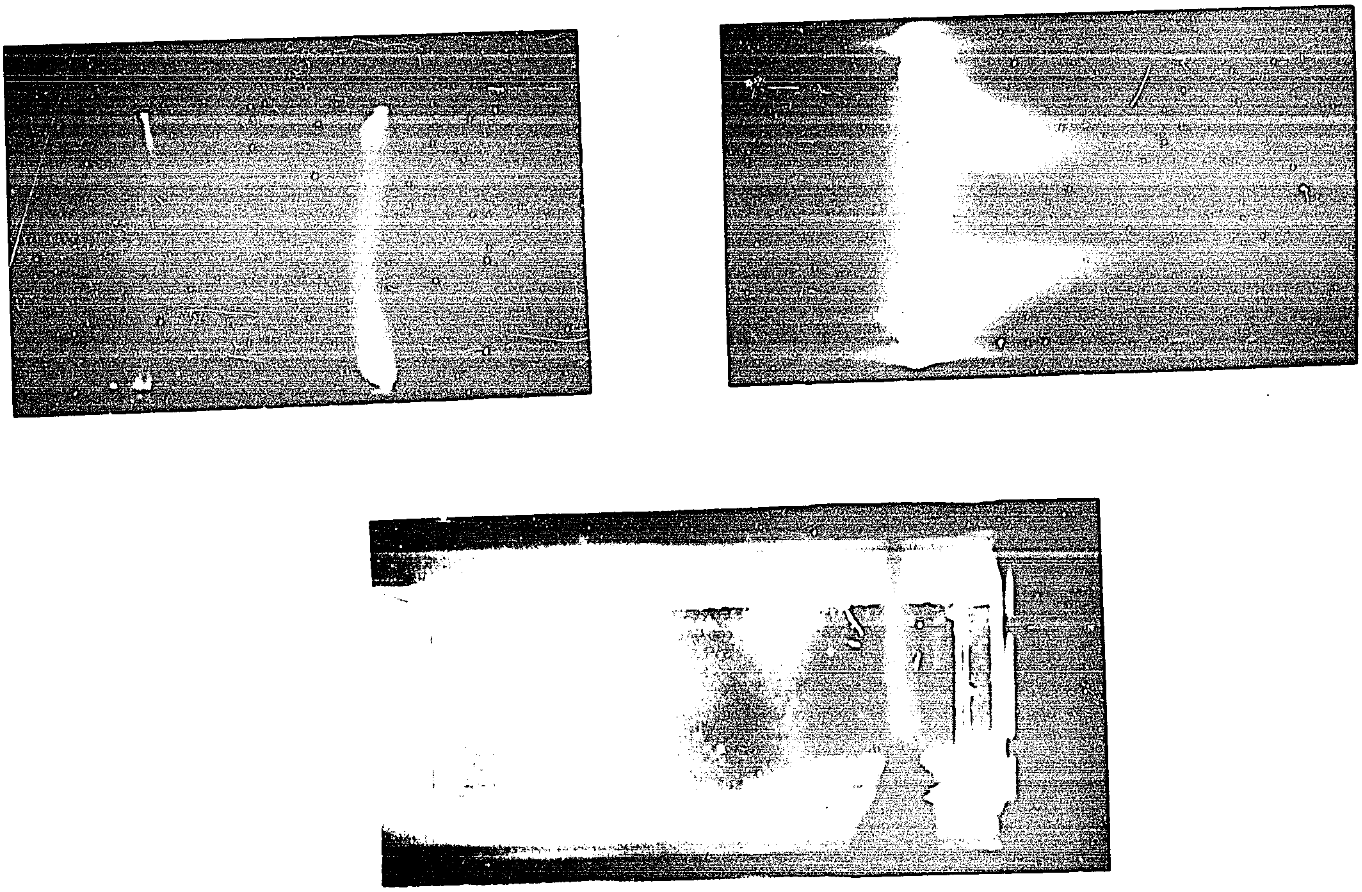

FIG. 26 VELOCITY MEASUREMENT WITH SPARK TRACING

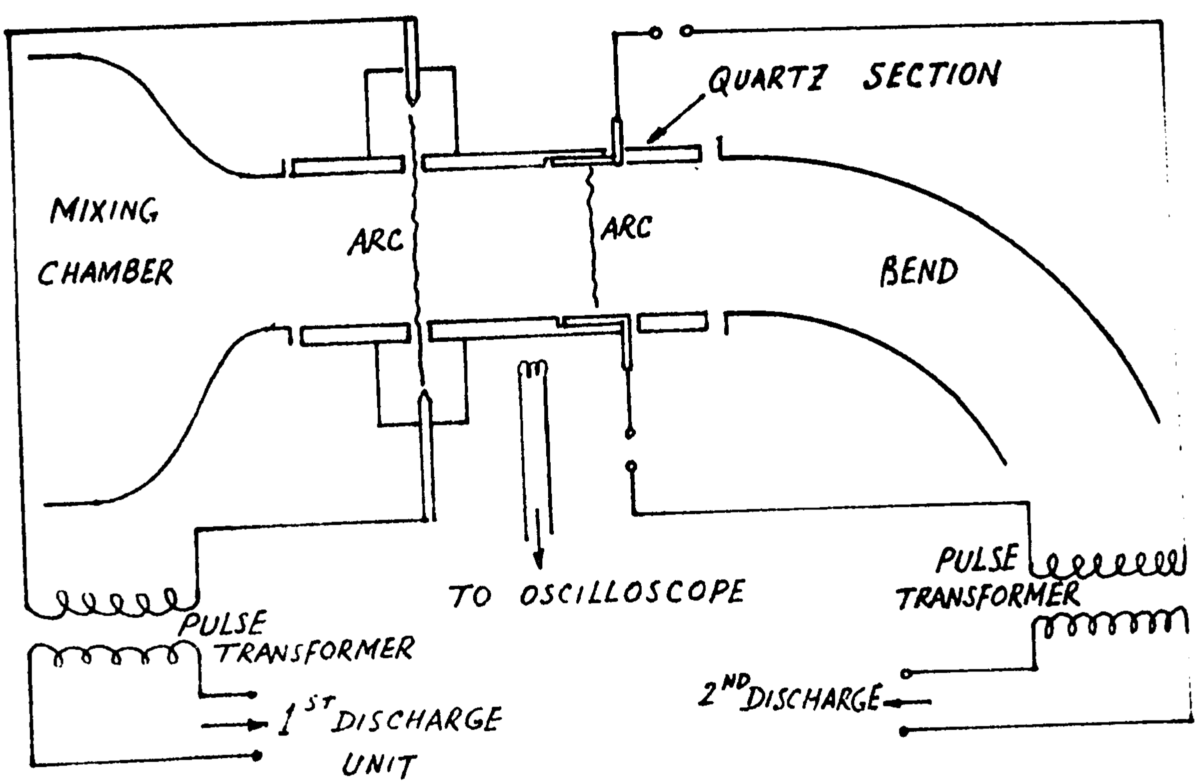

FIG. 27 SCHEMATIC OF SPARK TRACING SET-UP

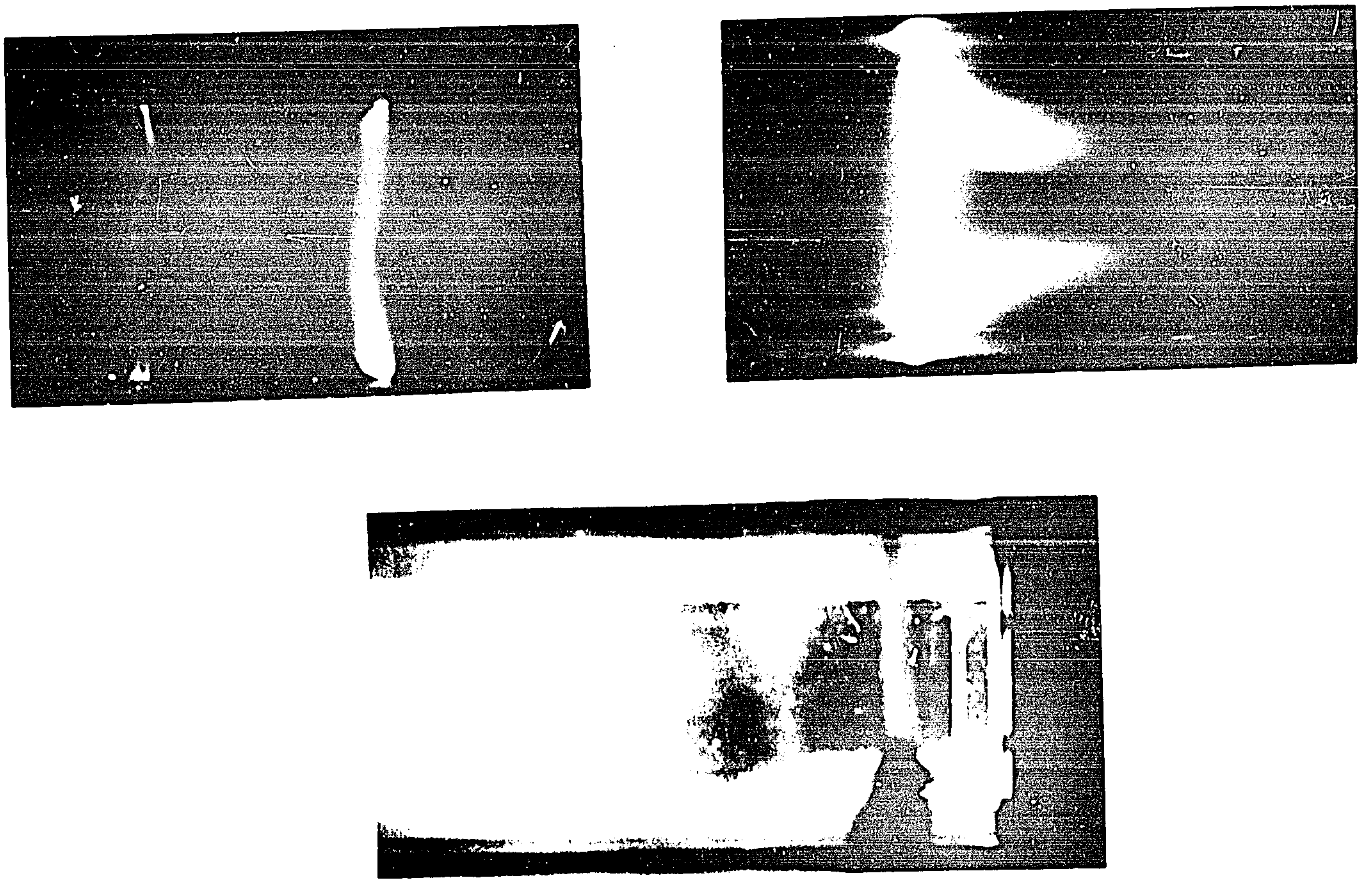

FIG. 26 VELOCITY MEASUREMENT WITH SPARK TRACING

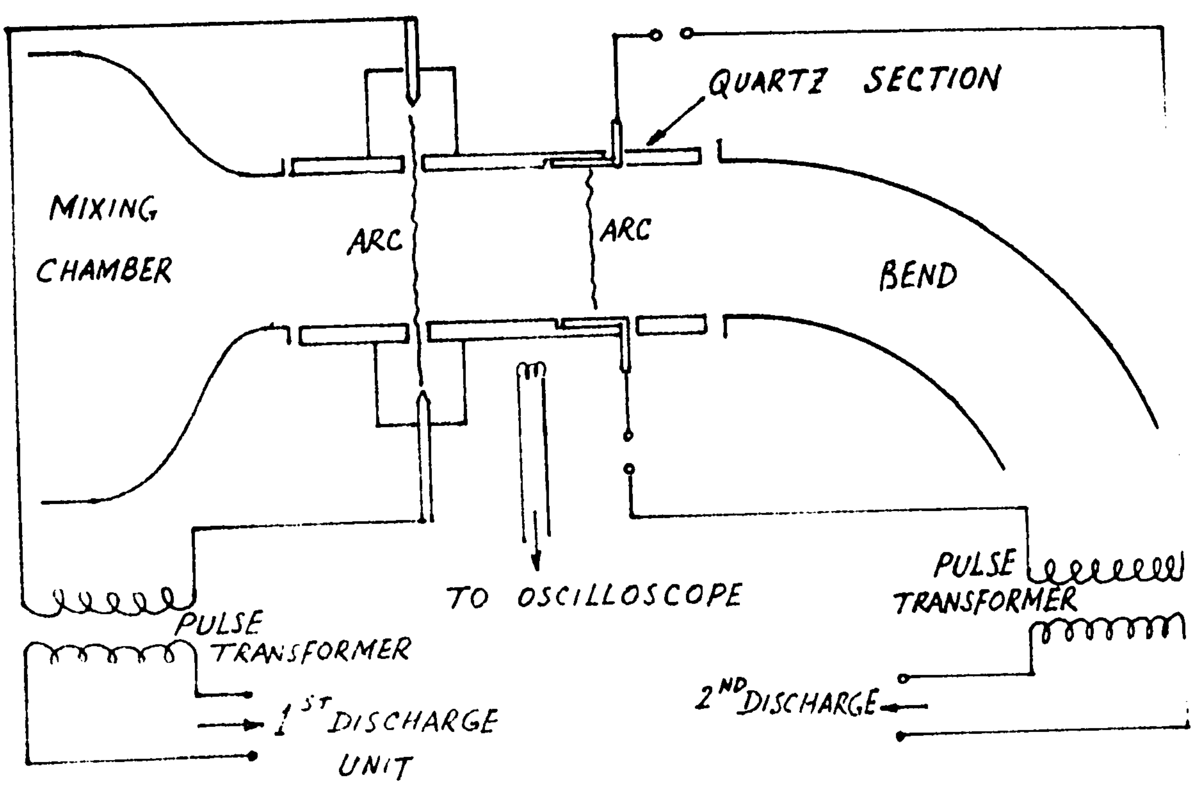

FIG. 27 SCHEMATIC OF SPARK TRACING SET-UP

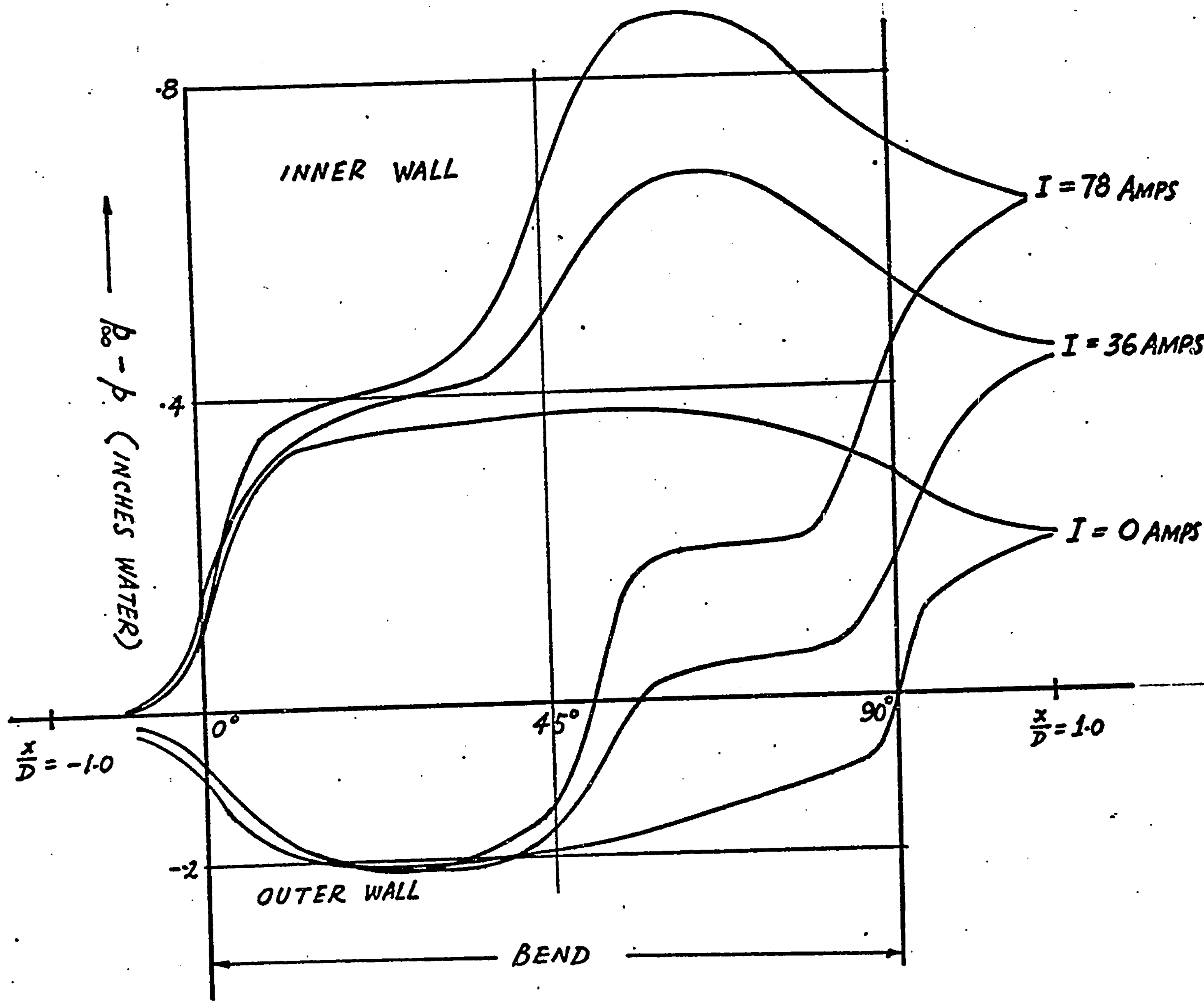

FIG. 28 PRESSURE DROP DUE TO OHMIC HEATING

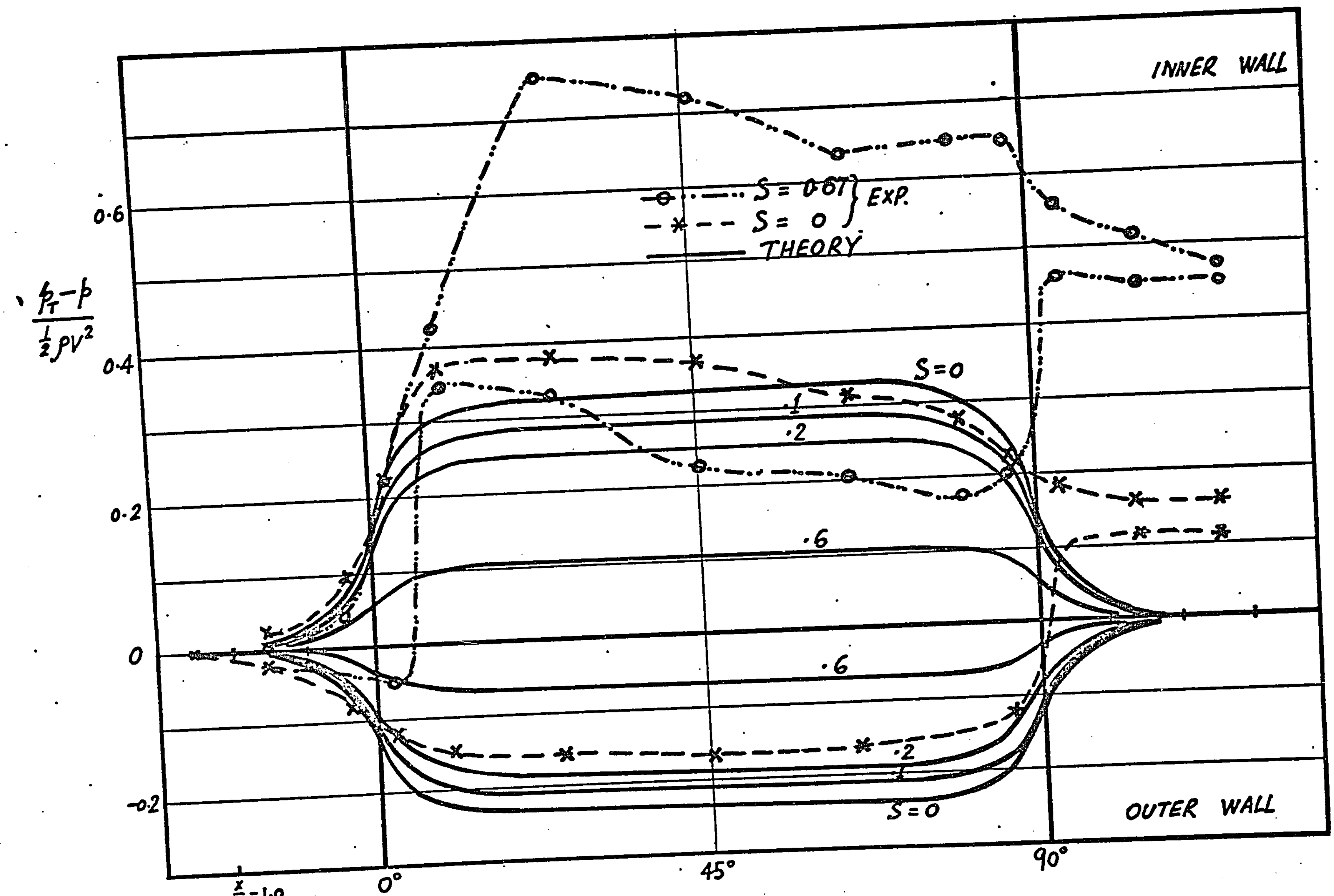

FIG. 29a PRESSURE COEFFICIENTS ALONG BEND

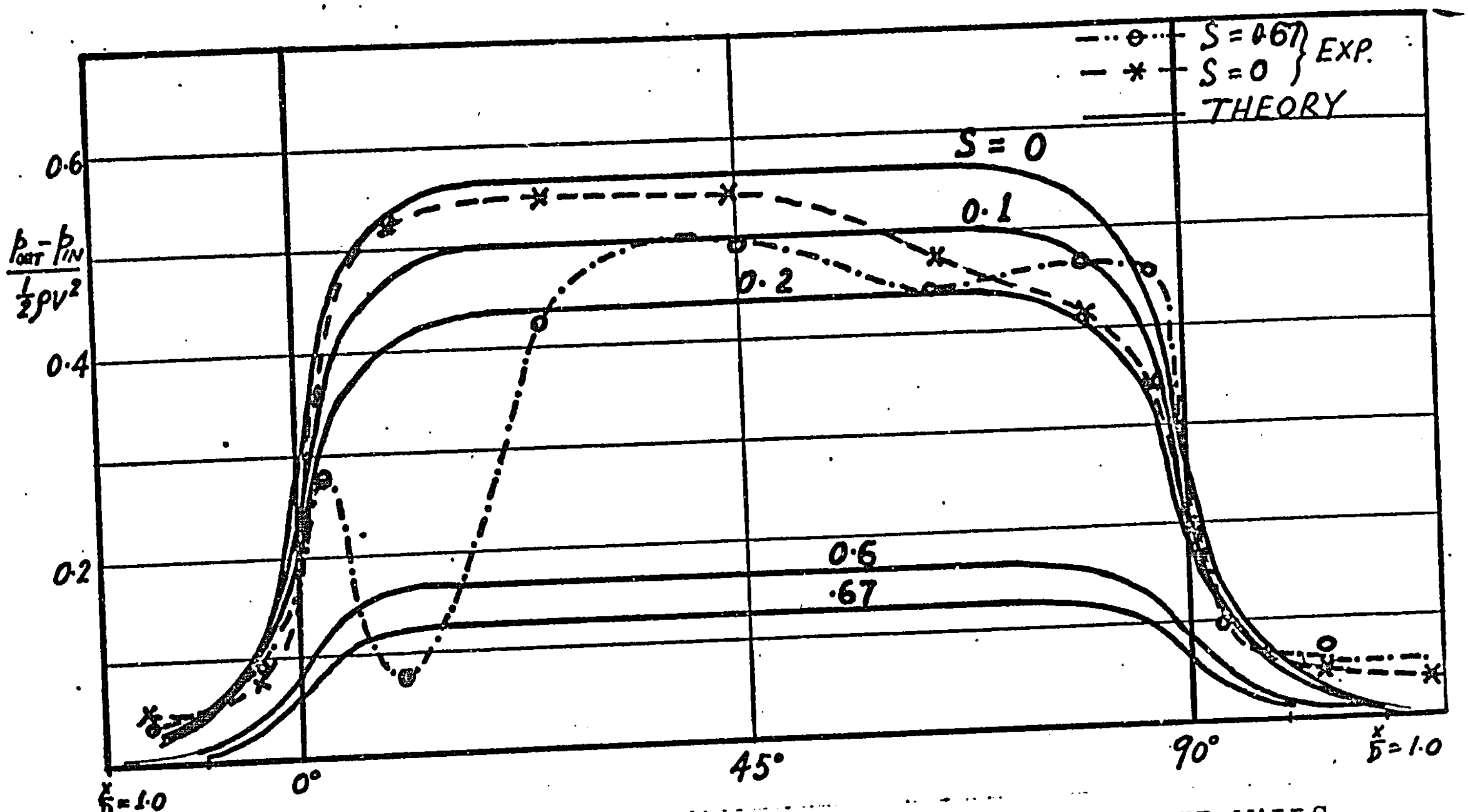

FIG. 29b PRESSURE DIFFERENCE BETWEEN OUTER AND INNER WALLS

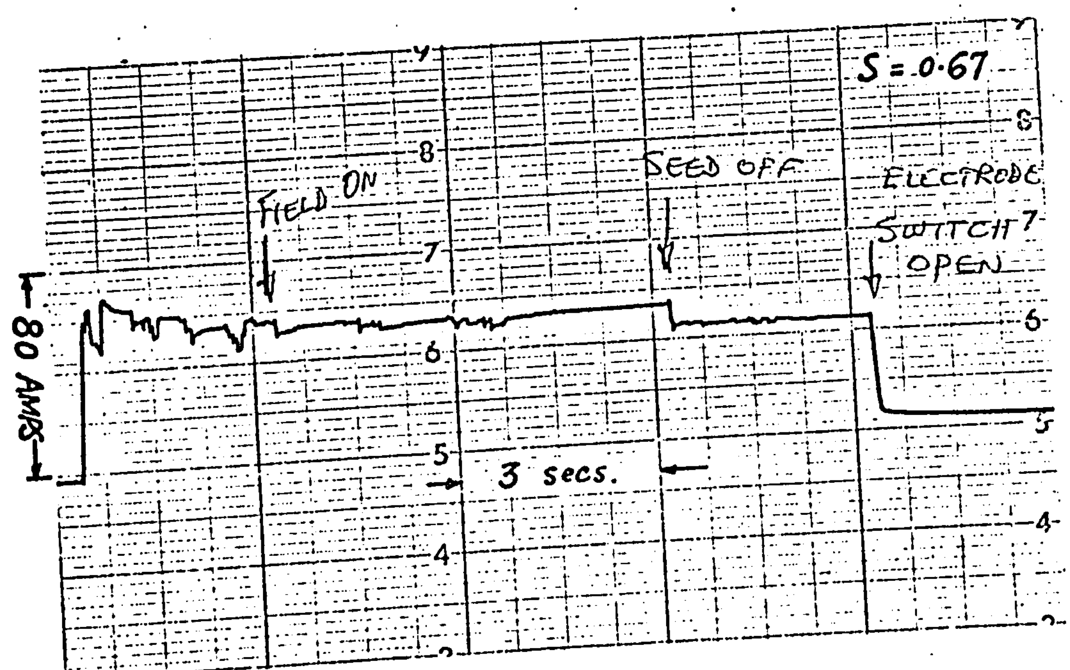

FIG. 29c CURRENT ACROSS ELEECRODE

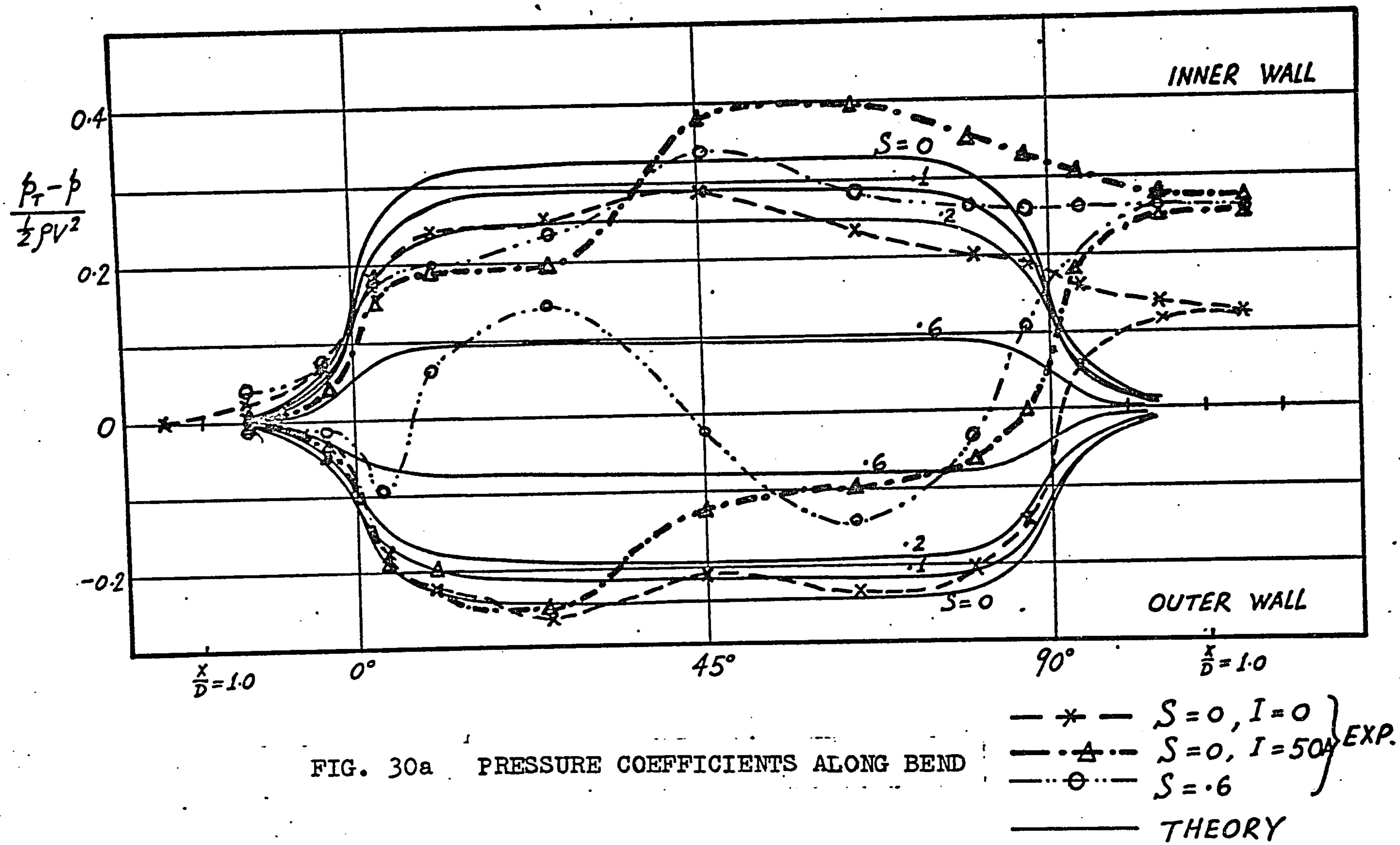

FIG. 30a PRESSURE COEFFICIENTS ALONG BEND

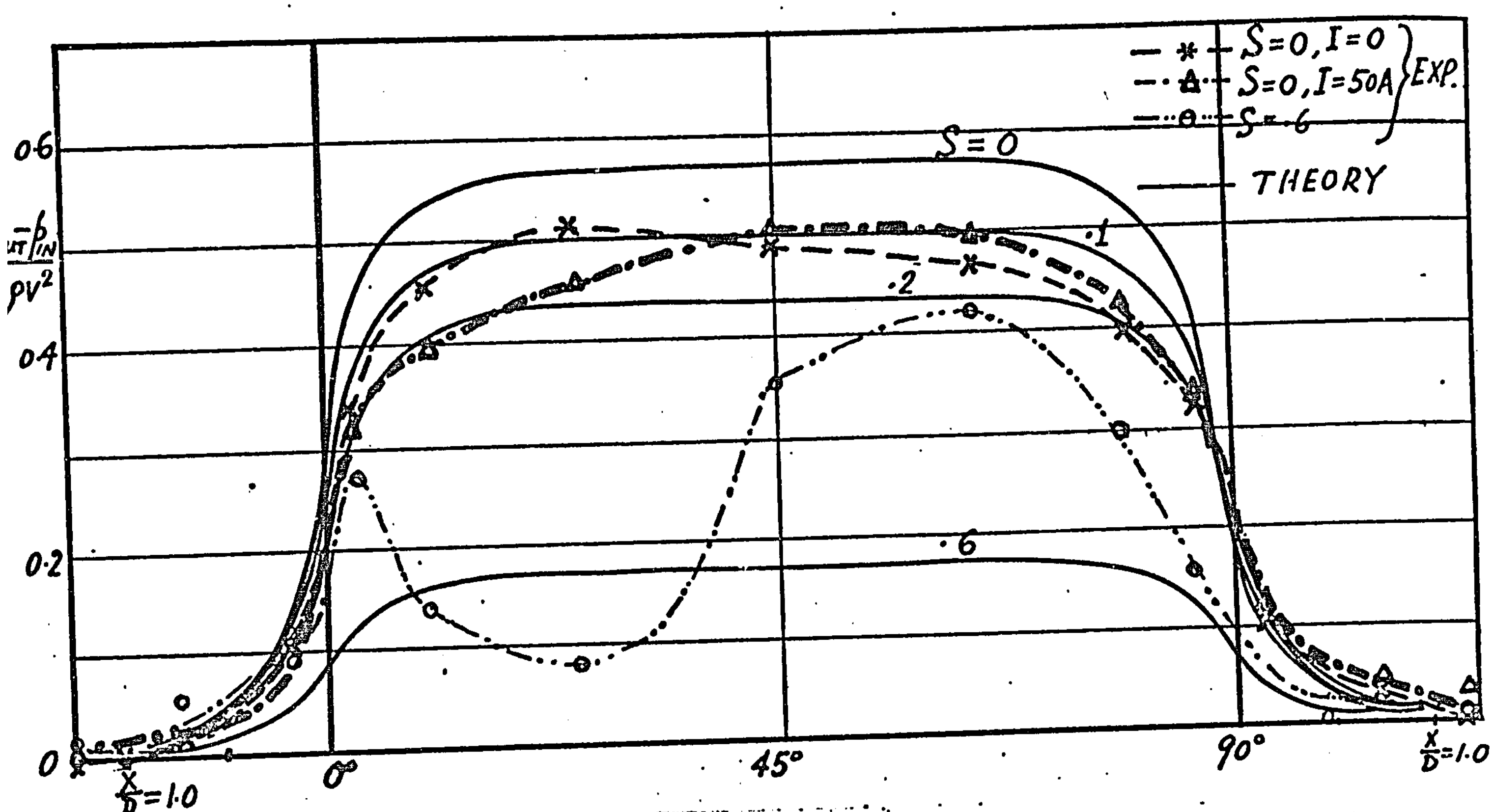

FIG. 30b PRESSURE DIFFERENCE BETWEEN OUTER AND INNER WALLS

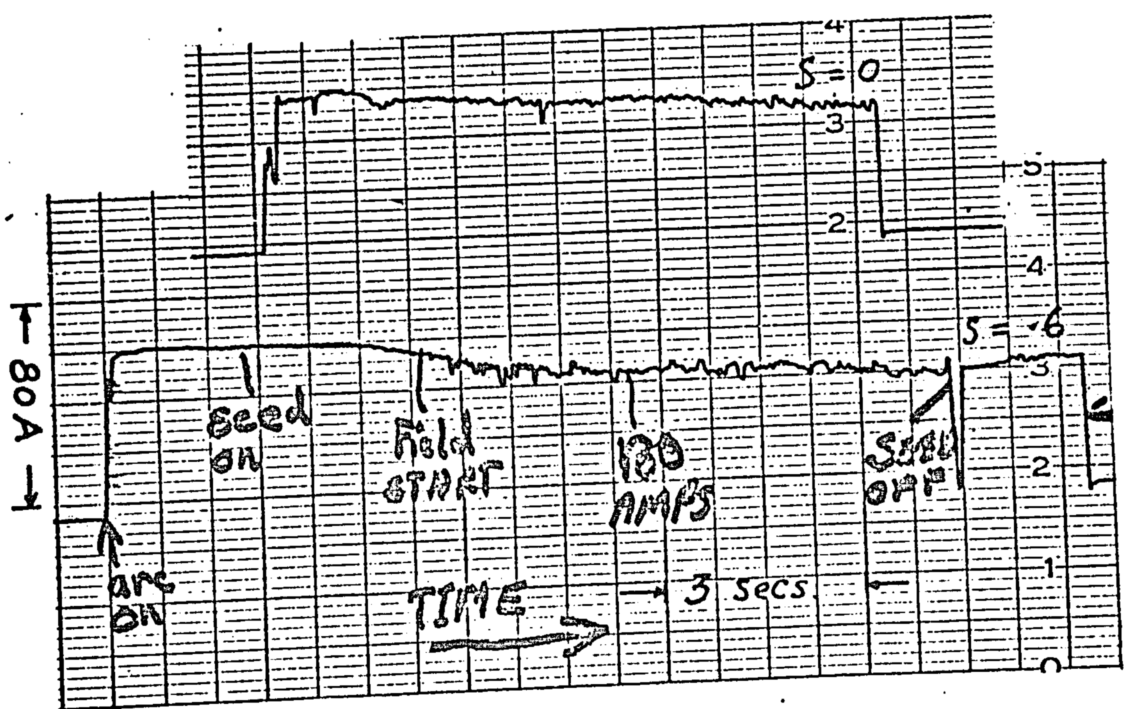

FIG. 30c CURRENT ACROSS ELECTRODE

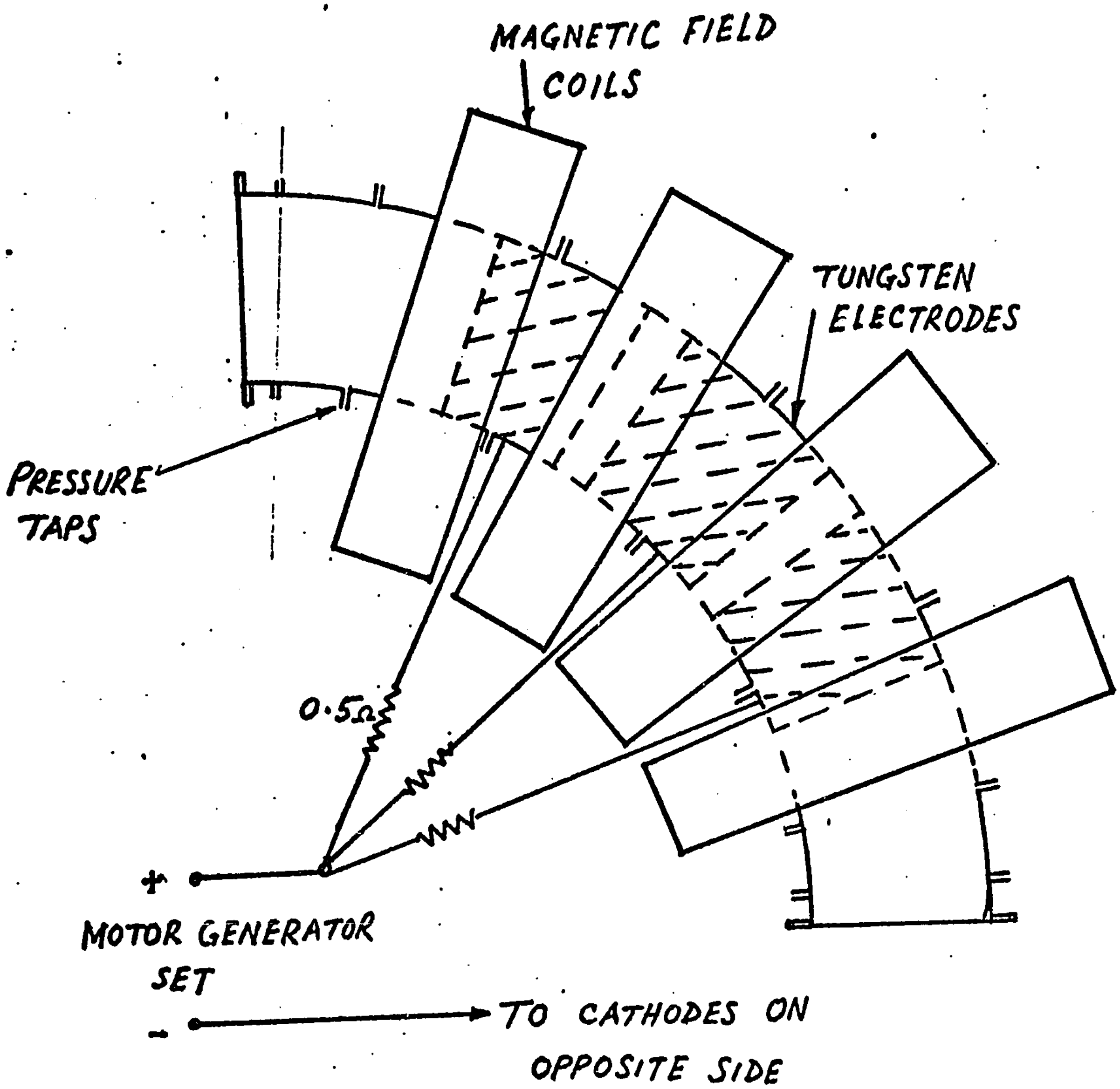

FIG. 31 SCHEMATIC OF MAGNETIC COILS AND ELECTRODE ARRANGEMENT

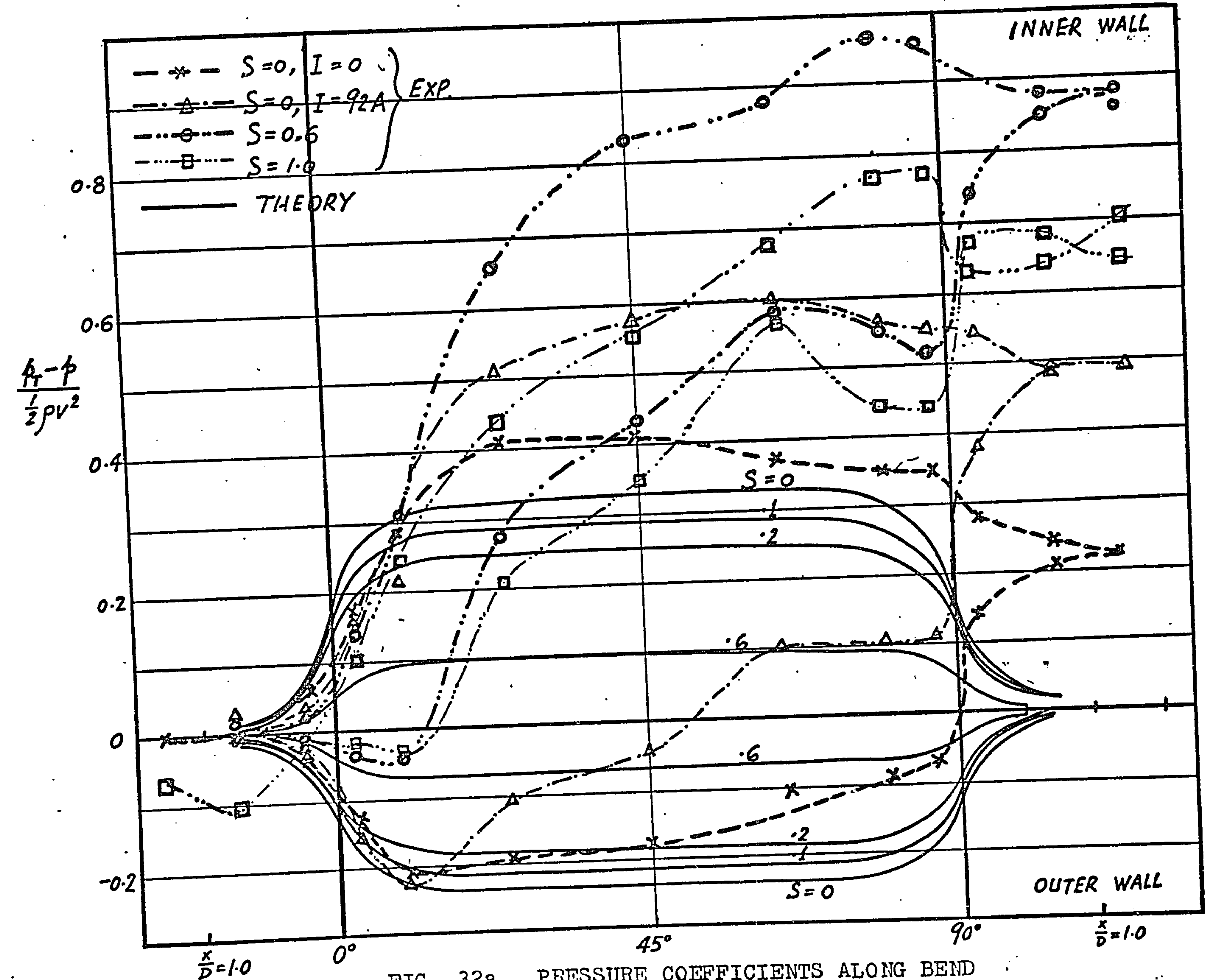

FIG. 32a PRESSURE COEFFICIENTS ALONG BEND

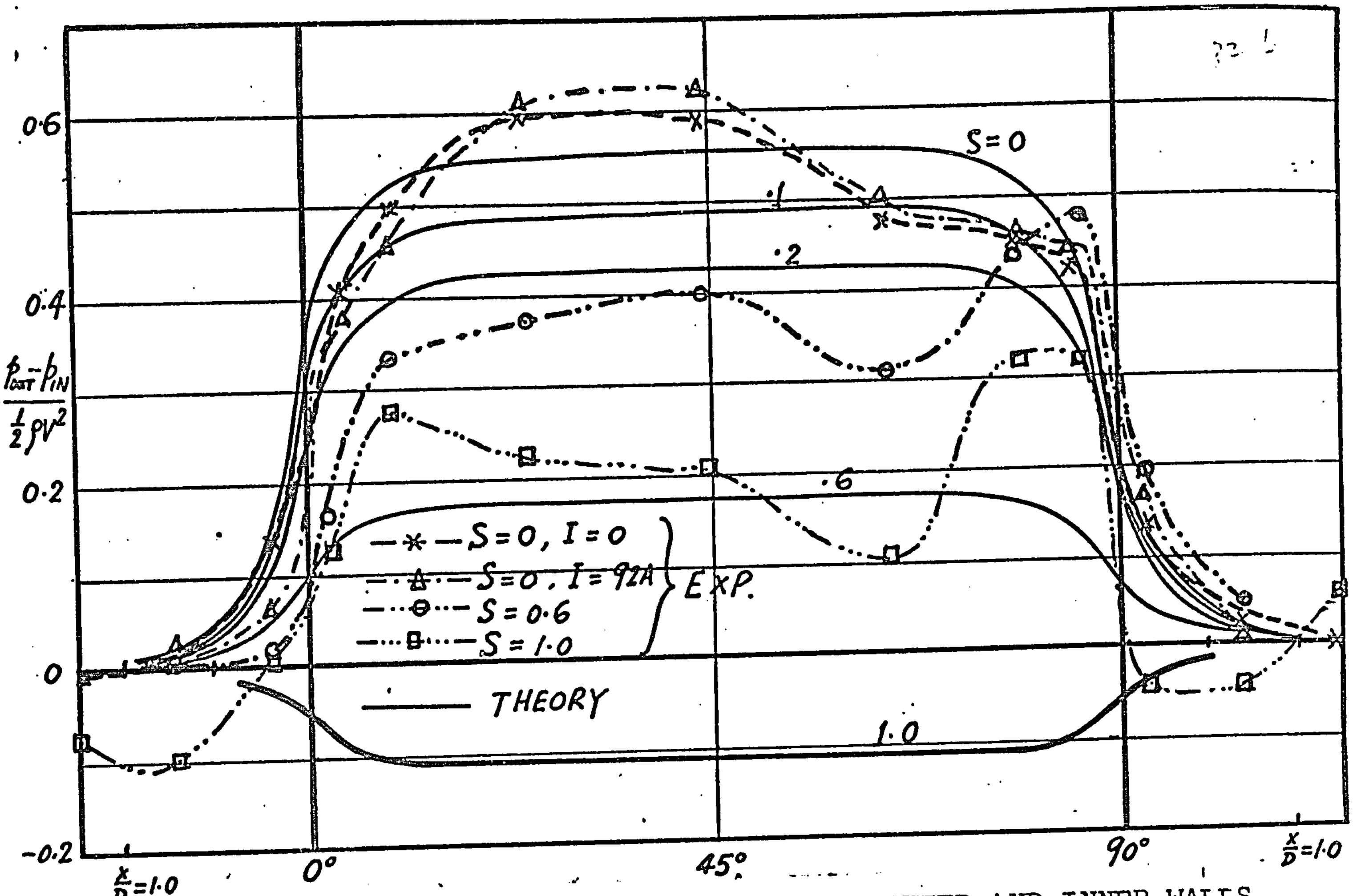

FIG. 32b PRESSURE DIFFERENCE BETWEEN OUTER AND INNER WALLS

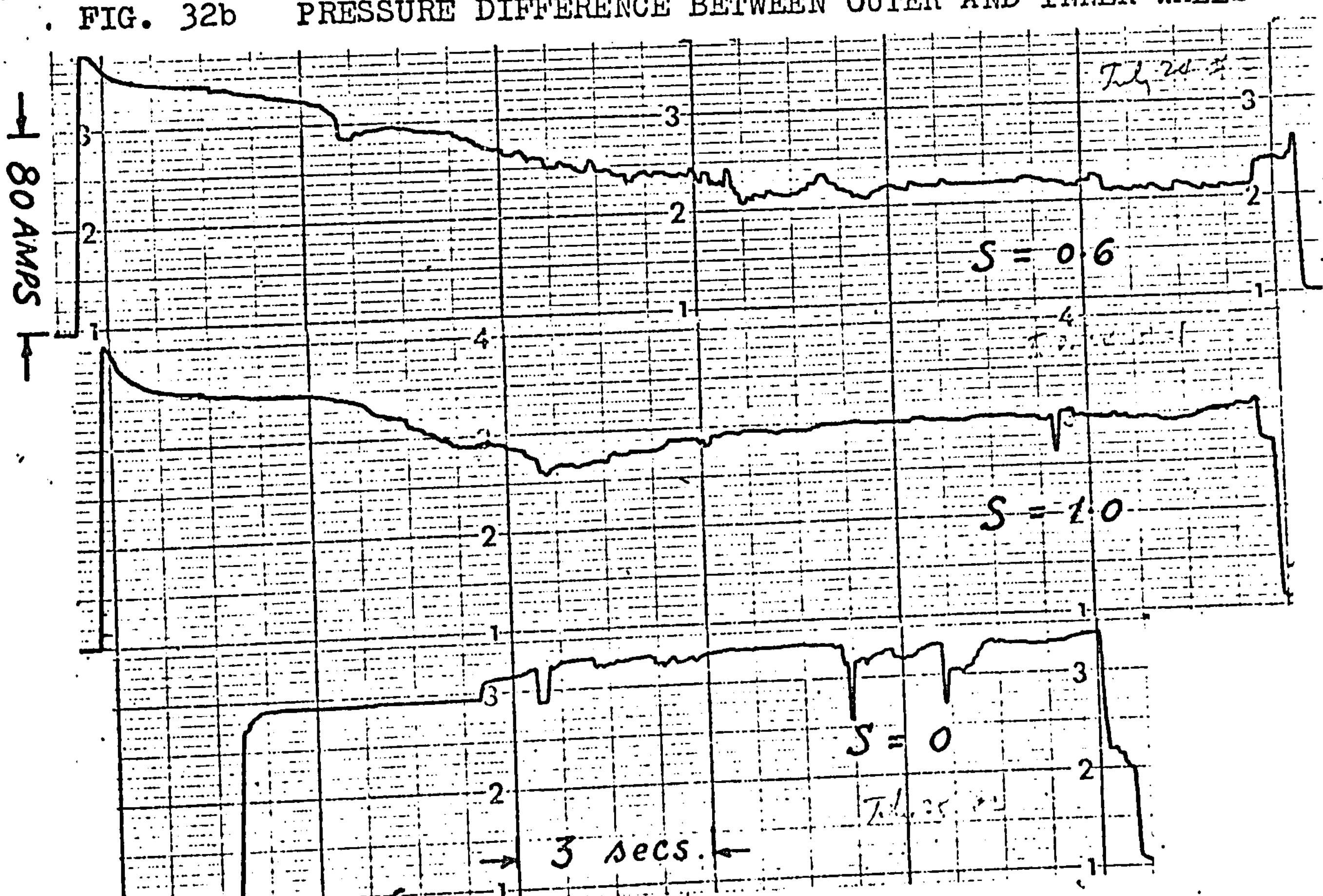

FIG. 32c TOTAL CURRENT ACROSS ELECTRODES

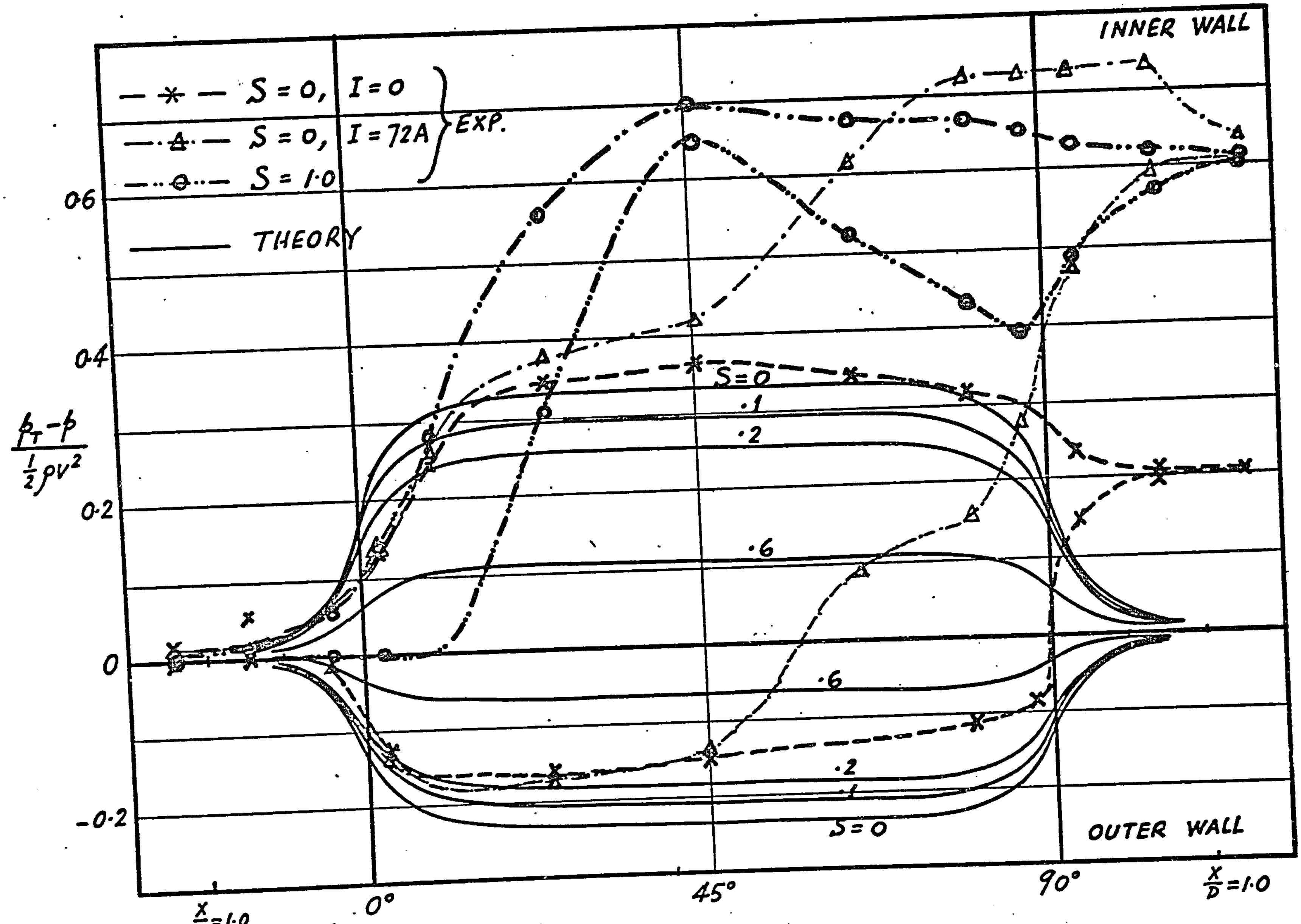

FIG. 33a PRESSURE COEFFICIENTS ALONG BEND

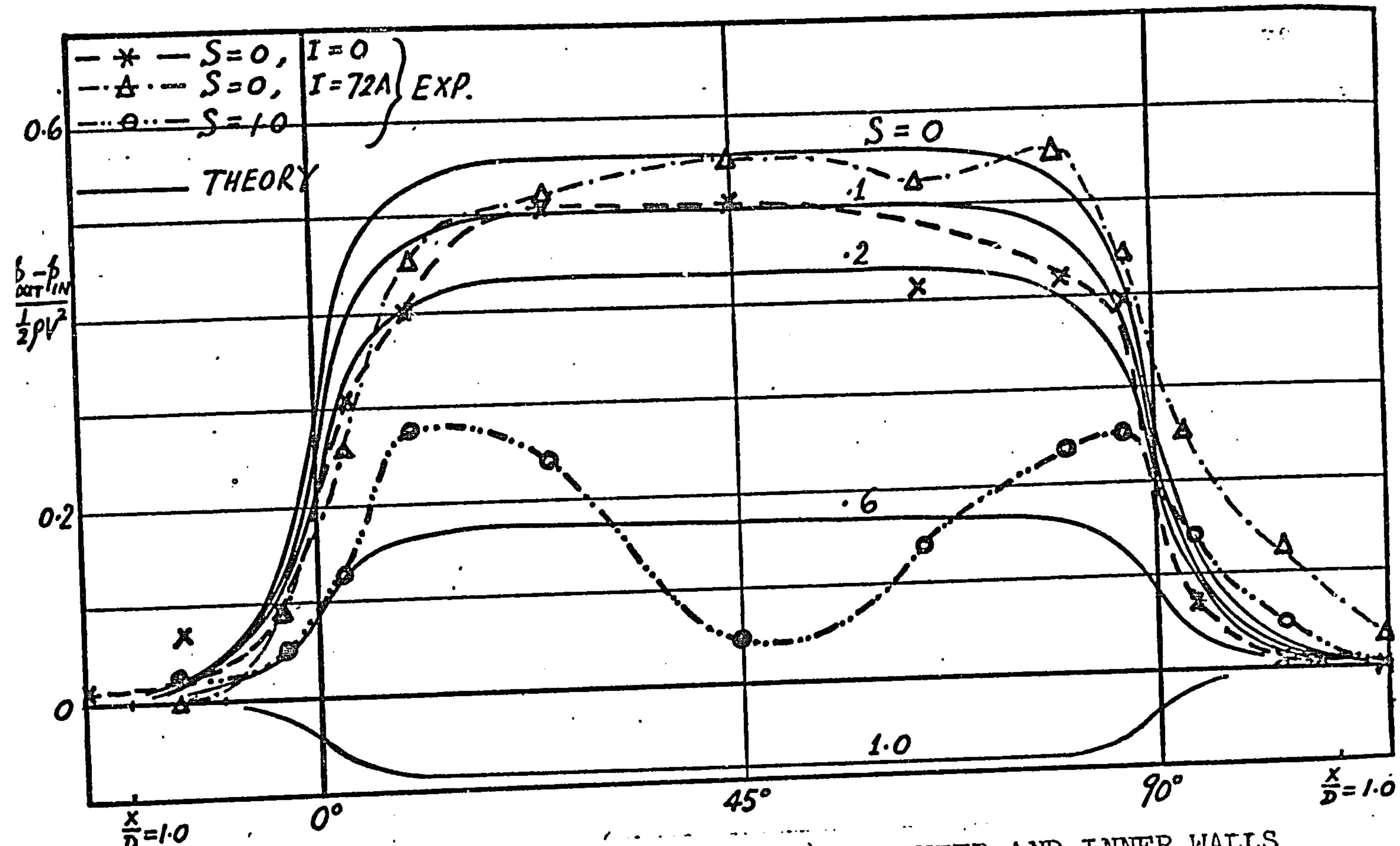

FIG. 33b PRESSURE DIFFERENCE BETWEEN OUTER AND INNER WALLS

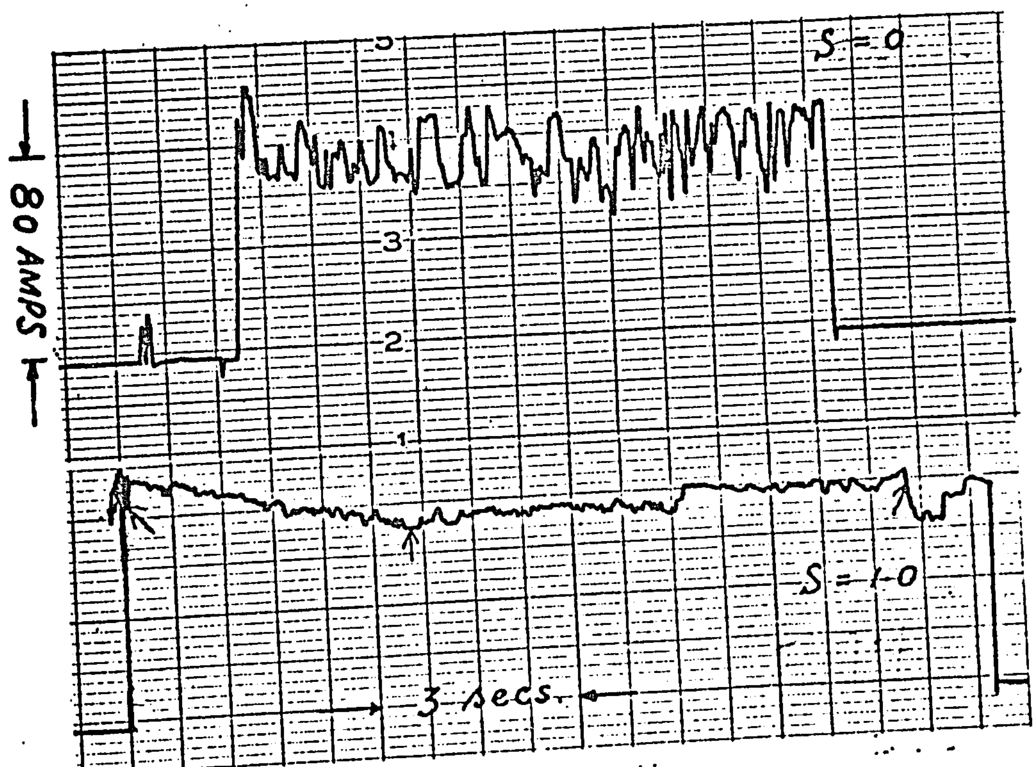

FIG. 33c TOTAL CURRENT ACROSS ELECTRODES

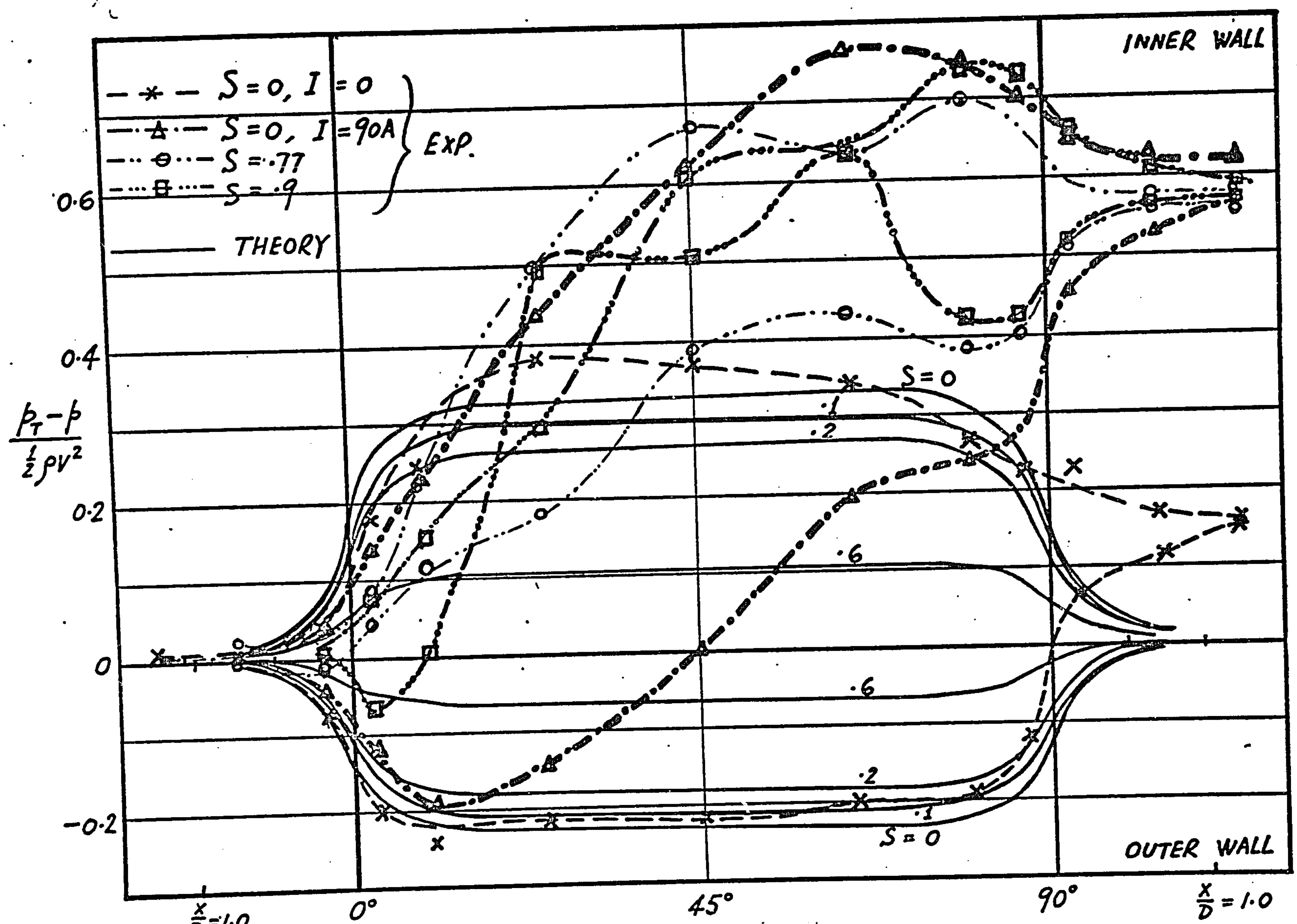

FIG. 34a PRESSURE COEFFICIENTS ALONG BEND

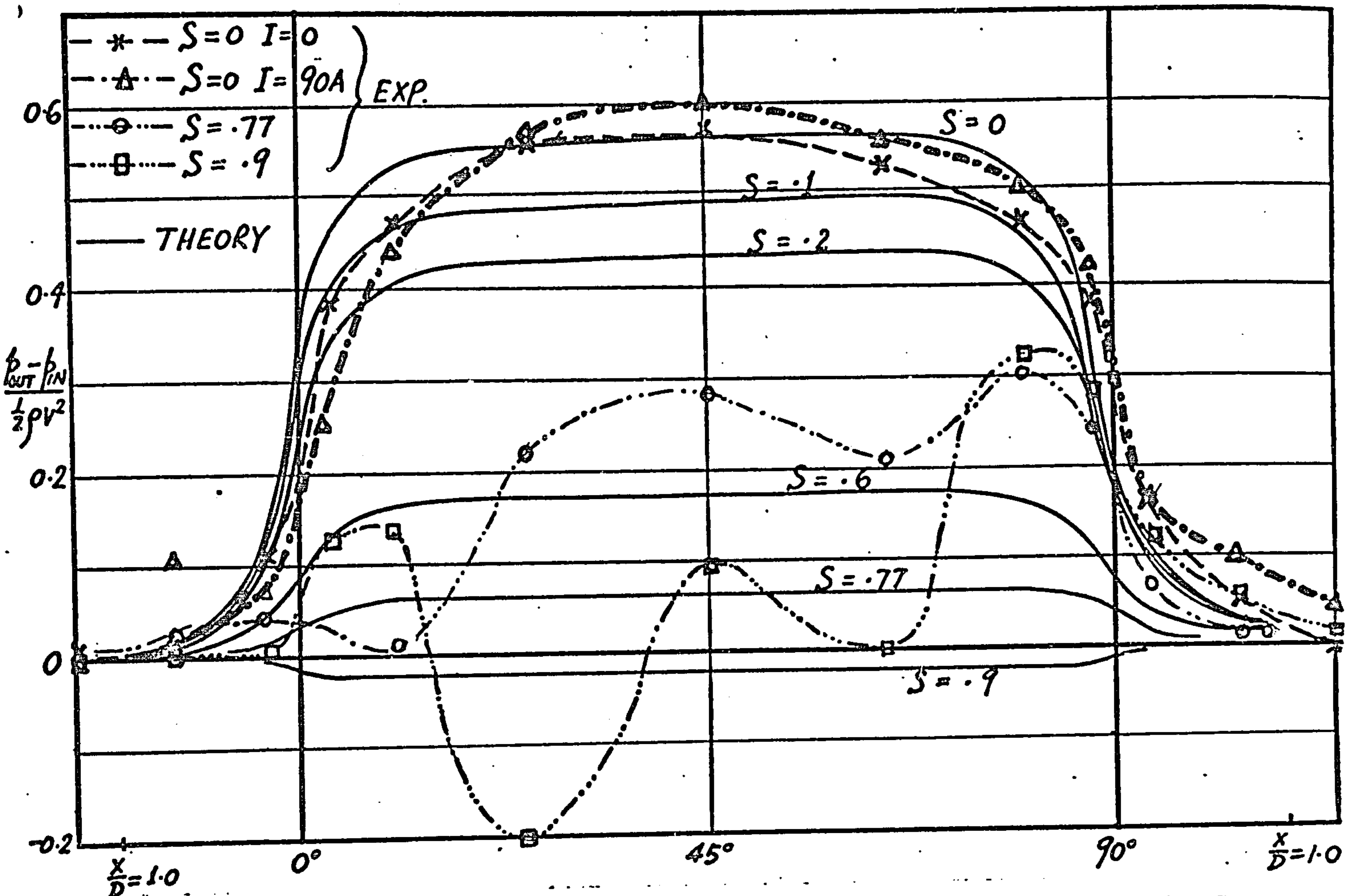

FIG. 34b PRESSURE DIFFERENCE BETWEEN OUTER AND INNER WALLS

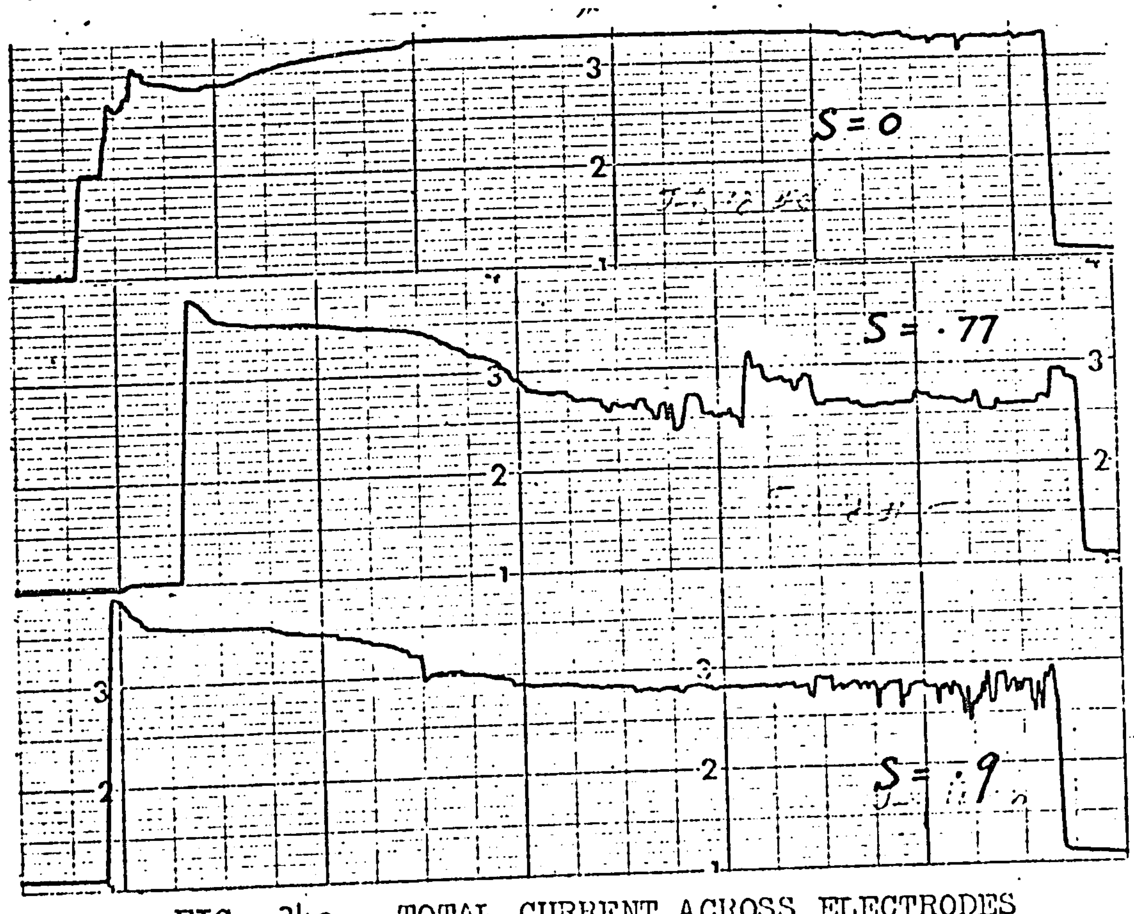

FIG. 34c TOTAL CURRENT ACROSS ELECTRODES

VITA

Name:		John Hoi Wai LAU
Born:		20 May, 1937, Hong Kong

Educated:

Primary:		La Salle College, Hong Kong
Secondary:		La Salle College, Hong Kong
University:		
	a)	The University of Toronto, Toronto, 1960 Bachelor of Applied Science (B.A.Sc.) Engineering Physics Option.
	b)	The University of Toronto, Institute of Aerophysics 1961 Master of Applied Science (M.A.Sc.)

END OF
REEL